



Thermomechanical vibration response of nanoplates with magneto-electro-elastic face layers and functionally graded porous core using nonlocal strain gradient elasticity

Mehmet Akif Koç, İsmail Esen & Mustafa Eroğlu

To cite this article: Mehmet Akif Koç, İsmail Esen & Mustafa Eroğlu (2024) Thermomechanical vibration response of nanoplates with magneto-electro-elastic face layers and functionally graded porous core using nonlocal strain gradient elasticity, *Mechanics of Advanced Materials and Structures*, 31:18, 4477-4509, DOI: [10.1080/15376494.2023.2199412](https://doi.org/10.1080/15376494.2023.2199412)

To link to this article: <https://doi.org/10.1080/15376494.2023.2199412>



Published online: 18 Apr 2023.



Submit your article to this journal [↗](#)



Article views: 490



View related articles [↗](#)





View Crossmark data [↗](#)



Citing articles: 15 View citing articles [↗](#)

Thermomechanical vibration response of nanoplates with magneto-electro-elastic face layers and functionally graded porous core using nonlocal strain gradient elasticity

Mehmet Akif Koç^a , İsmail Esen^b , and Mustafa Eroğlu^c 

^aTechnology Faculty, Mechatronics Engineering Department, Sakarya Applied Sciences University, Sakarya, Turkey; ^bEngineering Faculty, Mechanical Engineering Department, Karabük University, Karabük, Turkey; ^cEngineering Faculty, Mechanical Engineering Department, Sakarya University, Sakarya, Turkey

ABSTRACT

The thermal vibration and buckling behavior of a functionally graded nanoplate are examined in this study. The nanoplate is made up of a silicon nitride/stainless steel core plate and two cobalt-ferrite/barium-titanate face plates. Four alternative porosity models were used to simulate the porosity of the nanoplate, and numerous variables that can affect the nanoplate's behavior were taken into account. The study found that the thermomechanical behavior of nanoplates with magneto-electro-elastic face layers and a functionally graded porous core plate is affected by material gradation indices, porosity ratios, nonlocal variables, and different core plate material porosity models.

ARTICLE HISTORY

Received 15 March 2023
Accepted 2 April 2023

KEYWORDS

Thermal vibration; buckling behavior; silicon nitride; cobalt-ferrite; functionally graded material

1. Introduction

Magneto-electro-elastic (MEE) materials are a type of material that can change shape or dimensions when exposed to a magnetic field (magnetostriction) and can generate electrical charges when subjected to mechanical stress (piezoelectricity). These properties make MEE materials attractive for use in various applications of nanotechnology. For example, they can be used as sensors and actuators, which can convert electrical signals into mechanical motion or vice versa. MEE materials may also be used in the development of microelectromechanical systems (MEMS) and nanoelectromechanical systems (NEMS) for use in fields such as robotics, medical technology, and electronics. Additionally, MEE materials have the potential to be used in energy harvesting devices, which can convert mechanical energy into electrical energy through the use of piezoelectricity. Ongoing research is exploring the potential uses of MEE materials in nanotechnology [1–6].

The enormous potential for application in recently emerging technology advancements makes understanding the mechanical behavior of a system comprised of smart materials essential. Silicon Nitride (Si_3N_4) and stainless steel (SUS304) are the most used materials in micro/nanoelectromechanical systems because of their excellent strength and endurance [7]. A silicon nitride ceramic substance is renowned for its great strength, low density, and superior wear and corrosion resistance. It can function at high temperatures and is a great electrical insulator. These characteristics make it ideal for use in structural and wear-resistant

components and MEMS/NEMS applications such as MEMS sensors and actuators [8,9]. For example, a dense structure of silicon nitride ceramic was fabricated by direct ink writing using aqueous suspensions in the study [10]. A miniature and high-sensitivity volatile organic compound (VOC) sensor have been developed that can detect small amounts of the toxic chemical pyridine vapor in the air using a silicon nitride Mach-Zehnder interferometer waveguide with a sensitive cladding material made of polycarbonate [11]. The process produced microcracks, globules, pores, recast layers, and craters on the surface, with higher porosity levels observed in the rotary EDM process, according to this study, which looked at the machinability and surface characteristics of Si_3N_4 TiN composites when machined using rotary and die-sinking electrical discharge machining methods [12]. A steel alloy with at least 10.5% chromium is called SUS304, and it is renowned for its ability to resist corrosion as well as for being strong and long-lasting. It also has a low coefficient of thermal expansion and is resistant to high temperatures. The behavior of sediment containing hydrates is predicted using a multiphase constitutive model, which is then confirmed using test data [13]. Due to its corrosion resistance and mechanical strength, SUS304 is frequently utilized in micro/nanoelectromechanical systems [14–16]. A series of experiments were conducted to study the flow behavior of SUS304 under different forming conditions and the results were analyzed to understand the underlying reasons for the variations in flow behavior [17]. In the study [18], the impact of resin lamination on the tensile strength

of SUS304 stainless steel thin films was examined. It was discovered that while laminating polypropylene or polyethylene terephthalate films onto the SUS film did not significantly alter the strain or surface changes under tensile load, doing so did reduce the fracture strain, particularly in thin films. The study [19] investigated the SIMT behavior of commercial SUS304 metastable austenitic stainless steel with a focus on understanding the role of SFE on SIMT at higher strain rates. The steel was subjected to quasi-static and impact tensile tests to determine its relative magnetic permeability during deformation. A feedback loop for automation systems and material monitoring is created by analyzing the Long Period Grating Fiber Sensor inserted in a smart composite material for its reaction to mechanical vibrations. The simulation findings and experimental results are in excellent agreement [20].

Functionally graded materials (FGMs) are substances with a gradient in their composition or microstructure, which may cause a gradient in their mechanical and physical characteristics. Due to their capacity to tailor component properties for particular applications, these materials have been extensively used in a range of industries, from macroscale (vehicle, aviation, space and marine technologies, electronics, nuclear reactors, and biomedical engineering) to micro and nanoscale (micro/nano-electro-mechanical systems, shape memory alloys, and atomic force microscopes). By customizing the gradient of material characteristics to fulfill certain criteria, such as strength, stiffness, corrosion resistance, and thermal conductivity, FGMs have been employed on a larger scale to enhance the performance of components [21]. With a focus on how the shear stress and radial stress change with various pad contact areas and material property models, research employing finite element analysis examines the mechanical behavior of a functionally graded material braking disk under heat loading [22]. The study outlines a sound-wave-assisted vibrational casting process for producing FGMs with a gradient distribution of boron carbide (B₄C) particles in an aluminum matrix and examines the resultant microstructure and characteristics of the FGMs [23]. The research [24] explores the impact of volume fraction distributions on wave propagation and proposes higher-order shear deformation beam theories for functionally graded beams with possible applications in ultrasonic inspection and structural health monitoring. With possible applications in ultrasonic inspection and structural health monitoring, this study proposes plate theories for wave propagation in functionally graded plates with porosities, accounting for transverse shear deformation and changed material characteristics [25]. Using third-order shear deformation theory and Hamilton's principle, this study examines the natural frequencies of imperfectly functionally graded sandwich plates with porous face sheets and an isotropic homogeneous core that are supported by an elastic foundation. It also looks at the effects of porosity volume fraction, porosity distribution types, lay-up scheme, and side to thickness ratio on the non-dimensional fundamental natural frequency [26]. In order to predict crack behavior under extreme temperature conditions [27], a

thermal-mechanical coupling model for FGMs has been proposed. The model's accuracy and robustness have been verified through numerical tests, and it has been used to investigate the thermal cracking process in FGMs under various thermal loads. The influence of crack interaction on crack growth patterns has also been discussed. The mechanical characteristics of 6061 aluminum/SiC composite materials were examined in the work, and it was discovered that the SiC concentration and interlayer variation might greatly affect their tensile strength and elongation [28]. High-density bone issues with traditional implants may be effectively addressed with functionally graded material implants [29]. The FGMs were investigated for their behavior under thermal loads with various temperature profiles using the First Order Shear Deformation Theory (FSDT), and the outcomes were compared to previous research [30]. FGMs can be produced using various techniques and have many uses. They differ in their microstructure, content, or both, which affects how their characteristics change across their length or thickness [31]. For the first time, FGMs with hydroxyapatite (HA) and bioactive glass were produced using spark plasma sintering (SPS), employing two distinct series of FGMs with various compositions and microstructures that were created under optimal SPS conditions [32]. The approach described in the study [33] uses a quadrilateral finite element model and the Asymptotic Numerical Method (ANM) to examine the buckling and post-buckling behavior of a functionally graded material plate. The normal point contact between two elastic spheres with functionally graded material coatings is examined using a model the study [34], from which analytical solutions for the contact force and stress are derived. The study [31] proposes an innovative nature-inspired functionally graded lattice filled protection structure (FGLPS) to enhance the structural energy absorption characteristics of thin-walled structures under ship impact loadings. Moreover, the buckling behavior of a reinforced polyhedral liner under a point load is examined in the study [35]. The other FGMs studies have been given in [36].

FGMs have been used at the micro and nanoscale to enhance component performance by modifying the gradient of material characteristics to satisfy certain needs, such as electrical conductivity, magnetic qualities, and mechanical strength [37]. The study presents [38] the usage of a functionally graded magneto-electro-elastic nanoplate as a nano sensor, evaluates its sensitivity using a power law distribution model and a nonlocal Mindlin plate assumption, and takes into account different aspects that impact its frequency shift. Using the modified couple stress theory and refined zigzag theory, the research examines the impact of various parameters on the wave velocity of a micro-sandwich beam [39]. The nonlocal strain gradient theory and the Galerkin technique are used in the study [40] to look into the nonlinear forced vibrations of micro resonators. The other nonlinear vibration of the structures given in [41]. The study [42] uses a semi-analytical approach based on Eringen's nonlocal elasticity theory to examine the effects of various variables on the vibrational features of functionally graded nanobeams. Using a nonlocal theory and third-order parabolic

beam theory, the paper [43] offers a research on the thermo-electric-mechanical vibration behavior of functionally graded piezoelectric nanobeams and explores the influence of different parameters on the natural frequencies of the nanobeams. A novel three-dimensional framework has been established to analyze the thermo-electro-mechanical buckling of functionally graded piezoelectric cylindrical nano/micro-shells when they are compressed axially, subjected to an external applied voltage, and then uniformly heated [44]. The paper [45] investigates the nonlinear primary resonant dynamics of truncated conical microshells made of magnetostrictive material and with a functionally graded structure under an external magnetic field and mechanical excitation, using a microstructure-dependent model and numerical analysis method. The study [46] uses first-order shear deformation theory and nonlocal theory to examine the vibration behavior of a composite nanoplate with an attached mass-spring-damper system. It also looks at how different factors affect the system's natural frequency. Using numerical analysis and mathematical modeling, the study [47] examines the vibration response of thick microplates formed of porous exponentially functionally graded materials under accelerated moving loads. In order to increase performance and lower embodied carbon, the study [48] suggests a unique method that uses functionally graded concrete and voids to improve the mechanical and environmental performance of reinforced concrete buildings. Using Navier's approach, the bending and buckling of sandwich plates with various porosity laws were examined [49].

Numerous research has recently concentrated on the static and dynamic characterization of FG MEE structures comprised of piezoelectric and magnetic materials. MEE structures are composite materials with piezoelectric and magnetic capabilities that might be used as energy harvesters, sensors, and actuators [50]. The paper [6] uses a distributed parameter model and the modified Eshelby-Mori-Tanaka (EMT) approach to examine the impact of carbon nanotube (CNT) agglomeration on the energy harvesting behavior of a unimorph multifunctional cantilever beam (UMCB). In order to reduce the coupled nonlinear response of sandwich plates under various forms of loading, the study [51] examines the efficacy of a method known as active-controlled layer damping (ACLD). With potential applications in wave manipulation, communication systems, and electromagnetic stealth, the paper provides a PB phase metasurface-based polarizer for polarization control and radar cross section reduction [52]. The paper [53] reveals that skew angles and aspect ratios may significantly affect the behavior of SMEE plates, composite materials having both magnetic and electrical characteristics, and presents a model for understanding their behavior. The study [54] shows a finite element model for the static and dynamic analysis of functionally graded MEE plates and shells. These materials have continuously changing properties that are affected by a variety of physical phenomena, including magnetism, electricity, and mechanics. The study [55] looks at how different variables affect the thermal vibration and buckling behavior of a porous nanoplate constructed of functional grades of cobalt-

ferrite and barium-titanate. The paper proposes a method to address flutter instability in functionally graded plates subjected to supersonic airflow with any yawed angle, using the first-order shear deformation theory, physical spring technology, and characteristic orthogonal polynomials. The study [56] analyzes the critical angular velocity and frequency of an MEE rotary microdisk using modified couple stress theory and parametric analysis. The results demonstrate that external magnetic and electric fields can increase maximum deflection. By discretizing the domain with polygon meshes and representing the generalized intensity factors of stress, electric displacement, and magnetic induction fields analytically, the Scaled Boundary Finite Element Method (FEM) is a numerical method used to examine the fracture of magneto-electro-elastic materials [57]. The FSDT and the Voigt model are used in the paper to present a model for analyzing the vibrational and acoustic properties of magneto-electro-thermo-elastic functionally graded porous plates (METE-FGPPs). The model's convergence, accuracy, and adaptability are shown through comparison to previous findings and analysis of the impact of various parameters on the vibration and acoustic radiation of the METE-FGPPs [58]. In the study [59], the active vibration damping capabilities of the host structure are examined in relation to the employment of functionally graded piezoelectric materials as sensors and actuators for active vibration management of host structures.

Due to their magneto-electro-elastic characteristics, the researchers in the study decided to employ cobalt-ferrite (CoFe_2O_4) and barium-titanate (BaTiO_3) as the face layers of the nanoplate. These materials have two unique properties: piezoelectricity, which allows them to produce electrical charges under mechanical stress, and magnetostriction, which allows them to change form or size when exposed to a magnetic field. Due to these qualities, MEE materials have the potential to be beneficial in a variety of nanotechnology applications, such as sensors, actuators, and energy harvesting devices. The Si_3N_4 and SUS304, which are renowned for their strength, low density, and exceptional wear and corrosion resistance, are used to create the nanoplate's core. These characteristics make them appropriate for application in structural and wear-resistant components, as well as in MEMS and NEMS. The analysis of the nanoplate's thermo-mechanical vibration responses in the paper also makes use of higher-order shear deformation theory (HSDT). HSDT is a more sophisticated method of simulating the behavior of materials that considers how shear forces affect the material's deformation. The research intends to further knowledge of the behavior of magneto-electro-elastic materials and their possible applications in the realm of nanotechnology by integrating these unique materials and analytical methodologies.

2. Mathematical modelling

The Hamilton's approach, which is utilized to construct the equations of motion for magneto-electro-elastic face plates with functionally graded nanoplates, forms the foundation

of the mathematical model employed in this work. This enables the examination of the nanoplate's dynamic behavior and its reaction to thermal stresses, magneto-electro-elastic coupling, externally applied electric and magnetic fields, nonlocal characteristics, porosity volume fraction, and porosity fluctuation over thickness. The model accounts for the numerous characteristics of the nanoplate's constituent materials as well as their impact on the nanoplate's thermo-mechanical behavior.

2.1. Effective material properties of porous laminated nanoplate

Consider a three-layer rectangular plate, given in Figure 1, placed on a Cartesian coordinate system (x, y, z) having a (length) and b (width) lengths in x and y directions. Thus, the total thickness of the plate H_t is given by the summation of the core h and surface h_s layers as in the $H_t = h + 2h_s$ equation. Ω denotes the plate's middle plane for the undeformed case. Thus, the tensor $\Omega x = (-h_s - h/2, h/2 + h_s)$ stands for the plate's total domain border placed between the bottom ($z = -h_s - h/2$) and the top ($z = h_s + h/2$) surfaces and the edge $\bar{\Gamma}$. The curved surface Γ , defined by the tensor $\Gamma x (-h_s - h/2, h/2 + h_s)$, have an outward normal $\hat{n} = n_x \hat{e}_x + n_y \hat{e}_y$ with the n_x and n_y are the unit normal's direction cosines.

Pore development is a given in creating ceramic-based structures [60,61]. As a result, our analysis took into account a uniform porosity distribution over the thickness of the plate (as shown in Figure 2) using a porosity function provided in [62]. As a result, for the uniform porosity distribution example, Eq. (1) specifies an effective material attribute $P(z)$, presented in Table 1, based on the V_t volumetric fraction function, which represents a constituent's distribution over the thickness.

$$P(z) = [P_t - P_b]V_t + P_b - \frac{\alpha}{2}[P_t + P_b], \quad (1)$$

$$V_t = \left(\frac{2z+h}{2h}\right)^p, \quad V_t + V_b = 1$$

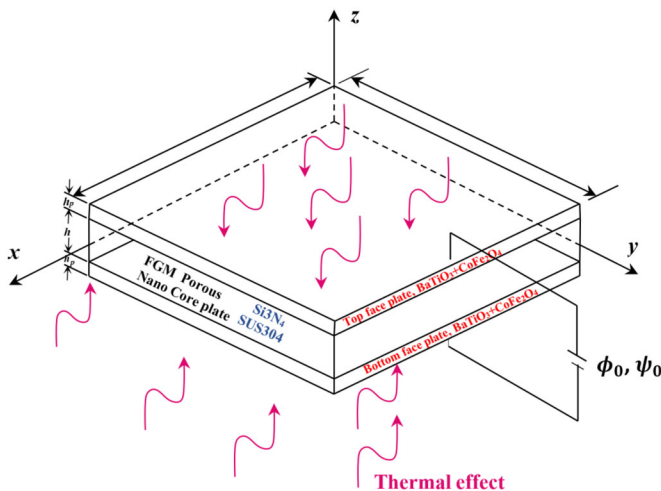


Figure 1. An FG higher-order nanoplate with porous structure and face layers under magnetic and thermal fields.

Here, P_b and P_t , respectively, stand for the material characteristics that make up the inferior and superior surfaces of the core plate. Except in the case of composite faceplates, P_b and P_t were assumed to be equal in the pure forms of the faceplates' $BaTiO_3$ and $CoFe_2O_4$ components. The total porosity volume fraction and power-law (material grading) index of the plate material is also implied by the parameters and p , respectively.

The material gradation index reflects the volume of materials composing the inferior and superior surfaces of the core plate along the core height. Thus, at $p=0$, the core face material will make up the whole core plate. The inferior face material's component reduces when p is raised, and when $p \rightarrow \infty$ is at its highest, the inferior face material makes up the whole core. According to the linear uniform porosity distribution, the Voight model results in [63,64]:

$$P(z) = [P_c - P_m]V_c + P_m - \frac{\alpha}{2}[P_c + P_m] \quad (2)$$

In which α is the material's total porosity as a percentage of volume. The effective characteristics of the center concentrated porosity model (Model 2) are defined by a nonlinear distribution function, where [62]:

$$P(z) = [(P_c - P_m)V_c + P_m] \left\{ 1 - \alpha \cos \left[\pi \frac{z}{h} \right] \right\} \quad (3)$$

The third model assumed that, as shown in Figure 2, porosity is concentrated at the bottom surface and diminishes higher. As a result, the porous material is ranked according to thickness as follows:

$$P(z) = [(P_c - P_m)V_c + P_m] \left\{ 1 - \alpha \cos \left[\frac{\pi}{2} \left(\frac{z}{h} + \frac{1}{2} \right) \right] \right\} \quad (4)$$

In terms of height, the final model is the opposite of the third and has the following characteristic:

$$P(z) = [(P_c - P_m)V_c + P_m] \left\{ 1 - \alpha \cos \left[\frac{\pi}{2} \left(\frac{z}{h} - \frac{1}{2} \right) \right] \right\} \quad (5)$$

In order to predict the behavior of the structure correctly, the impacts of temperature are thought to be required. Thus, the elastic modulus E_{ef} and the effective Poisson's ratio ν_{ef} the conductivity coefficients ψ_{ef} thermal expansion κ_{ef} and E_{ef} are considered temperature-related characteristics and may be characterized by a nonlinear temperature function [65,66].

$$P = P_0(P_{-1}T^{-1} + 1 + P_1T + P_2T^2 + P_3T^3) \quad (6)$$

Here, P represents any temperature T (K) dependent ingredient, and P_0 describes each material. P_{-1} , P_1 , P_2 , and P_3 values with orders (-1, 0, 1, 2, and 3) of the temperature T are shown in Table 2. The mass density $\rho(z)$ is simply a function of z and only moderately reliant on temperature changes, according to the effective material characteristics.

2.2. The nonlinear temperature increment

This section provides the relevant equations for uniform (UTR), linear (LTR), and nonlinear (NLTR) temperature rises throughout the nanorod's thickness. The whole body of

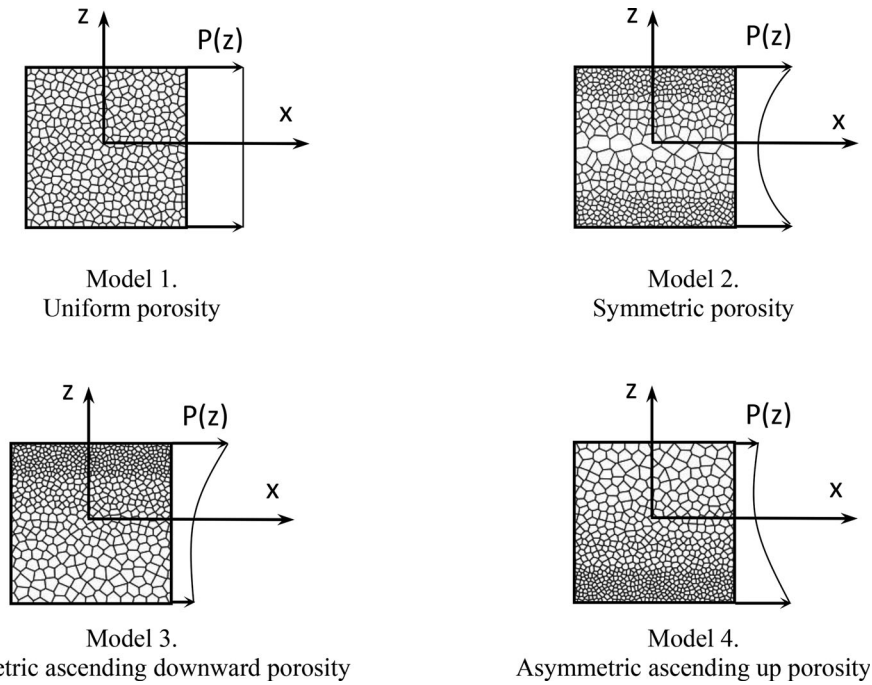


Figure 2. Models for the thickness-based distribution of porosity [61].

Table 1. Temperature dependent coefficients for the properties of CoFe_2O_4 and BaTiO_3 .

Material	Property	P_{-1}	P_0	P_1	P_2	P_3
CoFe_2O_4	C_{11} (Pa)	0	298.87e9	$-1.552e-4$	$6.125e-9$	$-9.0e-11$
	C_{55} (Pa)	0	47.33e9	$-1.552e-4$	$6.125e-9$	$-9.0e-11$
	ν	0	0.3	0	0	0
	α (1K^{-1})	0	$7.5e-6$	$-3.01e-4$	$4.02e-6$	$-1.01e-09$
	κ (W/mK)	0	4.7030	-0.0011	$1.6612e-06$	$-9.9670e-10$
	ρ (kg/m^3)	0	5300	0	0	0
BaTiO_3	C_{11} (Pa)	0	174e9	$-1.552e-4$	$6.125e-9$	$-9.0e-11$
	C_{55} (Pa)	0	44.93e9	$-1.552e-4$	$6.125e-9$	$-9.0e-11$
	ν	0	0.30	0	0	0
	α (1K^{-1})	0	$10e-6$	$-3.0e-4$	$4.0e-6$	$-1.0e-09$
	κ (W/mK)	0	3.7624	$-8.50521e-4$	$1.32894e-06$	$-7.97363e-10$
	ρ (kg/m^3)	0	5800	0	0	0

an FGM nanobeam with a starting temperature of $T_0 = 300\text{K}$ is uniformly increased to its ultimate temperature T , using the following equation in a stress-free condition with uniform temperature rise (UTR):

$$\Delta T = T - T_0 \quad (7)$$

The temperature of a plane extending down the z -direction may be calculated using the following equation [59] given the temperatures of the bottom and top surfaces, T_b and T_t , respectively, and assuming that the temperature rises linearly (LTR) from T_b to T_t along the thickness [67]:

$$T(z) = T_b + (T_t - T_b) \left(\frac{h + 2z}{2h} \right) \quad (8)$$

In the case of nonlinear temperature rises (NLTR) across the thickness, the top T_t and bottom T_b surfaces of the nanobeam may be determined by solving the steady-state one-dimensional heat transfer equation below with known temperature boundary conditions [68].

$$-\frac{d}{dz} \left(\kappa(z) \frac{dT}{dz} \right) = 0, \quad T\left(\frac{h}{2}\right) = T_t, \quad T\left(-\frac{h}{2}\right) = T_b \quad (9a)$$

Consequently, the temperature at any z extending along the thickness for a specified boundary condition is:

$$T(z) = T_b + \frac{(T_t - T_b)}{\int_{-\frac{h}{2}}^{\frac{h}{2}} \frac{1}{\psi(z)} dz} \int_{-\frac{h}{2}}^z \psi(z) dz \quad (9b)$$

2.3. Review of the nonlocal strain gradient theory (NSGT) for the MEE material

The stress at one point of a continuum body is assumed in Eringen's study [69] to be a function of the stresses at all other places. According to this hypothesis, the stiffness of the structure varies depending on the strength of nonlocal and material scale effects. In this sense, depending on the size of the nonlocal influence, the structure behaves more smoothly than classical forms. The strain gradient hypothesis, on the other hand, only considers the material scale effect as increasing the stiffness of the structure. Thus, the nonlocal elasticity theory and Eringen's strain gradient theory distinguish two different physical phenomena. These two separate factors are concurrently taken into account by

Table 2. The magnetic, piezo, electro, and thermal properties of CoFe₂O₄ and BaTiO₃.

		CoFe ₂ O ₄	BaTiO ₃
C ₁₁	(GPa)	286	166
C ₂₂		286	166
C ₃₃		269.5	162
C ₁₂		173	77
C ₁₃		170.5	78
C ₂₃		170.5	78
C ₄₄		45.3	43
C ₅₅		45.3	43
C ₆₆		56.5	44.5
e ₃₁	(C/m ²)	0	-4.4
e ₃₂		0	-4.4
e ₃₃		0	18.6
q ₃₁	(N/A.m)	580.3	0
q ₃₂		580.3	0
q ₃₃		699.7	0
ξ ₁₁	(10 ⁻⁹ C ² /N.m ²)	0.08	11.2
ξ ₂₂		0.08	11.2
ξ ₃₃		0.093	12.6
ζ ₁₁ = ζ ₂₂ = ζ ₃₃	(s/m)	0	0
λ ₁₁	(10 ⁻⁶ N.s ² /C)	-590	5
λ ₂₂		-590	5
λ ₃₃		157	10
p ₁₁ = p ₂₂	(10 ⁻⁷ C/m ² K)	0	0
p ₃₃		0	-11.4
λ ₁₁ = λ ₂₂	(10 ⁻⁵ Wb/m ² K)	0	0
λ ₃₃		-36.2	0
α ₁ = α ₂	(10 ⁻⁶ K ⁻¹)	10	15.8
ρ	(kg/m ³)	5800	5300

the NSGT to reflect the nonlocality [70,71]. The classical σ and higher-order $\sigma^{(h)}$ stress tensors in NSGT are described by the equations given below [70]:

$$\sigma = \int_V \alpha_0(\mathbf{x}', \mathbf{x}, e_0 a) \mathbf{C} : \varepsilon'(\mathbf{x}') dV' \quad (10)$$

$$\sigma^{(h)} = l_m^2 \int_V \alpha_1(\mathbf{x}', \mathbf{x}, e_1 a) \mathbf{C} : \nabla \varepsilon'(\mathbf{x}') dV' \quad (11)$$

where, classical kernel and higher-order nonlocal functions are α_0 and α_1 , respectively. Additionally, the Laplacian operator ($\nabla = \partial/\partial x + \partial/\partial y$) and fourth-order material coefficient are denoted by the letters ∇ and \mathbf{C} , respectively. The terms $\nabla \varepsilon$ and ε and imply the classical strain tensors and the strain gradient. Besides, $e_0 a$ and $e_1 a$ indicate the nonlocality constants with the e_1 and e_0 material coefficients, and a represents the atomics bonds geometrical characteristics. The l_m is the material size parameter and the colon symbol “:” indicates the tensor’s double-dot production. Thus, the whole stress tensor based on the NSGT is expressed by [70, 72]:

$$\sigma^t = \sigma - \nabla^2 \sigma^{(1)} \quad (12)$$

Assuming compatible $\alpha_1(\mathbf{x}', \mathbf{x}, e_1 a)$ and $\alpha_0(\mathbf{x}', \mathbf{x}, e_0 a)$ notions with Ref. [73] and equaling $e_0 = e_1 = e_0 a$, and utilizing the linear differentiation operator to Eq. (4) gives:

$$[1 - (e_0 a)^2 \nabla^2] \sigma = \mathbf{C} : \varepsilon \quad (13)$$

$$[1 - (e_0 a)^2 \nabla^2] \sigma^{(1)} = l_m^2 \mathbf{C} : \nabla \varepsilon \quad (14)$$

Equations (4–6) may be used to get the following total stress:

$$[1 - (e_0 a)^2 \nabla^2] \sigma = \mathbf{C} : \varepsilon - l_m^2 \nabla \mathbf{C} : \nabla \varepsilon \quad (15)$$

The plate’s stress-strain relations are determined by [70,71]:

$$\begin{aligned} [1 - (e_0 a)^2 \nabla^2] \sigma_{xx} &= [1 - l_m^2 \nabla^2] E(z) \varepsilon_{xx} \\ [1 - (e_0 a)^2 \nabla^2] \sigma_{yy} &= [1 - l_m^2 \nabla^2] E(z) \varepsilon_{yy} \\ [1 - (e_0 a)^2 \nabla^2] \sigma_{xz} &= [1 - l_m^2 \nabla^2] G(z) \gamma_{xz} \\ [1 - (e_0 a)^2 \nabla^2] \sigma_{yz} &= [1 - l_m^2 \nabla^2] G(z) \gamma_{yz} \end{aligned} \quad (16)$$

where respectively, σ_{xx} , σ_{yy} and ε_{xx} , ε_{yy} , denote the usual stresses and strains in the x and y directions. Additionally, the shear stresses and strains in the xz - and yz -planes are represented by σ_{xz} , σ_{yz} , and γ_{xz} , γ_{yz} . $E(z)$ and $G(z)$ stand for elasticity and shear modulus, respectively. When the l_m and $e_0 a$ in Eq. (8) are equal to 0, the stress-strain relations of the classical continuum theory may be found [73]. Finally, taking into account the magneto-electro elastic characteristics, the constitutive equations of the NGST microplate under thermal loads may be set up as in the following structure:

$$\begin{aligned} \sigma(x, y, z)(1 - e_0 a^2 \nabla^2) &= (1 - l_m^2 \nabla^2) \\ &[\bar{\mathbf{Q}}(z) \boldsymbol{\varepsilon} - \tilde{\mathbf{e}}(z) \mathbf{E} - \tilde{\mathbf{q}}(z) \mathbf{H}] - \bar{\mathbf{Q}}(z) \boldsymbol{\alpha}(z) \Delta T \\ \mathbf{D}_E(x, y, z)(1 - e_0 a^2 \nabla^2) &= (1 - l_m^2 \nabla^2) \\ &[\tilde{\mathbf{e}}^{\square}(z) \boldsymbol{\varepsilon} - \tilde{\boldsymbol{\xi}}(z) \mathbf{E} + \tilde{\boldsymbol{\zeta}}(z) \mathbf{H}] - \mathbf{p}(z) \Delta T \\ \mathbf{B}_M(x, y, z)(1 - e_0 a^2 \nabla^2) &= (1 - l_m^2 \nabla^2) \\ &[\tilde{\mathbf{q}}^{\square}(z) \boldsymbol{\varepsilon} + \tilde{\boldsymbol{\zeta}}(z) \mathbf{E} + \tilde{\boldsymbol{\chi}}(z) \mathbf{H}] - \boldsymbol{\lambda}(z) \Delta T \end{aligned} \quad (17)$$

2.4. Displacement fields and strains

The sinusoidal higher-order shear deformation theory (SHSDT), which is applied to a three-layer rectangular plate, is predicated on the assumptions listed below [74],

1. Because the displacements are negligible in relation to the thickness of the plate, the corresponding stresses are infinitesimally small.
2. The plane u and v displacements contain the components for extension u_0 , shear w_s , and bending w_0 .
3. The transverse displacement w is adjusted to take into account the bending w_0 , shear w_s , and stretching w_{st} components of the transverse stresses (σ_{xz} , σ_{yz} , σ_{zz}) and strains (ε_{xz} , ε_{yz} , ε_{zz}).
4. There is an increase in the trigonometric variation of the shear stresses (σ_{xz} , σ_{yz}) and strains (ε_{xz} , ε_{yz}) along the thickness of the plate when the shear components (w_s in u , v in-plane, and w transverse displacements) are included. As a result, there are no shear stresses (σ_{xz} , σ_{yz}) on the plate’s top and bottom faces.

Taking into account the presumptions described above for the full form of the SHSDT, the displacement field of the nanoplate is defined as follows:

$$u(x, y, z, t) = u_0(x, y, t) - z \frac{\partial w_0(x, y, t)}{\partial x} - f(z) \frac{\partial w_s(x, y, t)}{\partial x} \quad (18a)$$

$$v(x, y, z, t) = v_0(x, y, t) - z \frac{\partial w_0(x, y, t)}{\partial y} - f(z) \frac{\partial w_s(x, y, t)}{\partial y} \quad (18b)$$

$$w(x, y, z, t) = w_0(x, y, t) + w_s(x, y, t) + w_{st}(x, y, z, t) \quad (18c)$$

Here $f(z)$, w_{st} and $g(z)$ defined as:

$$f(z) = z - \frac{H_t}{\pi} \sin \left(\frac{\pi z}{H_t} \right) \quad (19)$$

$$w_{st}(x, y, z, t) = g(z)\vartheta(x, y, t) \quad (20)$$

$$g(z) = \cos \left(\frac{\pi z}{H_t} \right) \quad (21)$$

The terms u , v , and w in the displacement equations above stand for the total displacements of a point in an undeformed body. The unknown in-plane and transverse displacements of a point on the undeformed plate's midplane $(x, y, 0)$ at any time t are denoted by the symbols u_0 , v_0 , and w_0 . Here, the plate's u and v displacements are connected to its extensional deformation, whereas the w displacement indicates its bending deflection. The general form of the strain-displacement interactions associated with the displacement field in Eq. (10) is as follows:

$$\begin{Bmatrix} \varepsilon_{xx} \\ \varepsilon_{yy} \\ 2\varepsilon_{xy} \end{Bmatrix} = \begin{Bmatrix} \varepsilon_{xx}^{(0)} \\ \varepsilon_{yy}^{(0)} \\ \gamma_{xy}^{(0)} \end{Bmatrix} + z \begin{Bmatrix} \varepsilon_{xx}^{(b)} \\ \varepsilon_{yy}^{(b)} \\ \gamma_{xy}^{(s)} \end{Bmatrix} + f(z) \begin{Bmatrix} \varepsilon_{xx}^{(s)} \\ \varepsilon_{yy}^{(s)} \\ \gamma_{xy}^{(s)} \end{Bmatrix} \quad (22a)$$

$$\begin{Bmatrix} 2\varepsilon_{xz} \\ 2\varepsilon_{yz} \end{Bmatrix} = g(z) \begin{Bmatrix} \gamma_{xz}^{(0)} \\ \gamma_{yz}^{(0)} \end{Bmatrix} \quad (22b)$$

$$\varepsilon_{zz} = g'(z)\varepsilon_{zz}^{(0)} \quad (22c)$$

Also, the particular strain components are as follows:

$$\begin{Bmatrix} \varepsilon_{xx}^{(0)} \\ \varepsilon_{yy}^{(0)} \\ \gamma_{xy}^{(0)} \end{Bmatrix} = \begin{Bmatrix} \frac{\partial u_0}{\partial x} \\ \frac{\partial v_0}{\partial y} \\ \frac{\partial u_0}{\partial y} + \frac{\partial v_0}{\partial x} \end{Bmatrix}, \quad \begin{Bmatrix} \varepsilon_{xx}^{(b)} \\ \varepsilon_{yy}^{(b)} \\ \gamma_{xy}^{(b)} \end{Bmatrix} = \begin{Bmatrix} -\frac{\partial^2 w_0}{\partial x^2} \\ -\frac{\partial^2 w_0}{\partial y^2} \\ -2\frac{\partial^2 w_0}{\partial x \partial y} \end{Bmatrix} \quad (23a)$$

$$\begin{Bmatrix} \varepsilon_{xx}^{(s)} \\ \varepsilon_{yy}^{(s)} \\ \gamma_{xy}^{(s)} \end{Bmatrix} = \begin{Bmatrix} -\frac{\partial^2 w_s}{\partial x^2} \\ -\frac{\partial^2 w_s}{\partial y^2} \\ -2\frac{\partial^2 w_s}{\partial x \partial y} \end{Bmatrix} \quad (23b)$$

$$\begin{Bmatrix} \gamma_{xz}^{(0)} \\ \gamma_{yz}^{(0)} \end{Bmatrix} = \begin{Bmatrix} (1 - f'(z)) \frac{\partial w_s}{\partial x} + g(z) \frac{\partial \vartheta}{\partial x} \\ (1 - f'(z)) \frac{\partial w_s}{\partial y} + g(z) \frac{\partial \vartheta}{\partial y} \end{Bmatrix} = \begin{Bmatrix} g(z) \left(\frac{\partial w_s}{\partial x} + \frac{\partial \vartheta}{\partial x} \right) \\ g(z) \left(\frac{\partial w_s}{\partial y} + \frac{\partial \vartheta}{\partial y} \right) \end{Bmatrix}$$

$$\varepsilon_{zz}^{(0)} = \vartheta \quad (23c)$$

2.5. Constitutive equations

In the study, a linear elastic nanoplate with an isotropic core encased by top and bottom surface layers is considered. The functional grading of the barium-titanate and cobalt-ferrite elements was used to organize the nanoplate’s core, while pure or homogenous mixes of these materials were used to create the surface layers. The constitutive relations of the isotropic core plate may be defined as follows using the differential version of Eringen’s constitutive relations Eq. (3):

$$\begin{aligned}
 & \begin{Bmatrix} \mathcal{L}(\sigma_{xx}^c) \\ \mathcal{L}(\sigma_{yy}^c) \\ \mathcal{L}(\sigma_{zz}^c) \\ L(\sigma_{yz}^c) \\ L(\sigma_{xz}^c) \\ L(\sigma_{xy}^c) \end{Bmatrix} = \begin{bmatrix} C_{11}^c & C_{12}^c & C_{13}^c & 0 & 0 & 0 \\ C_{12}^c & C_{22}^c & C_{23}^c & 0 & 0 & 0 \\ C_{13}^c & C_{23}^c & C_{33}^c & 0 & 0 & 0 \\ 0 & 0 & 0 & C_{44}^c & 0 & 0 \\ 0 & 0 & 0 & 0 & C_{55}^c & 0 \\ 0 & 0 & 0 & 0 & 0 & C_{66}^c \end{bmatrix} \begin{Bmatrix} \varepsilon_{xx} \\ \varepsilon_{yy} \\ \varepsilon_{zz} \\ 2\varepsilon_{yz} \\ 2\varepsilon_{xz} \\ 2\varepsilon_{xy} \end{Bmatrix} \\
 & - \begin{bmatrix} 0 & 0 & e_{31} \\ 0 & 0 & e_{32} \\ 0 & 0 & e_{33} \\ 0 & e_{24} & 0 \\ e_{15} & 0 & 0 \\ 0 & 0 & 0 \end{bmatrix} \begin{Bmatrix} E_x \\ E_y \\ E_z \end{Bmatrix} - \begin{bmatrix} 0 & 0 & q_{31} \\ 0 & 0 & q_{32} \\ 0 & 0 & q_{33} \\ 0 & q_{24} & 0 \\ q_{15} & 0 & 0 \\ 0 & 0 & 0 \end{bmatrix} \begin{Bmatrix} H_x \\ H_y \\ H_z \end{Bmatrix}
 \end{aligned} \tag{24}$$

Here C_{ij}^n stands for the stiffness coefficients and are defined by:

$$C_{11}^c = \frac{1 - \nu}{\nu} \lambda(z) \tag{25a}$$

$$C_{12}^c = \lambda(z) \tag{25b}$$

$$C_{66}^c = \mu(z) \tag{25c}$$

$$C_{11}^c = C_{22}^c = C_{33}^c \tag{25d}$$

$$C_{12}^c = C_{13}^c = C_{23}^c \tag{25e}$$

$$C_{44}^c = C_{55}^c = C_{66}^c \tag{25f}$$

In stiffness coefficients, the $\lambda(z)$ and $\mu(z)$ are the Lamé constants ($\lambda(z) = \frac{\nu E(z)}{(1+\nu)(1-2\nu)}$, $\mu(z) = \frac{E(z)}{2(1+\nu)}$). Additionally, a constant Poisson’s ratio is assumed, and Young’s modulus changes along the core plate’s thickness h ($-h/2 \leq z \leq h/2$) related to a power-law as defined in [75].

$$E(z) = (E_t - E_b) \left(\frac{z}{h} + \frac{1}{2} \right)^p + E_b \tag{26}$$

The top and bottom surfaces’ respective Young’s moduli are represented by E_t and E_b , respectively, while p is the material grading index. Applying the nonlocal and strain-gradient differential operators, the constitutive relations of the surface layers are described by [76]. $\mathcal{L}(\ast) \equiv 1 - (e_0 a)^2 \nabla^2$ and $\Gamma(\ast) \equiv 1 - (l_m)^2 \nabla^2$.

$$\begin{aligned}
 & \begin{Bmatrix} \mathcal{L}(\sigma_{xx}^s) \\ \mathcal{L}(\sigma_{yy}^s) \\ \mathcal{L}(\sigma_{zz}^s) \\ L(\sigma_{yz}^s) \\ L(\sigma_{xz}^s) \\ L(\sigma_{xy}^s) \end{Bmatrix} = \Gamma \begin{bmatrix} C_{11}^s & C_{12}^s & C_{13}^s & 0 & 0 & 0 \\ C_{12}^s & C_{22}^s & C_{23}^s & 0 & 0 & 0 \\ C_{13}^s & C_{23}^s & C_{33}^s & 0 & 0 & 0 \\ 0 & 0 & 0 & C_{44}^s & 0 & 0 \\ 0 & 0 & 0 & 0 & C_{55}^s & 0 \\ 0 & 0 & 0 & 0 & 0 & C_{66}^s \end{bmatrix} \begin{Bmatrix} \varepsilon_{xx} \\ \varepsilon_{yy} \\ \varepsilon_{zz} \\ 2\varepsilon_{yz} \\ 2\varepsilon_{xz} \\ 2\varepsilon_{xy} \end{Bmatrix} - \\
 & -\Gamma \begin{bmatrix} 0 & 0 & e_{31} \\ 0 & 0 & e_{32} \\ 0 & 0 & e_{33} \\ 0 & e_{24} & 0 \\ e_{15} & 0 & 0 \\ 0 & 0 & 0 \end{bmatrix} \begin{Bmatrix} E_x \\ E_y \\ E_z \end{Bmatrix} - \Gamma \begin{bmatrix} 0 & 0 & q_{31} \\ 0 & 0 & q_{32} \\ 0 & 0 & q_{33} \\ 0 & q_{24} & 0 \\ q_{15} & 0 & 0 \\ 0 & 0 & 0 \end{bmatrix} \begin{Bmatrix} H_x \\ H_y \\ H_z \end{Bmatrix}
 \end{aligned} \tag{27a}$$

$$\begin{aligned} \begin{Bmatrix} \mathcal{L}(D_x) \\ \mathcal{L}(D_y) \\ \mathcal{L}(D_z) \end{Bmatrix} &= \Gamma \begin{bmatrix} 0 & 0 & 0 & 0 & e_{15} & 0 \\ 0 & 0 & 0 & e_{24} & 0 & 0 \\ e_{31} & e_{32} & e_{33} & 0 & 0 & 0 \end{bmatrix} \begin{Bmatrix} \varepsilon_{xx} \\ \varepsilon_{yy} \\ \varepsilon_{zz} \\ 2\varepsilon_{yz} \\ 2\varepsilon_{xz} \\ 2\varepsilon_{xy} \end{Bmatrix} + \Gamma \begin{bmatrix} \varepsilon_{11} & 0 & 0 \\ 0 & \varepsilon_{22} & 0 \\ 0 & 0 & \varepsilon_{33} \end{bmatrix} \begin{Bmatrix} E_x \\ E_y \\ E_z \end{Bmatrix} + \\ &+ \Gamma \begin{bmatrix} g_{11} & 0 & 0 \\ 0 & g_{22} & 0 \\ 0 & 0 & g_{33} \end{bmatrix} \begin{Bmatrix} H_x \\ H_y \\ H_z \end{Bmatrix} \end{aligned} \quad (27b)$$

$$\begin{aligned} \begin{Bmatrix} \mathcal{L}(B_x) \\ \mathcal{L}(B_y) \\ \mathcal{L}(B_z) \end{Bmatrix} &= \Gamma \begin{bmatrix} 0 & 0 & 0 & 0 & q_{15} & 0 \\ 0 & 0 & 0 & q_{24} & 0 & 0 \\ q_{31} & q_{32} & q_{33} & 0 & 0 & 0 \end{bmatrix} \begin{Bmatrix} \varepsilon_{xx} \\ \varepsilon_{yy} \\ \varepsilon_{zz} \\ 2\varepsilon_{yz} \\ 2\varepsilon_{xz} \\ 2\varepsilon_{xy} \end{Bmatrix} + \Gamma \begin{bmatrix} \varepsilon_{11} & 0 & 0 \\ 0 & \varepsilon_{22} & 0 \\ 0 & 0 & \varepsilon_{33} \end{bmatrix} \begin{Bmatrix} E_x \\ E_y \\ E_z \end{Bmatrix} + \\ &+ \Gamma \begin{bmatrix} \mu_{11} & 0 & 0 \\ 0 & \mu_{22} & 0 \\ 0 & 0 & \mu_{33} \end{bmatrix} \begin{Bmatrix} H_x \\ H_y \\ H_z \end{Bmatrix} \end{aligned} \quad (27c)$$

By establishing the electric $\check{\varphi}$ and magnetic potentials $\check{\psi}$, the constitutive relations may be defined in their entirety. The components of electric E_i and magnetic fields H_i are expressed using these three-dimensional potentials.

$$E_i = \{-\check{\varphi}_{,i}\}, \quad H_i = \{-\check{\psi}_{,i}\}, \quad i = x, y, z \quad (28)$$

According to Maxwell's equations, the distributions of these potentials for a nanoplate activated with initial external electric φ_0 and magnetic ψ_0 potentials are characterized by fuzing the linear and cosine functions as in the following [77,78]:

$$\begin{Bmatrix} \check{\varphi}(x, y, z, t) \\ \check{\psi}(x, y, z, t) \end{Bmatrix} = \begin{Bmatrix} \varphi_0 \\ \psi_0 \end{Bmatrix} \frac{2\hat{z}}{H_t} - \begin{Bmatrix} \varphi(x, y, t) \\ \psi(x, y, t) \end{Bmatrix} \cos\left(\frac{\pi\hat{z}}{H_t}\right) \quad (29)$$

Here $\varphi(x, y, t)$ and $\psi(x, y, t)$, in turn, imply the time-dependent planar electric and magnetic potential distributions. Furthermore, the \hat{z} variable stands for the thickness of the surface-layers ($\hat{z} = z \pm h/2 \pm h_s/2$). For the plate's top layer \hat{z} is defined as $\hat{z} \equiv z_1 = z - h/2 - h_s/2$, whereas \hat{z} is defined as $\hat{z} \equiv z_2 = z + h/2 + h_s/2$ for the plate's bottom layer. Note that, z is only valid for $(h/2 \leq z \leq h/2 + h_s/2)$ and $(-h/2 - h_s/2 \leq z \leq -h/2)$.

2.6. Equations of motion

By using the following virtual displacements, Hamilton's principle may be altered for the motion equations of the three-layered rectangular nanoplate [79]:

$$\int_0^T (\delta\mathcal{U} - \delta\mathcal{E} - \delta\mathcal{M} - \delta\mathcal{K} + \delta\mathcal{V}) dt = 0 \quad (30)$$

Here, $\delta\mathcal{U}$, $\delta\mathcal{K}$, and $\delta\mathcal{V}$ are, in turn, the virtual forms of strain energy, kinetic energy, and work done by external forces. Additionally, $\delta\mathcal{E}$ and $\delta\mathcal{M}$ are the electric and magnetic fields' virtual contributions. Accordingly, the virtual strain energy $\delta\mathcal{U}$ is defined by

$$\begin{aligned} \delta\mathcal{U} &= \int_{\Omega} \left[\int_{-h/2-h_s}^{-h/2} (\sigma_{xx}^s \delta\varepsilon_{xx} + \sigma_{yy}^s \delta\varepsilon_{yy} + \sigma_{zz}^s \delta\varepsilon_{zz} + 2\sigma_{yz}^s \delta\varepsilon_{yz} + 2\sigma_{xz}^s \delta\varepsilon_{xz} + 2\sigma_{xy}^s \delta\varepsilon_{xy}) dz \right. \\ &+ \int_{-h/2}^{h/2} (\sigma_{xx}^c \delta\varepsilon_{xx} + \sigma_{yy}^c \delta\varepsilon_{yy} + \sigma_{zz}^c \delta\varepsilon_{zz} + 2\sigma_{yz}^c \delta\varepsilon_{yz} + 2\sigma_{xz}^c \delta\varepsilon_{xz} + 2\sigma_{xy}^c \delta\varepsilon_{xy}) dz \\ &\left. + \int_{h/2}^{h/2+h_f} ((\sigma_{xx}^s \delta\varepsilon_{xx} + \sigma_{yy}^s \delta\varepsilon_{yy} + \sigma_{zz}^s \delta\varepsilon_{zz} + 2\sigma_{yz}^s \delta\varepsilon_{yz} + 2\sigma_{xz}^s \delta\varepsilon_{xz} + 2\sigma_{xy}^s \delta\varepsilon_{xy}) dz) \right] dx dy \end{aligned} \quad (31)$$

Additionally, the electric $\delta\mathcal{E}$ and magnetic $\delta\mathcal{M}$ fields' contributions are given by:

$$\delta\mathcal{E} = \int_{\Omega} \left[\int_{-h/2-h_s}^{-h/2} (D_x \delta E_x + D_y \delta E_y + D_z \delta E_z) dz + \int_{-h/2}^{h/2} (D_x \delta E_x + D_y \delta E_y + D_z \delta E_z) dz + \int_{h/2}^{h/2+h_s} (D_x \delta E_x + D_y \delta E_y + D_z \delta E_z) dz \right] dx dy \quad (32)$$

$$\delta\mathcal{M} = \int_{\Omega} \left[\int_{-h/2-h_s}^{-h/2} (B_x\delta H_x + B_y\delta H_{y+}B_z\delta H_z)dz + \int_{-h/2}^{h/2} (B_x\delta H_x + B_y\delta H_{y+}B_z\delta H_z)dz + \int_{h/2}^{h/2+h_s} (B_x\delta H_x + B_y\delta H_{y+}B_z\delta H_z)dz \right] dx dy \tag{33}$$

Also, the contribution of the kinetic energy is as follows:

$$\delta\mathcal{K} = \int_{\Omega} \left[\int_{-h/2-h_s}^{-h/2} \rho^f(\dot{u}\delta\dot{u} + \dot{v}\delta\dot{v} + \dot{w}\delta\dot{w})dz + \int_{-h/2}^{h/2} \rho^c(z)(\dot{u}\delta\dot{u} + \dot{v}\delta\dot{v} + \dot{w}\delta\dot{w})dz + \int_{h/2}^{h/2+h_s} \rho^f(\dot{u}\delta\dot{u} + \dot{v}\delta\dot{v} + \dot{w}\delta\dot{w})dz \right] dx dy \tag{34}$$

Here $\rho^f(z)$ and $\rho^c(z)$, in turn, stand for the mass densities of nanoplate’s surface layers and core defined by the power-law equation as:

$$\rho^c(z) = (\rho_t^c - \rho_b^c) \left(\frac{z}{h} + \frac{1}{2} \right)^p + \rho_b^c \tag{35}$$

where the values ρ_t^c and ρ_b^c represent the mass densities of the superior and inferior core surfaces, respectively. Additionally, a variable’s time derivative is implied by a dot superscript, such as in the expression $\dot{u} = \partial u / \partial t$. The following summarizes how in-plane external pressures contribute to virtual work:

$$\delta\mathcal{V} = - \int_{\Omega} \left[(N_{xx0} + N_{xx\mathcal{E}} + N_{xx\mathcal{M}}) \frac{\partial w_0}{\partial x} \frac{\partial \delta w_0}{\partial x} + (N_{yy0} + N_{yy\mathcal{E}} + N_{yy\mathcal{M}}) \frac{\partial w_0}{\partial y} \frac{\partial \delta w_0}{\partial y} \right] dx dy \tag{36}$$

Here, the 0, \mathcal{E} , and \mathcal{M} subscripts represent the in-plane compressive mechanical, electrical, and magnetic forces. Clearly, $N_{xx0} = P_{x0}$ and $N_{yy0} = P_{y0}$ are compressive mechanical forces, $N_{xx\mathcal{M}} = P_{q31}$ and $N_{yy\mathcal{M}} = P_{q32}$ are the magnetic forces arising from magnetic potential, and $N_{xx\mathcal{E}} = P_{e31}$ and $N_{yy\mathcal{E}} = P_{e32}$ are the electric forces resulting from by external electric voltage. The virtual work equation disregards the mechanical forces applied to the top and lower surfaces since the study only looks at MEE nanoplates’ free vibration and buckling responses. Assume that the plate buckles with cylindrical bending behavior when an external force is applied along its midplane. In that instance, only the deflection’s bending (w_0) component is connected to the externally applied axial forces. Additionally, the overall behavior of the plate will be influenced by the deflection’s shear (w_s) and stretch (w_{st}) components. The resulting forces and moments that are linked to thickness may then be expressed as follows:

$$\begin{aligned} \begin{Bmatrix} N_{xx} & N_{yy} & N_{xy} \\ M_{xx}^{(b)} & M_{yy}^{(b)} & M_{xy}^{(b)} \\ M_{xx}^{(s)} & M_{yy}^{(s)} & M_{xy}^{(s)} \end{Bmatrix} &= \int_{-h/2-h_s}^{-h/2} (\sigma_{xx}^s, \sigma_{yy}^s, \sigma_{xy}^s) \begin{Bmatrix} 1 \\ z \\ f(z) \end{Bmatrix} dz + \\ &+ \int_{-h/2}^{h/2} (\sigma_{xx}^c, \sigma_{yy}^c, \sigma_{xy}^c) \begin{Bmatrix} 1 \\ z \\ f(z) \end{Bmatrix} dz + \int_{h/2}^{h/2+h_s} (\sigma_{xx}^s, \sigma_{yy}^s, \sigma_{xy}^s) \begin{Bmatrix} 1 \\ z \\ f(z) \end{Bmatrix} dz \end{aligned} \tag{37a}$$

$$N_{zz} = \int_{-h/2-h_s}^{h/2} \sigma_{zz}^s g'(z) dz + \int_{-h/2}^{h/2} \sigma_{zz}^c g'(z) dz + \int_{h/2}^{h/2+h_s} \sigma_{zz}^s g'(z) dz \tag{37b}$$

$$\{S_{xz}, S_{yz}\} = \int_{-h/2-h_s}^{-h/2} \{\sigma_{xz}^s, \sigma_{yz}^s\} g(z) dz + \int_{-h/2}^{h/2} \{\sigma_{xz}^c, \sigma_{yz}^c\} g(z) dz + \int_{h/2}^{h/2+h_s} \{\sigma_{xz}^s, \sigma_{yz}^s\} g(z) dz \tag{37c}$$

Also, the virtual strain energy gets the following form:

$$\begin{aligned} \delta\mathcal{U} = \int_{\Omega} &(N_{xx}\delta\varepsilon_{xx}^{(0)} + N_{yy}\delta\varepsilon_{yy}^{(0)} + N_{zz}\delta\varepsilon_{zz}^{(0)} + N_{xy}\delta\varepsilon_{xy}^{(0)} + N_{xz}\delta\varepsilon_{xz}^{(0)} + N_{yz}\delta\varepsilon_{yz}^{(0)} + M_{xx}\delta\varepsilon_{xx}^{(b)} + M_{yy}\delta\varepsilon_{yy}^{(b)} + M_{xy}\delta\varepsilon_{xy}^{(b)} + M_{xx}\delta\varepsilon_{xx}^{(s)} \\ &+ M_{yy}\delta\varepsilon_{yy}^{(s)} + M_{xy}\delta\varepsilon_{xy}^{(s)}) dx dy \end{aligned} \tag{38}$$

Additionally, the thickness-related electric \bar{D}_i ($i = x, y, z$) and magnetic \bar{B}_i ($i = x, y, z$) coefficients are given as:

$$\begin{aligned} \{\bar{D}_x, \bar{D}_y, \bar{D}_z\} = & \int_{-h/2-h_s}^{-h/2} (D_x, D_y, D_z) \begin{Bmatrix} \cos\left(\frac{\pi z_2}{h_s}\right) \\ \cos\left(\frac{\pi z_2}{h_s}\right) \\ \frac{\pi}{h_s} \sin\left(\frac{\pi z_2}{h_s}\right) \end{Bmatrix} dz + \int_{-h/2}^{h/2} (D_x, D_y, D_z) \begin{Bmatrix} \cos\left(\frac{\pi z_2}{h}\right) \\ \cos\left(\frac{\pi z_2}{h}\right) \\ \frac{\pi}{h} \sin\left(\frac{\pi z_2}{h}\right) \end{Bmatrix} dz \\ & + \int_{h/2}^{h/2+h_s} (D_x, D_y, D_z) \begin{Bmatrix} \cos\left(\frac{\pi z_1}{h_s}\right) \\ \cos\left(\frac{\pi z_1}{h_s}\right) \\ \frac{\pi}{h_s} \sin\left(\frac{\pi z_1}{h_s}\right) \end{Bmatrix} dz \end{aligned} \quad (39a)$$

$$\begin{aligned} \{\bar{B}_x, \bar{B}_y, \bar{B}_z\} = & \int_{-h/2-h_s}^{-h/2} (B_x, B_y, B_z) \begin{Bmatrix} \cos\left(\frac{\pi z_2}{h_s}\right) \\ \cos\left(\frac{\pi z_2}{h_s}\right) \\ \frac{\pi}{h_s} \sin\left(\frac{\pi z_2}{h_s}\right) \end{Bmatrix} dz + \int_{-h/2}^{h/2} (B_x, B_y, B_z) \begin{Bmatrix} \cos\left(\frac{\pi z_2}{h}\right) \\ \cos\left(\frac{\pi z_2}{h}\right) \\ \frac{\pi}{h} \sin\left(\frac{\pi z_2}{h}\right) \end{Bmatrix} dz \\ & + \int_{h/2}^{h/2+h_s} (B_x, B_y, B_z) \begin{Bmatrix} \cos\left(\frac{\pi z_1}{h_s}\right) \\ \cos\left(\frac{\pi z_1}{h_s}\right) \\ \frac{\pi}{h_s} \sin\left(\frac{\pi z_1}{h_s}\right) \end{Bmatrix} dz \end{aligned} \quad (39b)$$

The electric and magnetic fields' virtual contribution can be presented in an easier form:

$$\delta\mathcal{E} = \int_{\Omega} \left(\bar{D}_x \frac{\partial \delta\varphi}{\partial x} + \bar{D}_y \frac{\partial \delta\varphi}{\partial y} - \bar{D}_z \delta\varphi \right) dx dy \quad (40)$$

$$\delta\mathcal{M} = \int_{\Omega} \left(\bar{B}_x \frac{\partial \delta\psi}{\partial x} + \bar{B}_y \frac{\partial \delta\psi}{\partial y} - \bar{B}_z \delta\psi \right) dx dy \quad (41)$$

The kinetic energy variation defined by the m_i mass inertias can be written as:

$$\begin{aligned} \delta\mathcal{K} = & \int_{\Omega} [m_0(\dot{u}_0 \delta \dot{u}_0 + \dot{v}_0 \delta \dot{v}_0 + \dot{w}_0 \delta \dot{w}_0 + \dot{w}_0 \delta \dot{w}_s + \dot{w}_s \delta \dot{w}_0 + \dot{w}_s \delta \dot{w}_s) - m_1 \left(\dot{u}_0 \frac{\partial \delta \dot{w}_0}{\partial x} + \frac{\partial \dot{w}_0}{\partial x} \delta \dot{u}_0 + \dot{v}_0 \frac{\partial \delta \dot{w}_0}{\partial y} \right. \\ & + \frac{\partial \dot{w}_0}{\partial y} \delta \dot{v}_0 \left. \left(\frac{\partial \dot{w}_0}{\partial x} \frac{\partial \delta \dot{w}_0}{\partial x} + \frac{\partial \dot{w}_0}{\partial y} \frac{\partial \delta \dot{w}_0}{\partial y} \right) - m_3 \left(\dot{u}_0 \frac{\partial \delta \dot{w}_0}{\partial x} + \frac{\partial \dot{w}_0}{\partial x} \delta \dot{u}_0 + \dot{v}_0 \frac{\partial \delta \dot{w}_0}{\partial y} + \frac{\partial \dot{w}_0}{\partial y} \delta \dot{v}_0 \right) + m_4 \left(\frac{\partial \dot{w}_0}{\partial x} \frac{\partial \delta \dot{w}_0}{\partial x} \right. \right. \\ & + \frac{\partial \dot{w}_0}{\partial x} \frac{\partial \delta \dot{w}_0}{\partial x} + \frac{\partial \dot{w}_0}{\partial y} \frac{\partial \delta \dot{w}_0}{\partial y} + \frac{\partial \dot{w}_0}{\partial y} \frac{\partial \delta \dot{w}_0}{\partial y} \left. \left. \right) m_5 \left(\frac{\partial \dot{w}_s}{\partial x} \frac{\partial \delta \dot{w}_s}{\partial x} + \frac{\partial \dot{w}_s}{\partial y} \frac{\partial \delta \dot{w}_s}{\partial y} \right) + m_6 (\dot{w}_0 \delta \dot{\phi} + \dot{w}_s \delta \dot{\phi} + \dot{\phi} \delta \dot{w}_0 + \dot{\phi} \delta \dot{w}_s) \right. \\ & \left. + m_7 \dot{\phi} \delta \dot{\phi} \right] dx dy \end{aligned} \quad (42)$$

The differentiation of variables with respect to time is shown here by the dot superscript, and m_i ($i = 0, 1, 2$) mass inertias are defined as:

$$m_i = \int_{-h/2-h_s}^{-h/2} \rho^s z^i dz + \int_{-h/2}^{h/2} p^c(z) z^i dz + \int_{h/2}^{h/2+h_s} \rho^s z^i dz \quad (43a)$$

$$m_{i+3} = \int_{-h/2-h_s}^{-h/2} \rho^s f(z) z^i dz + \int_{-h/2}^{h/2} p^c(z) f(z) z^i dz + \int_{h/2}^{h/2+h_s} \rho^s f(z) z^i dz \quad (43b)$$

$$m_6 = \int_{-h/2-h_s}^{-h/2} \rho^s g(z) dz + \int_{-h/2}^{h/2} p^c(z) g(z) dz + \int_{h/2}^{h/2+h_s} \rho^s g(z) dz \quad (43c)$$

$$m_7 = \int_{-h/2-h_s}^{-h/2} \rho^s g^2(z) dz + \int_{-h/2}^{h/2} p^c(z) g^2(z) dz + \int_{h/2}^{h/2+h_s} \rho^s g^2(z) dz \quad (43d)$$

The virtual work's latest form resulting from in-plane external forces is given by:

$$\delta \mathcal{V} = \int_{\Omega} \left[(p_{x0} + p_{e31} + p_{q31}) \frac{\partial w_0}{\partial x} \frac{\partial \delta w_0}{\partial x} + (p_{y0} + p_{e32} + p_{q32}) \frac{\partial w_0}{\partial x} \frac{\partial \delta w_0}{\partial x} \right] dx dy \quad (44)$$

In the analyses, in-plane mechanical compression forces are assumed to be equal $p_{x0} = N_0$ and $p_{y0} = \gamma N_0$, with $\gamma = p_{x0}/p_{y0}$. The in-plane electric p_{e3i} and magnetic p_{q3i} ($i = 1, 2$) forces are described as:

$$p_{e3i} = - \left[\int_{-h/2-h_s}^{-h/2} e_{3i} \left(\frac{2V_0}{h_s} \right) dz + \int_{-h/2}^{h/2} e_{3i}(z) \left(\frac{2V_0}{h} \right) dz + \int_{h/2}^{h/2+h_s} e_{3i} \frac{2V_0}{h_s} dz \right] \quad (45a)$$

$$p_{q3i} = - \left[\int_{-h/2-h_s}^{-h/2} q_{3i} \left(\frac{2H_0}{h_s} \right) dz + \int_{-h/2}^{h/2} q_{3i}(z) \left(\frac{2H_0}{h} \right) dz + \int_{h/2}^{h/2+h_s} q_{3i} \left(\frac{2H_0}{h_s} \right) dz \right] \quad (45b)$$

For a macro rectangular plate based on the sinusoidal higher-order shear deformation theory, the final seven motion equations (38a–g) can be obtained by substituting the energy variation equations $\delta \mathcal{U}$, $\delta \mathcal{E}$, $\delta \mathcal{M}$, $\delta \mathcal{K}$, and $\delta \mathcal{V}$ from Eqs. (30), (32–34) and (36) into Eq. (22), performing partial integration to obtain the whole differentiations of generalized virtual translations relative to x , y , and t .

$$\delta u_0 : \frac{\partial N_{xx}}{\partial x} + \frac{\partial N_{xy}}{\partial x} = m_0 \ddot{u}_0 - m_1 \frac{\partial \ddot{w}_0}{\partial x} - m_1 \frac{\partial \ddot{w}_s}{\partial x} \quad (46a)$$

$$\delta v_0 : \frac{\partial N_{yy}}{\partial y} + \frac{\partial N_{xy}}{\partial x} = m_0 \ddot{v}_0 - m_1 \frac{\partial \ddot{w}_0}{\partial y} - m_3 \frac{\partial \ddot{w}_s}{\partial y} \quad (46b)$$

$$\begin{aligned} \delta w_0 : & \frac{\partial^2 M_{xx}^{(b)}}{\partial x^2} + 2 \frac{\partial^2 M_{xy}^{(b)}}{dx dy} + \frac{\partial^2 M_{yy}^{(b)}}{dy^2} - (p_{x0} + p_{e31} + p_{q31}) \frac{\partial^2 w_0}{\partial y^2} \\ & = m_0 (\ddot{w}_0 + \ddot{w}_s) + m_1 \left(\frac{\partial \ddot{u}_0}{\partial x} + \frac{\partial \ddot{v}_0}{\partial y} \right) - m_2 \left(\frac{\partial \ddot{w}_0}{\partial x^2} + \frac{\partial \ddot{w}_0}{\partial y^2} \right) - m_4 \left(\frac{\partial^2 \ddot{w}_s}{\partial x^2} + \frac{\partial^2 \ddot{w}_s}{\partial y^2} \right) + m_6 \ddot{\phi} \end{aligned} \quad (46c)$$

$$\begin{aligned} \delta w_s : & \frac{\partial^2 M_{xx}^{(s)}}{\partial x^2} + 2 \frac{\partial^2 M_{xy}^{(s)}}{dx dy} + \frac{\partial^2 M_{yy}^{(s)}}{dy^2} + \frac{\partial S_{xz}}{\partial x} + \frac{\partial S_{yz}}{\partial y} \\ & = m_0 (\ddot{w}_0 + \ddot{w}_s) + m_3 \left(\frac{\partial \ddot{u}_0}{\partial x} + \frac{\partial \ddot{v}_0}{\partial y} \right) - m_4 \left(\frac{\partial^2 \ddot{w}_0}{\partial x^2} + \frac{\partial^2 \ddot{w}_0}{\partial y^2} \right) - m_5 \left(\frac{\partial^2 \ddot{w}_s}{\partial x^2} + \frac{\partial^2 \ddot{w}_s}{\partial y^2} \right) + m_6 \ddot{\phi} \end{aligned} \quad (46d)$$

$$\delta \phi : \frac{\partial S_{xz}}{\partial x} + \frac{\partial S_{yz}}{\partial y} - N_{zz} = m_6 (\ddot{w}_0 + \ddot{w}_s) + m_7 \ddot{\phi} \quad (46e)$$

$$\delta \varphi : \frac{\partial \bar{D}_x}{\partial x} + \frac{\partial \bar{D}_{yz}}{\partial y} + \bar{D}_z = 0 \quad (46f)$$

$$\delta \psi : \frac{\partial \bar{B}_x}{\partial x} + \frac{\partial \bar{B}_{yz}}{\partial y} + \bar{B}_z = 0 \quad (46g)$$

The nanoplate's boundary conditions are defined in the following form:

$$\delta u_0 : 0 = N_{xx} n_x + N_{xy} n_y - m_1 \ddot{w}_0 n_x - m_3 \ddot{w}_s n_x \quad (47a)$$

$$\delta v_0 : 0 = N_{yy} n_y + N_{xy} n_x - m_1 \ddot{w}_0 n_y - m_3 \ddot{w}_s n_y \quad (47b)$$

$$\delta w_0 : 0 = \left[\frac{\partial M_{xx}^{(b)}}{\partial x} + \frac{\partial M_{xy}^{(b)}}{\partial y} - (p_{x0} + p_{e31} + p_{q31}) \frac{\partial w_0}{\partial x} \right] n_x + \left[\frac{\partial M_{yy}^{(b)}}{\partial y} + \frac{\partial M_{xy}^{(b)}}{\partial x} \frac{\partial M_{xy}^{(b)}}{\partial y} - (p_{y0} + p_{e32} + p_{q32}) \frac{\partial w_0}{\partial y} \right] n_y$$

$$+ \left(m_1 \ddot{u}_0 - m_2 \frac{\partial \ddot{w}_0}{\partial x} - m_4 \frac{\partial \ddot{w}_s}{\partial x} \right) n_x + \left(m_1 \ddot{v}_0 - m_2 \frac{\partial \ddot{w}_0}{\partial y} - m_4 \frac{\partial \ddot{w}_s}{\partial y} \right) n_y$$

$$\delta \frac{\partial w_0}{\partial n} : 0 = M_{nn}^{(b)} \quad (47d)$$

$$\delta \frac{\partial w_s}{\partial n} : 0 = M_{nn}^{(s)} \quad (47e)$$

$$\delta \phi : 0 = S_{xz} n_x + S_{yz} n_y \quad (47f)$$

$$\delta \varphi : 0 = \bar{D}_x n_x + \bar{D}_y n_y \quad (47g)$$

$$\delta \psi : 0 = \bar{B}_x n_x + B_y n_y \quad (47h)$$

Here:

$$M_{nn}^{(b)} = M_{xx}^{(b)} n_x^2 + 2M_{xy}^{(b)} n_x n_y + M_{yy}^{(b)} n_y^2, \quad M_{nn}^{(s)} = M_{xx}^{(s)} n_x^2 + 2M_{xy}^{(s)} n_x n_y + M_{yy}^{(s)} n_y^2 \quad (47i)$$

Applying the nonlocal and strain-gradient differential operators $\mathcal{L}(\ast) \equiv 1 - (e_0 a)^2 \nabla^2$ and $\Gamma(\ast) \equiv 1 - (l_m)^2 \nabla^2$ replacing Eqs. (10), (14)–(16), (19), (29), and (31) into Eq. (38), the following equilibrium equations (Eqs. 40a–g) concerning displacements and magneto-electro-elastic coefficients can be obtained for a rectangular nanoplate in the following form:

$$\Gamma \left[A_{11}^{(0)} \frac{\partial^2 u_0}{\partial x^2} - A_{11}^{(1)} \frac{\partial^3 w_0}{\partial x^3} - A_{11}^{-(0)} \frac{\partial^3 w_s}{\partial x^3} + \left(A_{12}^{(0)} + A_{66}^{(0)} \right) \frac{\partial v_0}{\partial x \partial y} - \left(A_{12}^{(1)} + 2A_{66}^{(1)} \right) \frac{\partial^3 w_s}{\partial x \partial y^2} \right. \\ \left. - \left(A_{12}^{-(0)} + 2A_{66}^{-(0)} \right) \frac{\partial^3 w_s}{\partial x \partial y^2} + A_{66}^{(0)} \frac{\partial^2 u_0}{\partial y^2} + \tilde{A}_{13}^{(0)} \frac{\partial \phi}{\partial x} + \bar{B}_{e31}^{(0)} \frac{\partial \varphi}{\partial x} + \bar{B}_{q31}^{(0)} \frac{\partial \psi}{\partial x} \right] = \mathcal{L} \left[m_0 \ddot{u}_0 - m_1 \frac{\partial \ddot{w}_0}{\partial x} - m_3 \frac{\partial \ddot{w}_s}{\partial x} \right] \quad (48a)$$

$$\Gamma \left[A_{22}^{(0)} \frac{\partial^2 v_0}{\partial y^2} - A_{22}^{(1)} \frac{\partial^3 w_0}{\partial y^3} - A_{22}^{-(0)} \frac{\partial^3 w_s}{\partial y^3} + \left(A_{12}^{(0)} + A_{66}^{(0)} \right) \frac{\partial u_0}{\partial x \partial y} - \left(A_{12}^{(1)} + 2A_{66}^{(1)} \right) \frac{\partial^3 w_0}{\partial x^2 \partial y} \right. \\ \left. - \left(A_{12}^{-(0)} + 2A_{66}^{-(0)} \right) \frac{\partial^3 w_s}{\partial x^2 \partial y} + A_{66}^{(0)} \frac{\partial^2 v_0}{\partial x^2} + \tilde{A}_{13}^{(0)} \frac{\partial \phi}{\partial y} + \bar{B}_{e32}^{(0)} \frac{\partial \varphi}{\partial y} + \bar{B}_{e32}^{(0)} \frac{\partial \psi}{\partial y} \right] = \mathcal{L} \left[m_0 \ddot{v}_0 - m_1 \frac{\partial \ddot{w}_0}{\partial y} - m_3 \frac{\partial \ddot{w}_s}{\partial y} \right] \quad (48b)$$

$$\Gamma \left[A_{11}^{(1)} \frac{\partial^3 u_0}{\partial x^3} - A_{22}^{(2)} \frac{\partial^4 w_0}{\partial y^4} - A_{11}^{-(1)} \frac{\partial^4 w_s}{\partial y^4} + \left(A_{12}^{(1)} + 2A_{66}^{(1)} \right) \left(\frac{\partial^3 u_0}{\partial x \partial y^2} + \frac{\partial^3 v_0}{\partial x^2 \partial y} \right) \right. \\ \left. - 2 \left(A_{12}^{(2)} + 2A_{66}^{(2)} \right) \frac{\partial^4 w_0}{\partial x^2 \partial y^2} - 2 \left(A_{12}^{-(1)} + 2A_{66}^{-(1)} \right) \frac{\partial^4 w_s}{\partial x^2 \partial y^4} + A_{22}^{(1)} \frac{\partial^3 v_0}{\partial x^3} - A_{22}^{(2)} \frac{\partial^4 w_0}{\partial y^4} - \bar{A}_{22}^{(1)} \frac{\partial^4 w_s}{\partial y^4} \right. \\ \left. + \tilde{A}_{13}^{(1)} \frac{\partial^2 \phi}{\partial x^2} + A_{23}^{(1)} \frac{\partial^2 \phi}{\partial y^2} + \bar{B}_{e31}^{(1)} \frac{\partial^2 \varphi}{\partial x^2} + \bar{B}_{e32}^{(1)} \frac{\partial^2 \varphi}{\partial y^2} + \bar{B}_{q31}^{(1)} \frac{\partial^2 \psi}{\partial x^2} + \bar{B}_{q32}^{(1)} \frac{\partial^2 \psi}{\partial y^2} \right] \quad (48c)$$

$$= \mathcal{L} \left[(P_{x0} + P_{e31} + P_{q31}) \frac{\partial^2 w_0}{\partial x^2} + (P_{y0} + P_{e32} + P_{q32}) \frac{\partial^2 w_0}{\partial y^2} + m_0 (\ddot{w}_0 + \ddot{w}_s) + m_1 \left(\frac{\partial \ddot{u}_0}{\partial x} + \frac{\partial \ddot{u}_0}{\partial y} \right) \right. \\ \left. - m_2 \left(\frac{\partial^2 \ddot{w}_0}{\partial x^2} + \frac{\partial^2 \ddot{w}_0}{\partial y^2} \right) - m_4 \left(\frac{\partial^2 \ddot{w}_0}{\partial x^2} + \frac{\partial^2 \ddot{w}_0}{\partial y^2} \right) + m_6 \ddot{\phi} \right]$$

$$\begin{aligned}
 & \Gamma \left[\bar{A}_{11}^{(0)} \frac{\partial^3 u_0}{\partial x^3} - \bar{A}_{11}^{(1)} \frac{\partial^4 w_0}{\partial x^4} - \bar{A}_{11}^{(f)} \frac{\partial^4 w_s}{\partial x^4} + \left(\bar{A}_{12}^{(0)} + 2\bar{A}_{66}^{(0)} \right) \left(\frac{\partial^3 u_0}{\partial x \partial y^2} + \frac{\partial^3 v_0}{\partial x^2 \partial y} \right) - 2 \left(\bar{A}_{12}^{(1)} + 2\bar{A}_{66}^{(1)} \right) \frac{\partial^4 w_0}{\partial x^2 \partial y^2} - 2 \left(\bar{A}_{12}^{(f)} + 2\bar{A}_{66}^{(f)} \right) \frac{\partial^4 w_s}{\partial x^2 \partial y^2} \right. \\
 & + \bar{A}_{22}^{(0)} \frac{\partial^3 v_0}{\partial y^3} - \bar{A}_{22}^{(1)} \frac{\partial^4 w_0}{\partial y^4} - \bar{A}_{22}^{(f)} \frac{\partial^4 w_s}{\partial y^4} + \hat{A}_{44}^{(0)} \frac{\partial^2 w_s}{\partial y^2} + \hat{A}_{55}^{(0)} \frac{\partial^2 w_s}{\partial x^2} + \left(\tilde{A}_{13}^{(f)} + \hat{A}_{55}^{(0)} \right) \frac{\partial^2 \phi}{\partial x^2} + \left(\tilde{A}_{23}^{(f)} + \hat{A}_{44}^{(0)} \right) \frac{\partial^2 \phi}{\partial y^2} \\
 & + \left(\bar{B}_{e31}^{(f)} - B_{e15}^{(g)} \right) \frac{\partial^2 \varphi}{\partial x^2} + \ddot{w}_s + m_3 \left(\frac{\partial \ddot{u}_0}{\partial x} + \frac{\partial \dot{v}_0}{\partial y} \right) - m_4 \left(\frac{\partial^2 \ddot{w}_0}{\partial x^2} \left(\bar{B}_{e32}^{(f)} - B_{e24}^{(g)} \right) \frac{\partial^2 \varphi}{\partial y^2} + \left(\bar{B}_{q31}^{(f)} - B_{q15}^{(g)} \right) \frac{\partial^2 \psi}{\partial x^2} + \left(\bar{B}_{q32}^{(f)} - B_{q24}^{(g)} \right) \frac{\partial^2 \psi}{\partial y^2} \right] \\
 & = \mathcal{L} \left[\left(m_0 \left(\ddot{w}_0 + \frac{\partial^2 \ddot{w}_0}{\partial y^2} \right) \right) - m_5 \left(\frac{\partial^2 \ddot{w}_s}{\partial x^2} + \frac{\partial^2 \ddot{w}_s}{\partial y^2} \right) + m_6 \ddot{\phi} \right]
 \end{aligned} \tag{48d}$$

$$\begin{aligned}
 & \Gamma \left[-\tilde{A}_{13}^{(0)} \frac{\partial u_0}{\partial x} + \tilde{A}_{13}^{(1)} \frac{\partial^2 w_0}{\partial x^2} + \left(-\tilde{A}_{13}^{(f)} + \hat{A}_{55}^{(0)} \right) \frac{\partial^2 w_s}{\partial x^2} - \tilde{A}_{23}^{(0)} \frac{\partial v_0}{\partial y} + \tilde{A}_{23}^{(1)} \frac{\partial^2 w_0}{\partial y^2} + \left(-\tilde{A}_{23}^{(f)} + \hat{A}_{44}^{(0)} \right) \frac{\partial^2 w_s}{\partial y^2} \right. \\
 & \left. - \tilde{A}_{33}^{(g)} \phi + \hat{A}_{44}^{(0)} \frac{\partial^2 \phi}{\partial y^2} + \hat{A}_{55}^{(0)} \frac{\partial^2 \phi}{\partial x^2} - B_{e15}^{(g)} \frac{\partial^2 \varphi}{\partial x^2} - B_{e24}^{(g)} \frac{\partial^2 \varphi}{\partial y^2} - B_{q15}^{(g)} \frac{\partial^2 \psi}{\partial x^2} - B_{q24}^{(g)} \frac{\partial^2 \psi}{\partial y^2} - \bar{B}_{e33}^{(g)} \varphi - \bar{B}_{q33}^{(g)} \psi + \bar{B}_{e33}^{(g)} + \bar{B}_{q33}^{(g)} \right] \\
 & = \mathcal{L} [m_6(\ddot{w}_0 + \ddot{w}_s) + m_7 \ddot{\phi}] - \tilde{A}_{13}^{(0)} \frac{\partial u_0}{\partial x} + \tilde{A}_{13}^{(1)} \frac{\partial^2 w_0}{\partial x^2} + \left(\tilde{A}_{13}^{(f)} + \hat{A}_{55}^{(0)} \right) \frac{\partial^2 w_0}{\partial x^2} - \tilde{A}_{23}^{(0)} \frac{\partial v_0}{\partial y} + \tilde{A}_{23}^{(1)} \frac{\partial^2 w_0}{\partial y^2} \\
 & + \left(\tilde{A}_{23}^{(f)} + \hat{A}_{44}^{(0)} \right) \frac{\partial^2 w_s}{\partial y^2} - \left(-\tilde{A}_{23}^{(f)} + \hat{A}_{44}^{(0)} \right) \frac{\partial^2 w_s}{\partial y^2} - \tilde{A}_{23}^{(g)} \phi + \hat{A}_{44}^{(0)} \frac{\partial^2 \phi}{\partial y^2} + \hat{A}_{55}^{(0)} \frac{\partial^2 \phi}{\partial x^2} - B_{e15}^{(g)} \frac{\partial^2 \varphi}{\partial x^2} - B_{e24}^{(g)} \frac{\partial^2 \varphi}{\partial y^2} \\
 & - B_{q15}^{(g)} \frac{\partial^2 \psi}{\partial x^2} - B_{q24}^{(g)} \frac{\partial^2 \psi}{\partial y^2} - \bar{B}_{e33}^{(g)} \varphi - \bar{B}_{q33}^{(g)} \psi + B_{e33}^{(1)} + B_{q33}^{(1)} = \mathcal{L} [m_6(\dot{w}_0 + \dot{w}_s) + m_7 \dot{\phi}]
 \end{aligned} \tag{48e}$$

$$\begin{aligned}
 & \bar{B}_{e31}^{(0)} \frac{\partial u_0}{\partial x} + \bar{B}_{e32}^{(0)} \frac{\partial v_0}{\partial y} - \bar{B}_{e31}^{(1)} \frac{\partial^2 w_0}{\partial x^2} - \bar{B}_{e32}^{(1)} \frac{\partial^2 w_0}{\partial y^2} + \left(B_{e15}^{(g)} - \bar{B}_{e31}^{(f)} \right) \frac{\partial^2 w_2}{\partial y^2} + \bar{B}_{e32}^{(g)} \phi + B_{e15}^{(g)} \frac{\partial^2 \phi}{\partial x^2} + B_{e24}^{(g)} \frac{\partial^2 \phi}{\partial y^2} - P_{e33}^{(s2)} \varphi \\
 & - P_{g33}^{(c2)} \psi + P_{e11}^{(c2)} \frac{\partial^2 \varphi}{\partial x^2} + P_{e22}^{(c2)} \frac{\partial^2 \varphi}{\partial y^2} + P_{g11}^{(c2)} \frac{\partial^2 \psi}{\partial x^2} + P_{g22}^{(c2)} \frac{\partial^2 \psi}{\partial y^2} - P_{g33}^{(s)} - P_{e33}^{(s)} = 0
 \end{aligned} \tag{48f}$$

$$\begin{aligned}
 & \bar{B}_{q31}^{(0)} \frac{\partial u_0}{\partial x} + \bar{B}_{q32}^{(0)} \frac{\partial v_0}{\partial y} - \bar{B}_{q31}^{(1)} \frac{\partial^2 w_0}{\partial x^2} - \bar{B}_{q32}^{(1)} \frac{\partial^2 w_0}{\partial y^2} + \left(B_{q15}^{(g)} - \bar{B}_{q31}^{(f)} \right) \frac{\partial^2 w_s}{\partial x^2} + \left(B_{q24}^{(g)} - \bar{B}_{q32}^{(f)} \right) \frac{\partial^2 w_s}{\partial y^2} + \bar{B}_{q33}^{(g)} \phi \\
 & + B_{q15}^{(g)} \frac{\partial^2 \phi}{\partial x^2} + B_{q24}^{(g)} \frac{\partial^2 \phi}{\partial y^2} - P_{g33}^{(s2)} \varphi - P_{\mu33}^{(c2)} \psi + P_{g11}^{(c2)} \frac{\partial^2 \varphi}{\partial x^2} + P_{g22}^{(c2)} \frac{\partial^2 \varphi}{\partial y^2} + P_{\mu11}^{(c2)} \frac{\partial^2 \psi}{\partial x^2} + P_{\mu22}^{(c2)} \frac{\partial^2 \psi}{\partial y^2} - P_{g33}^{(s)} - P_{\mu33}^{(s)} = 0
 \end{aligned} \tag{48g}$$

The definitions of the resulting magneto-electro-elastic coefficients are provided in Appendix A1–A3.

$$\begin{pmatrix} u_0 \\ v_0 \\ w_0 \\ w_s \\ \phi \\ \varphi \\ \psi \end{pmatrix} = \sum_{m=1}^{\infty} \sum_{n=1}^{\infty} \begin{pmatrix} \bar{u} \cos(\alpha x) \sin(\beta y) e^{i\omega t} \\ \bar{v} \sin(\alpha x) \cos(\beta y) e^{i\omega t} \\ \bar{w}_0 \sin(\alpha x) \sin(\beta y) e^{i\omega t} \\ \bar{w}_s \sin(\alpha x) \sin(\beta y) e^{i\omega t} \\ \bar{\phi} \sin(\alpha x) \sin(\beta y) e^{i\omega t} \\ \bar{\varphi} \sin(\alpha x) \sin(\beta y) e^{i\omega t} \\ \bar{\psi} \sin(\alpha x) \sin(\beta y) e^{i\omega t} \end{pmatrix}, \quad \alpha = \frac{m\pi}{L_x}, \quad \beta = \frac{n\pi}{L_y} \tag{49}$$

The remaining seven variables, \bar{u} , \bar{v} , \bar{w}_0 , \bar{w}_s , $\bar{\phi}$, $\bar{\varphi}$, and $\bar{\psi}$, respectively, stand in for the greatest displacement, electric, and magnetic potential values. Here, it stands for the natural frequency. For ease of use, these seven variables can be represented as vectors.

2.7. Solution method

The precise analytical solutions of a simply supported (SS) three-layered rectangular nanoplate are obtained in the research using Navier’s solution approach. Due to this, the double trigonometric series expansion is used to solve for the seven unknowns as follows:

$$\{\Delta\} = [\bar{u} \quad \bar{v} \quad \bar{w}_0 \quad \bar{w}_s \quad \bar{\phi} \quad \bar{\varphi} \quad \bar{\psi}]^T \quad (50)$$

The governing equations system is finally arranged as in the below form by using the stiffness $[K]$ and inertia $[M]$ matrices, and load vector $\{F\}$:

$$\{[K] - \omega_{mn}^2[M]\}\{\Delta\} = \{F\} \quad (51)$$

In addition, the load vector, neglectable in the free vibration and buckling analysis, is as follows:

$$\{F\} = \left[\begin{array}{ccccccc} 0 & 0 & 0 & 0 & -\left(B_{e33}^{(g)} + B_{q33}^{(g)}\right) & -\left(P_{g33}^{(g)} + P_{e33}^{(g)}\right) & -\left(P_{g33}^{(g)} + P_{e33}^{(g)}\right) \end{array} \right] \quad (52)$$

In the case of free vibration analysis, the nanoplate's governing equation system under in-plane static forces is defined as follows:

$$\{[K] - \omega_{mn}^2[M]\}\{\Delta\} = \{0\} \quad (53)$$

Also, just for nanoplate's buckling analysis, the system of governing equations is:

$$[K]\{\Delta\} = \{0\} \quad (54)$$

The elements of symmetric ($K_{ij} = K_{ji}$) stiffness $[K]$ and symmetric ($M_{ij} = M_{ji}$) inertia matrixes are given in Appendix A4–A5.

2.8. Validation

The following non-dimensional frequency parameter (Eq. 39) is defined in the same manner as the research of [80,81] in order to verify the current investigation. Here, the bottom material's mass density and elasticity modulus are $\rho_b=5300 \text{ kg/m}^3$ and $C_{b11}=166 \text{ GPa}$, respectively (BaTiO_3). The plate has a rectangular form, $a=2 \text{ m}$, $b=1 \text{ m}$, ratio $h/a=0.2$, and is made of $\text{BaTiO}_3/\text{CoFe}_2\text{O}_4$ with $p=1$.

$$\bar{\omega} = \omega_{(m,n)} \left(\frac{a^2}{h} \right) \sqrt{\frac{\rho_b}{C_{b11}}} \quad (55)$$

Table 4 compares the dimensionless frequencies of the current investigation with those of the literature studies. Table 4 shows that, except for the first and second modes, the findings of the recent research and Ref. [80] are comparable.

The tables below compare the three nonlocal plate hypotheses with the computed maximum deflection and natural frequencies [82]. The dimensionless maximum deflections computed by three nonlocal plate theories are compared with the current investigation results in Tables 3 and 4 based on the various nonlocal parameter and thickness values for square and rectangular plates under uniformly distributed and point loads. These assessments

indicated that the findings from the present research were comparable to those from studies using first- and third-order theories. Additionally, the nonlocal theory provided superior predictions for more significant displacements, and for all nonlocal effect values, findings from the first and third-order theories were roughly equivalent. The computed natural frequencies are contrasted in Tables 5 and 6 with the third-order nonlocal plate theories taking into account various nonlocal parameters and aspect ratio values. The following equations were used to compare the maximum non-dimensional deflection and natural frequencies:

$$\bar{w} = -w \left(\frac{Eh^2}{q_0 a^4} \right) 10^2 \quad \bar{w} = -w \left(\frac{Eh^2}{Q_0 a^4} \right) 10^2 \quad \bar{\omega} = \omega h \sqrt{\frac{\rho}{G}} \quad (56)$$

where Q_0 and q_0 denote the size of the point and uniform loads, the parameters a , E , ν , and represent the plate's length, elastic modulus, Poisson's ratio, and density.

Table 5 compares the computed deflections of a supported isotropic plate with $a=10$, $\nu=0.3$ for the Poisson ratio, and $E=300 \times 10^6$ for the elastic modulus caused by applying a single load, $q_0=1\text{N}$. Table 6 compares the

Table 4. Comparison of the dimensionless frequencies $\bar{\omega}$ of an FG simply supported rectangular plate consisting of $\text{BaTiO}_3/\text{CoFe}_2\text{O}_4$.

Mode	Ref. [81]	Ref. [80]	Present study
(1,1)	9.525	10.0244	16.6437
(2,2)	28.762	32.5716	51.9655
(3,3)	50.966	66.2842	77.9483
(4,4)	131.186	104.0065	103.9311
(5,5)	139.106	129.6477	129.9139

Table 3. Temperature dependent coefficients for the properties of Si_3N_4 , SUS304 [65, 83].

Material	Property	P_{-1}	P_0	P_1	P_2	P_3	$P(T=300\text{K})$
Si_3N_4	E (Pa)	0	$348.43e+9$	$-3.070e-4$	$2.160e-7$	$-8.946e-11$	$3.2227e+11$
	ν	0	0.24	0	0	0	0.24
	α (1 K^{-1})	0	$5.8723e-6$	$9.095e-4$	0	0	$7.4746e-06$
	κ (W/mK)	-1123.6	-14.087	$-6.227e-3$	0	0	–
	ρ (kg/m^3)	0	2370	0	0	0	2370
SUS304	E (Pa)	0	$201.04e+9$	$3.079e-4$	$-6.534e-7$	0	$207.7877 \text{ e}+9$
	ν	0	0.3262	$-2.002e-4$	$3.97e-7$	0	0.3177
	α (1 K^{-1})	0	$12.33e-6$	$8.086e-4$	0	0	$15.32e-6$
	κ (W/mK)	0	15.397	$-1.264e-3$	$2.09e-6$	$-7.223e-10$	–
	ρ (kg/m^3)	0	8166	0	0	0	8166

Table 5. Comparison of non-dimensional maximum center deflection \bar{w} in simply supported plate under uniform load q_0 ($q_0=1$, $a=10$, $\nu=0.3$ and $E=300 \times 10^6$ Pa).

a/b	a/h	μ	Classical	First-order [82]	Third-order [82]	Present (high-order)
1	10	0	4.0083	4.1853	4.1853	4.1854
		0.5	4.3702	4.5608	4.5607	4.5607
		1	4.7322	4.9363	4.9362	4.9362
	1.5	0	5.0942	5.3118	5.3116	5.3116
		0.5	5.4561	5.6873	5.6871	5.6879
		2.5	5.8181	6.0628	6.0625	6.0630
	3	0	6.18	6.4383	6.438	6.4387
		0.5	4.0083	4.0154	4.0154	4.0153
		1	4.3702	4.3779	4.3779	4.3781
	50	0	4.3702	4.7404	4.7404	4.7410
		0.5	4.7322	5.1029	5.1029	5.1033
		1	5.0942	5.4654	5.4654	5.4650
	2.5	0	5.8181	5.8279	5.8279	5.8280
		0.5	6.18	6.1904	6.1904	6.1901
		1	4.0083	4.01	4.01	4.0122
100	0	4.3702	4.3721	4.3721	4.3725	
	0.5	4.7322	4.7342	4.7342	4.7340	
	1	5.0942	5.0963	5.0963	5.0960	
2	10	0	0.6483	0.717	0.7169	0.7180
		0.5	0.7946	0.8768	0.8767	0.8760
		1	0.9408	1.0366	1.0364	1.0361
1.5	0	1.087	1.1965	1.1961	1.1970	
	0.5	1.2332	1.3563	1.3558	1.3560	
	2.5	1.3794	1.5161	1.5155	1.5165	
3	0	1.5256	1.6759	1.6752	1.6766	
	0	0.6483	0.6511	0.6511	0.6508	
	0.5	0.7946	0.7978	0.7978	0.7985	
50	1	0.9408	0.9446	0.9446	0.9440	
	1.5	1.087	1.0914	1.0914	1.0917	
	2	1.2332	1.2381	1.2381	1.2384	
2.5	0	1.3794	1.3849	1.3849	1.3846	
	0.5	1.5256	1.5316	1.5316	1.5314	
	1	0.6483	0.649	0.649	0.6485	
100	0.5	0.7946	0.7954	0.7954	0.7950	
	1	0.9408	0.9417	0.9417	0.9415	
	1.5	1.087	1.0881	1.0881	1.0883	
2	0	1.2332	1.2344	1.2344	1.2340	
	0.5	1.3794	1.3808	1.3808	1.3805	
	3	1.5256	1.5271	1.5271	1.5265	

Table 6. Comparison of the supported plate's non-dimensional maximum center deflection w under the central Q_0 point load ($Q_0=1$, $a=10$, $E=30 \times 10^6$ Pa, $\nu=0.3$, 100 term series).

a/b	a/h	μ	Classical	First-order [82]	Third-order [82]	Present (high-order)
1	10	0	0.4609	0.5147	0.5137	0.5180
		0.5	0.5752	0.821	0.8072	0.8222
		1	0.6894	1.1274	1.1008	1.1270
	1.5	0	0.8037	1.4337	1.3944	1.4340
		0.5	0.918	1.7401	1.688	1.7505
		2.5	1.0322	2.0465	1.9816	2.0484
	3	0	1.1465	2.3528	2.2751	2.3553
		0	0.4609	0.463	0.463	0.4640
		0.5	0.5752	0.585	0.585	0.5865
	50	1	0.6894	0.707	0.7069	0.7092
		1.5	0.8037	0.8289	0.8288	0.8285
		2	0.918	0.9509	0.9508	0.9510
	2.5	0	1.0322	1.0728	1.0727	1.0725
		0.5	1.1465	1.1948	1.1947	1.1950
		1	0.4609	0.4614	0.4614	0.4611
100	0.5	0.5752	0.5776	0.5776	0.5778	
	1	0.6894	0.6938	0.6938	0.6935	
	1.5	0.8037	0.81	0.81	0.8150	
2	10	0	0.918	0.9262	0.9262	0.9260
		0.5	1.0322	1.0424	1.0424	1.0420
		3	1.1465	1.1586	1.1586	1.1589
50	0	0.1685	0.2183	0.2165	0.2188	
	0.5	0.2753	0.7092	0.6528	0.7090	
	1	0.3821	1.2002	1.089	1.2008	
1.5	0	0.4889	1.6911	1.5253	1.6907	
	0.5	0.5957	2.182	1.9616	2.1835	
	2.5	0.7025	2.6729	2.3979	2.6724	
3	0	0.8093	3.1638	2.8341	3.1630	
	0	0.1685	0.1705	0.1705	0.1700	
	0.5	0.2753	0.2927	0.2926	0.2930	
50	1	0.3821	0.4148	0.4146	0.4152	
	1.5	0.4889	0.537	0.5367	0.5394	
	2	0.5957	0.6592	0.6587	0.6590	
2.5	0	0.7025	0.7813	0.7808	0.7816	
	0.5	0.8093	0.9035	0.9029	0.9030	
	1	0.1685	0.169	0.169	0.1685	
100	0.5	0.2753	0.2796	0.2796	0.2791	
	1	0.3821	0.3903	0.3903	0.3901	
	1.5	0.4889	0.5009	0.5009	0.5010	
2	0	0.5957	0.6116	0.6115	0.6111	
	0.5	0.7025	0.7222	0.7222	0.7225	
	3	0.8093	0.8328	0.8328	0.8330	

computed deflections of a supported, isotropic plate with $a=10$, $\nu=0.3$ for the Poisson ratio, and $E=300 \times 106$ for the elastic modulus caused by the application of a uniform load $Q_0=1$ N/m up to 100 term series. In Table 7, investigations employing various theories from the literature are compared with the computed non-dimensional first mode frequency $\bar{\omega}_{11}$ of a supported isotropic plate with $a=10$, Poisson ratio $\nu=0.3$, and modulus of elasticity $E=300 \times 106$. In Table 8, investigations employing various theories from the literature are compared with the computed non-dimensional higher-order frequencies $\bar{\omega}$ of a simply supported isotropic plate with $a=10$, $a/b=1$, $a/h=100$, Poisson ratio $\nu=0.3$, and modulus of elasticity $E=300 \times 106$.

3. Numerical analysis

In this section, temperature-dependent effective material properties (effective elasticity module E_{ef} , effective Poisson ratio ν_{ef} , effective thermal expansion coefficient κ_{ef} , and effective thermal conductivity coefficients ψ_{ef}) of the whole plate (core and face plates) have been determined with the

Table 7. Comparison of non-dimensional first mode frequency $\bar{\omega}_{11}$ of simply supported plate ($a=10$, $E=30 \times 10^6$ Pa, $\nu=0.3$).

a/b	a/h	μ	Classical	First-order [82]	Third-order [82]	Present (high-order)
1	10	0	0.0963	0.093	0.0935	0.0935
		1	0.088	0.085	0.0854	0.0851
		2	0.0816	0.0788	0.0791	0.0781
		3	0.0763	0.0737	0.0741	0.0732
		4	0.072	0.0696	0.0699	0.0699
	20	0	0.0683	0.066	0.0663	0.0665
		0	0.0241	0.0239	0.0239	0.0240
		1	0.022	0.0218	0.0218	0.0215
		2	0.0204	0.0202	0.0202	0.0207
		3	0.0191	0.0189	0.0189	0.0190
	4	0	0.018	0.0178	0.0179	0.0175
		0	0.0171	0.0169	0.017	0.0161
		0	0.0602	0.0589	0.0591	0.0590
		1	0.0568	0.0556	0.0557	0.0551
		2	0.0539	0.0527	0.0529	0.0524
3	0	0.0514	0.0503	0.0505	0.0501	
	0	0.0493	0.0482	0.0483	0.0488	
	0	0.0473	0.0463	0.0464	0.0464	
	0	0.015	0.015	0.015	0.0152	
	1	0.0142	0.0141	0.0141	0.0140	
2	0	0.0135	0.0134	0.0134	0.0135	
	0	0.0129	0.0128	0.0128	0.0130	
	0	0.0123	0.0123	0.0123	0.0120	
	0	0.0118	0.0118	0.0118	0.0116	

different material gradation index p , material porosity ratio α , strain gradient effect l_m , and nonlocal parameter e_0a considering different material porosity models (uniform porosity Model 1, symmetric porosity Model 2, asymmetric ascending downward porosity Model 3, asymmetric ascending up porosity Model 4). The mechanical and physical characteristics of BaTiO₃ and CoFe₂O₄ are shown in Table 2. The eigenvalue equation is solved to get the vibration

Table 8. Comparison of non-dimensional higher order frequencies ($\bar{\omega}$) of simply supported plate ($a = 10$, $a/b = 1$, $a/h = 100$, $E = 30 \times 10^9$ Pa, $\nu = 0.3$).

Frequencies μ	Classical	First-order [82]	Third-order [82]	Present (high-order)
ω_{11}	0	0.0963	0.093	0.0935
	1	0.088	0.085	0.0854
	2	0.0816	0.0788	0.0791
	3	0.0763	0.0737	0.0741
	4	0.072	0.0696	0.0699
ω_{22}	0	0.3853	0.3414	0.3458
	1	0.288	0.2552	0.2585
	2	0.2399	0.2126	0.2153
	3	0.2099	0.186	0.1884
	4	0.1889	0.1674	0.1696
ω_{33}	0	0.8669	0.6889	0.702
	1	0.5202	0.4134	0.4213
	2	0.4063	0.3228	0.329
	3	0.3446	0.2738	0.279
	4	0.3045	0.242	0.2466
5	0.2757	0.2191	0.2233	

frequencies (Eq. 51). The material of the core plate consists of ceramic one Silicon nitrite (Si₃Ni₄) and metallic one SUS304. On the other hand, face plates' material content of BaTiO₃ and CoFe₂O₄.

3.1. The effective properties of the FGM's plate depending on the temperature rise

This section investigates the effective material properties of the whole plate, considering nonlinear temperature rise from 300 to 800 K for the different material gradation indexes p , material porosity ratios α , and different material porosity models. The uniform porosity model (Model 1), given in Figure 2, has been implemented for the numerical analysis. On the other hand, for the numerical simulation analysis, face plate material compounds are chosen as $Br = 0.5$ and $Co = 0.5$ (50% BaTiO₃ and 50% CoFe₂O₄). Depending on the material composition (p) with a nonlinear temperature rise between 300 and 800 K with the increment step 1 K, Figure 3 shows the alterations in the FGM plate's actual material properties. Each composition's effective elasticity modulus E_{ef} demonstrates a diminishing behavior as the temperature rises because of the increased temperature rise ΔT , the material is getting softer, as shown in Figure 3a with the porosity ratio of the core plate $\alpha = 0$, strain gradient effect $l_m = 0$, and nonlocal parameter $e_0a = 0$.

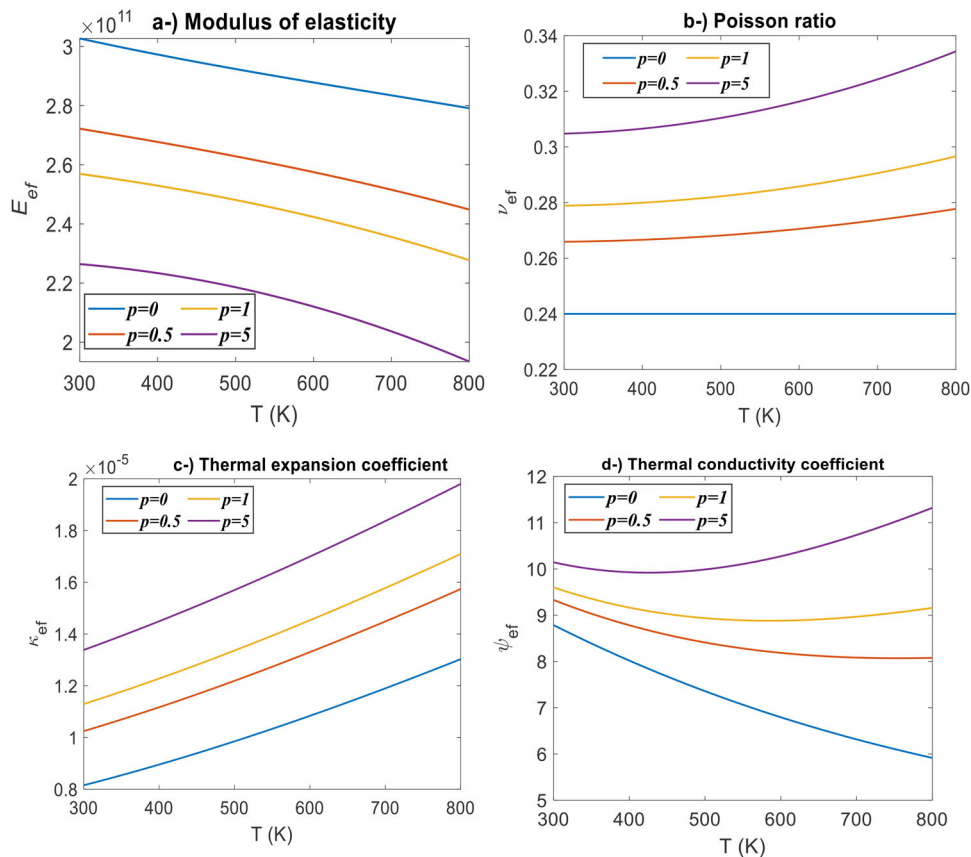


Figure 3. Comparison of the effective material properties of the whole plate (face plate and core plate) depending on the four different material gradation index of the core plate ($p = 0, 0.5, 1$, and 5) and nonlinear temperature rise ΔT with the range of 300–800 K; for the porosity index $\alpha = 0$; aspect ratio $a/H = 10$; face plate material Barium 50% and Cobalt 50%; nonlocal parameter $e_0a = 0$; material size parameter $l_m = 0$; external electric potential $V_0 = 0$; external magnetic potential $H_0 = 0$; material porosity model Model 1; (a) effective elasticity modulus E_{ef} , (b) effective Poisson ratio ν_{ef} , (c) effective thermal expansion coefficient κ_{ef} , (d) effective thermal conductivity ψ_{ef} .

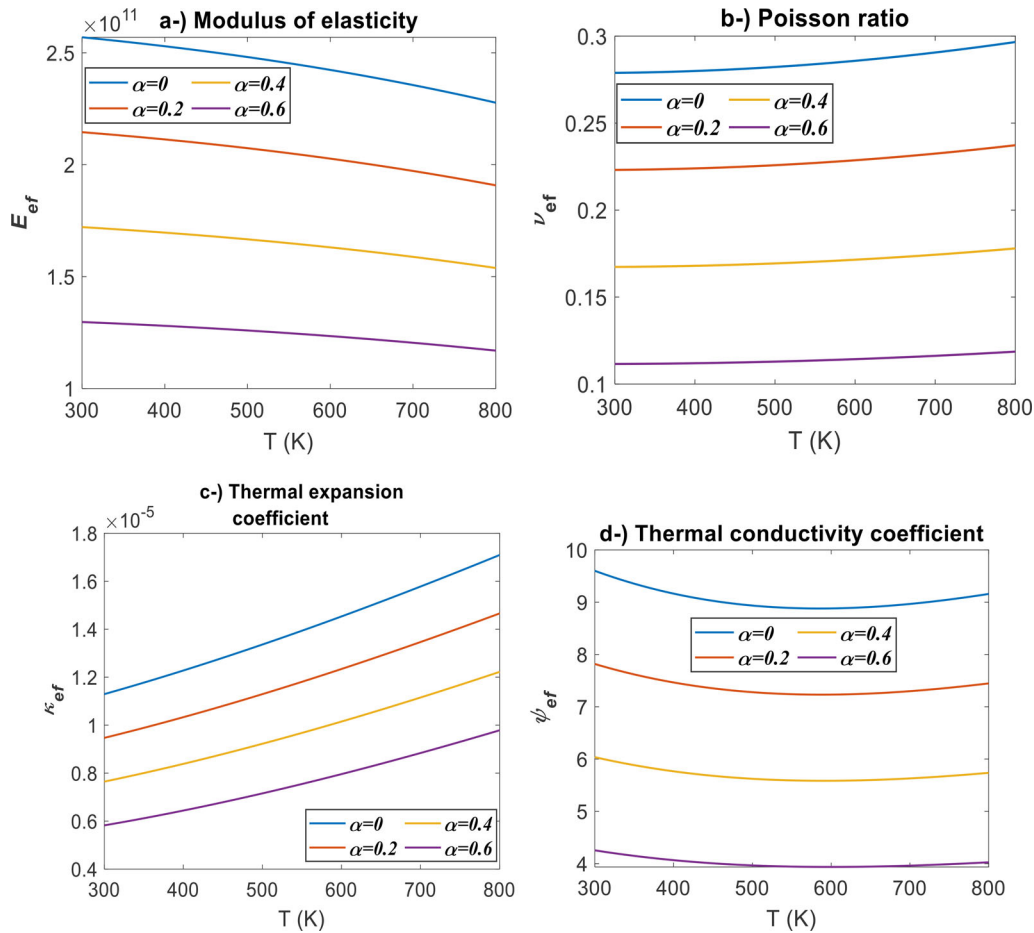


Figure 4. Comparison of the effective material properties of the whole plate (face plate and core plate) depending on the four different material porosity ratios of the core plate ($\alpha = 0, 0.2, 0.4$, and 0.6) and nonlinear temperature rise ΔT with the range of 300–800 K; for material gradation index of the core plate $p = 1$; aspect ratio $a/H = 10$; face plate material Barium 50% and Cobalt %50; nonlocal parameter $e_0 a = 0$; material size parameter $l_m = 0$; external electric potential $V_0 = 0$; external magnetic potential $H_0 = 0$; material porosity model Model 1; (a) effective elasticity modulus E_{ef} , (b) effective Poisson ratio ν_{ef} , (c) effective thermal expansion coefficient κ_{ef} , (d) effective thermal conductivity ψ_{ef} .

Moreover, as shown in Figure 3a, the effective elasticity modulus E_{ef} decreases gradually as the increased material gradation indexes p because the elasticity module of the ceramic (Si_3N_4) is bigger than the metallic one (SUS304) (remember $p = 0$ for the ceramic all of the core plate, $p = \infty$ for metallic all of the core plate). On the other hand, as shown in Figure 3a, decreases in the effective elasticity modulus E_{ef} of the plate are nearly linear for the ceramic-weighted material and nonlinear for the metallic material. Figure 3b shows the effective Poisson ratio ν_{ef} of the whole plate according to nonlinear temperature rise for the different material gradation indexes p . As shown in the figure, the Poisson ratio of the plate is bigger for the metallic material (big p values) than for the weighted ceramic material. Furthermore, the nonlinearity of the curve is increased by increasing the material gradation index p (metal content). For the material gradation index $p = 0$ (ceramic one), the change of the Poisson ratio according to temperature rise is minimal and nearly linear. But, for the metallic content one, the change of the Poisson ratio according to temperature rise is maximum, and the curve is nonlinear. Moreover, the effective thermal expansion coefficient κ_{ef} increases linearly with temperature, although the metallic-rich compositions' increment ratio is more notable than the ceramic one

(Figure 3c). For the same temperature, the thermal expansion coefficient of the metallic plate is obtained higher than the ceramic material plate. For example, the thermal expansion coefficient is obtained for the nonlinear temperature rise $\Delta T = 500$ K $9.85e - 6$, $1.22e - 5$, $1.33e - 5$, and $1.56e - 5$ with $p = 0, 0.5, 1$, and 5 , respectively. As shown in Figure 3d, the thermal conductivity coefficient ψ_{ef} increase as the increases nonlinear temperature rise for the metal-rich or entirely metallic compositions. On the other hand, for the ceramic-rich composition, as the increase temperature rise, the thermal conductivity parameters decrease, as shown in the figure.

According to various porosity ratios parameters, α and nonlinear temperature changes from 300 K to 800 K with increment 1 K for a constant material gradation index $p = 1$, the material porosity model 1, strain gradient effect $l_m = 0$, and nonlocal parameter $e_0 a = 0$ and material porosity model Model 1 given in Figure 2. Figure 4 depicts the effective material property fluctuations (E_{ef} , ν_{ef} , κ_{ef} , and ψ_{ef}) of the FGM nanoplate. As shown in the figure generally, it is clearly seen that the effective material properties value decreases as the increase porosity ratio α increases. For example, the effective elasticity modulus E_{ef} of the FGM nanoplate has been determined as $2.48e11$, $2.07e11$, $1.66e11$,

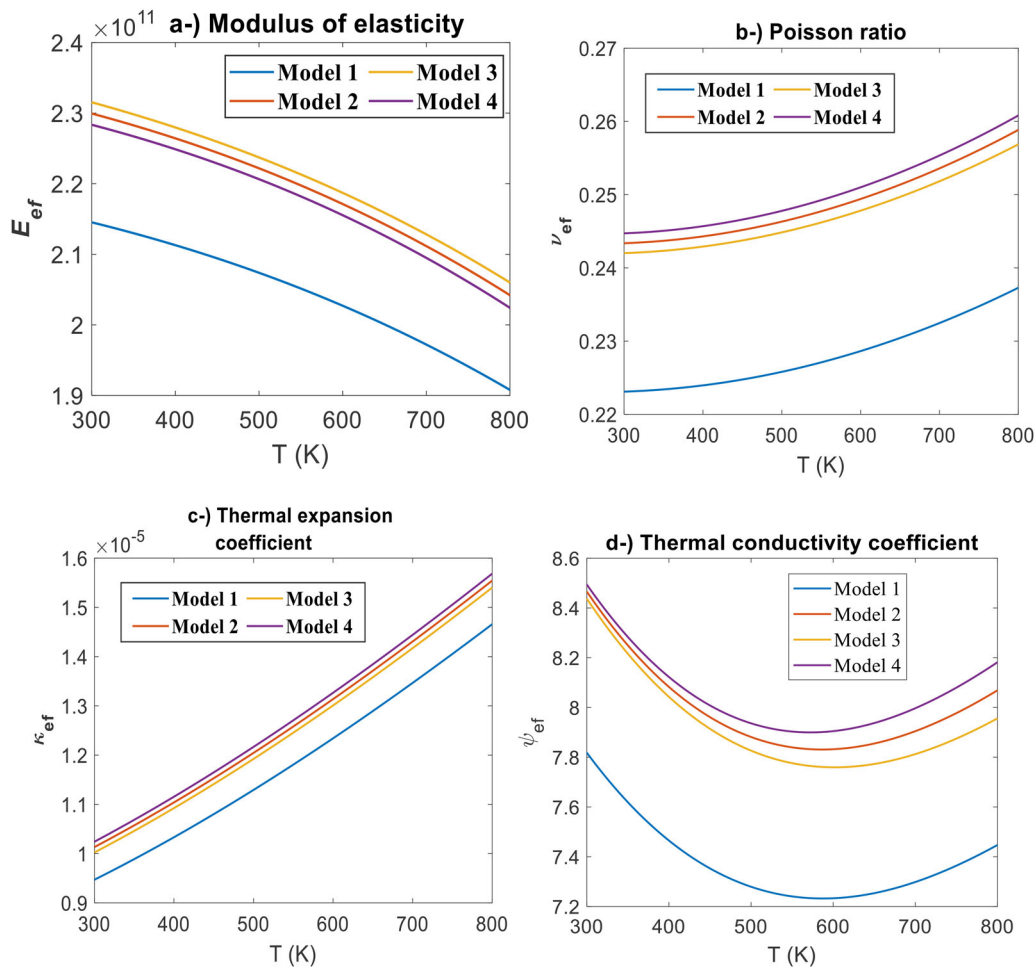


Figure 5. Comparison of the effective material properties of the whole plate (face plate and core plate) depending on the four different material porosity models of the core plate (Models 1, 2, 3, and 4) and nonlinear temperature rise ΔT with the range of 300–800 K; for material gradation index of the core plate $p=1$, the parameters porosity ratio $\alpha=0.2$; aspect ratio $a/H=10$; face plate material Barium 50% and Cobalt %50; nonlocal parameter $e_0a=0$; material size parameter $l_m=0$; external electric potential $V_0=0$; external magnetic potential $H_0=0$; (a) effective elasticity modulus E_{ef} , (b) effective Poisson ratio ν_{ef} , (c) effective thermal expansion coefficient κ_{ef} , (d) effective thermal conductivity ψ_{ef} .

and 1.25e11 Pa, respectively, for the temperature rise $\Delta T=500$ K. On the other hand, as shown in the figures, as the increase in nonlinear temperature rise ΔT effective elasticity modulus E_{ef} of the FGM plates decreases, and the effective Poisson ratio ν_{ef} and effective thermal expansion coefficients κ_{ef} increase. However, as shown in Figure 4d, the coefficient of thermal conductivity decreased up to around 600 K and then increased nonlinearly.

The effective material property changes of the FGM nanoplate are shown in Figure 5 when different models of porosity distribution and nonlinear temperature increases between 300 and 800 K are taken into account with the parameters porosity ratio $\alpha=0.2$ and material gradation index $p=1$. As shown in the figures, the increase in the temperature of the FGM plate decreased effective the modulus of elasticity E_{ef} in all porosity models (Figure 5a) linearly while increasing Poisson's ratio ν_{ef} and coefficient of thermal expansion κ_{ef} nonlinearly (Figure 5b, c). The biggest and smallest effective elasticity module value have been obtained with Model 3 and Model 1, respectively, while these values are defined with Model 4 and Model 1 for the effective Poisson ratio. On the other hand, as shown in Figure 5c, the biggest and smallest effective thermal

expansion coefficient κ_{ef} has been obtained with the porosity models Model 4 and 1, respectively.

However, as shown in Figure 5d, the coefficient of thermal conductivity ψ_{ef} of the FGM plate decreased up to around 600 K and then improved nonlinearly up to 800 K. Moreover, the biggest effective thermal conductivity value for any temperature given in the figure is obtained for the porosity model 1.

3.2. Frequency analysis of the FGM nanoplate

For a constant porosity index of $\alpha=0.4$, Figure 6 shows the first three dimensionless frequency variations that rely on the porosity models and material composition with the nonlocal parameter $e_0a=0$, material scale factor $l_m=0$. As shown in the figure, as the increased material gradation index p , the first three dimensionless frequencies of the FGM plate decrease gradually. Moreover, the biggest first dimensionless frequencies value has been obtained with the porosity model 1. For the second and third dimensionless frequency, the biggest frequency parameter values have been obtained with Model 1 for the low material gradation index [0,1] and Model 3 for the higher material gradation index

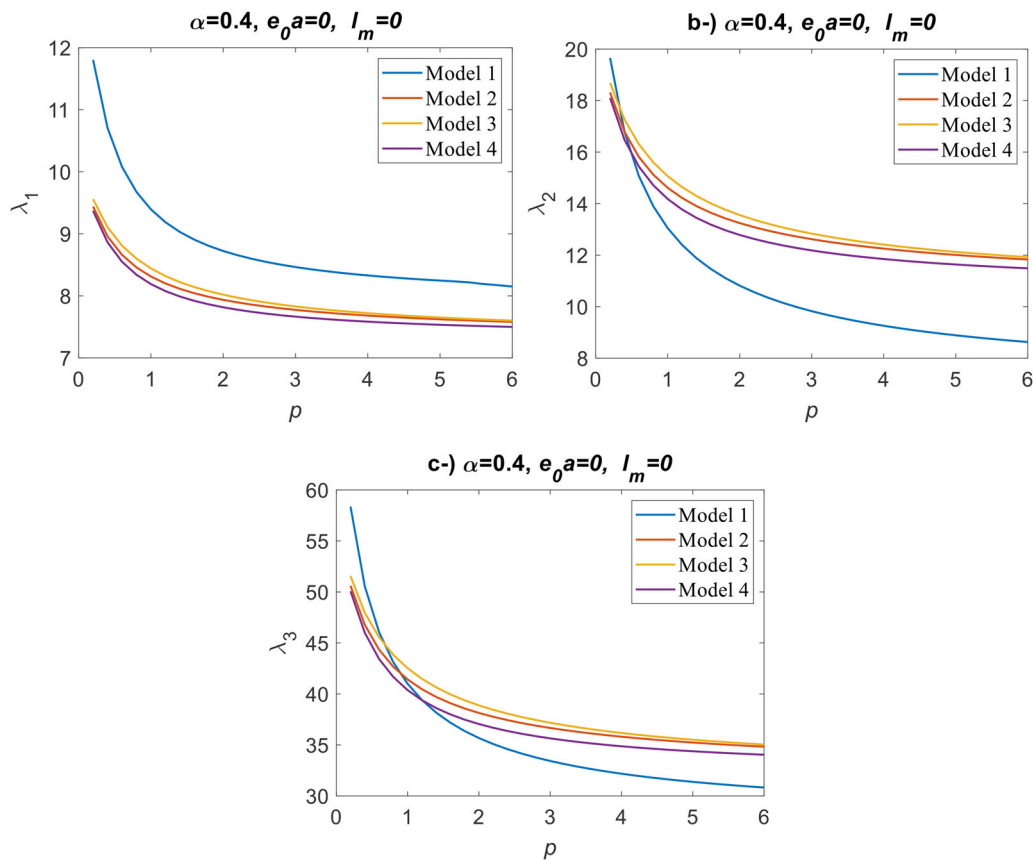


Figure 6. Comparison of the first three dimensionless frequencies λ_1 , λ_2 , and λ_3 depending on the material gradation index of core plate $p=0-6$ and different models of porosity distributions of the core plate; for the porosity index $\alpha=0.4$; aspect ratio $a/H=10$; face plate material Barium 50% and Cobalt %50; nonlocal parameter $e_0a=0$; material size parameter $I_m=0$; temperature rise $\Delta T=0$; external electric potential $V_0=0$; external magnetic potential $H_0=0$; (a) the fundamental frequency parameter λ_1 , (b) the second frequency parameter λ_2 , (c) the third frequency λ_3 .

[1,6]. A quick frequency reduction is seen for the material gradation index p at the values of 0 and 1. After p is bigger than 1, the decline becomes more gradual until it reaches limitations for higher p values, at which point the material composition is more likely to be pure metal. It has been shown that the uniform porosity model (Model 1) exhibits higher variances than the others, and its variation curve type takes on an entirely new shape, whereas the other curves indicate largely comparable patterns. The porosity of Model 1 shows the greatest degree of reduction for the second and third frequency values. Model 1, 2, 3, and 4 porosity models decreased the dimensionless frequencies from 11.8, 9.43, 9.55, and 9.37 to 8.15, 7.57, 7.6, and 7.49, respectively, when the material gradation index p increased from 0.2 to 6. As a result, the reductions in 1 dimensionless frequency for Models 1, 2, 3, and 4 are computed to be 30.9, 19.7, 20.4, and 20%. These values have been obtained for the second and third frequencies and are presented in Table 9.

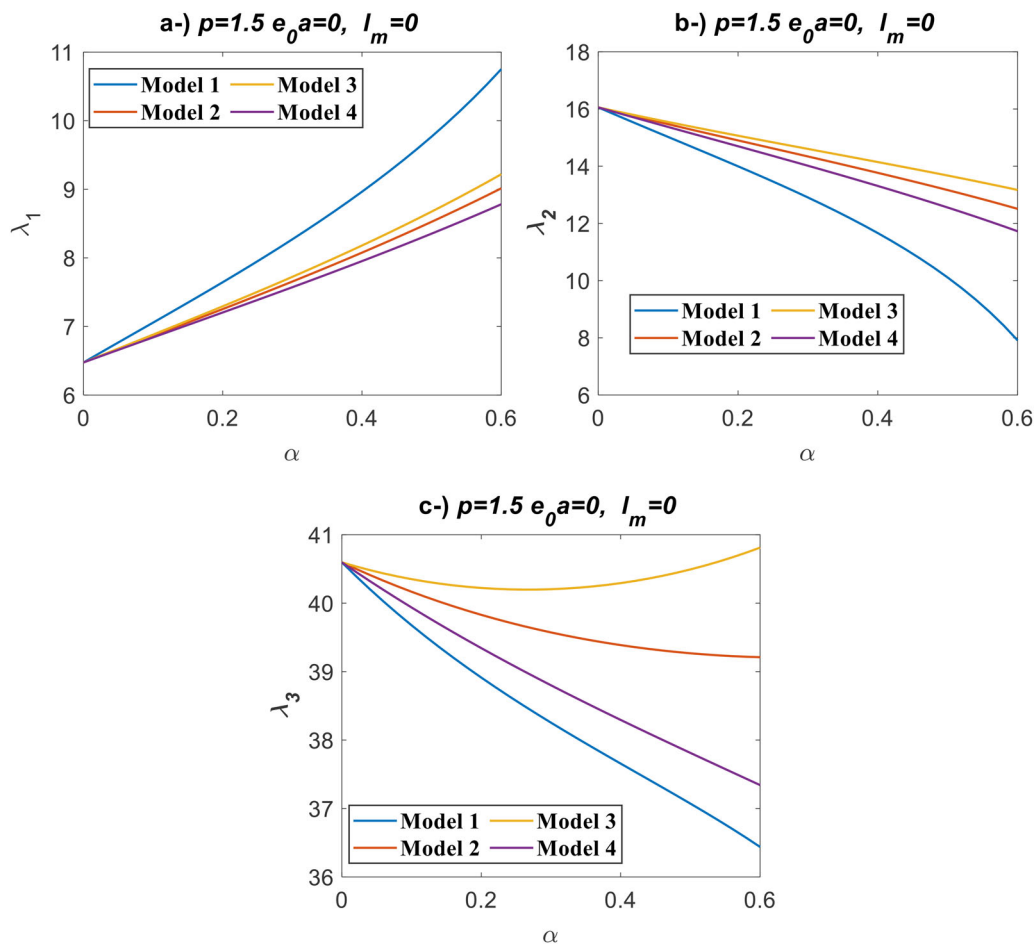
The core plate's material consists of metal at the bottom surface and ceramic (S3N4) at the top surface of the core plate. Between the bottom and top surfaces, the material composition of the core plate is formed of metal and ceramic constituents depending on the material gradation index p . When $p=0$, the whole material of the core plate is ceramic, and at $p=\infty$ it is from metal (SUS304). At $p=1$, the total material composition is 50% metal and 50% ceramic. But the composition is changed through the thickness when

$p=5$ the total material composition of the core plate is made of 83.3% metal and 16.7% ceramic. Due to this fact that when $p=5$, the amount of the metal reaches 83.3%, and the variation curves of the frequencies tend to limit because of the trend of homogenous material from metal. As the material gradation index p -value increases, the dimensionless frequency parameter generally decreases and this is due to the increase in the amount of metal in the core plate. Metal, SUS304's modulus of elasticity at 300 K is 207.78 GPa of ceramic, and SiN4's is 322.27 GPa. Therefore, since the modulus of elasticity of the metal is lower than that of ceramic, the natural frequencies are lower at the material gradation index values where the metal is high, compared to the smaller values of the material gradation index where the ceramic is high.

For just constant material properties at $p=1.5$, Figure 7 shows the fluctuations in dimensionless frequencies that rely on the porosity index and porosity distribution considering different material porosity models. The dimensionless frequencies' typical variational behaviors are nonlinear. As shown in Figure 7a, b, as the increases material porosity index parameter α , the first frequency increases, and the second frequency value decreases, respectively. For example, the porosity index value $\alpha=0.1$ and 0.6, and the first frequency value has been obtained as $\lambda_1 = 7.05$ and 10.75, respectively. According to these values, it is clearly seen that the dimensionless first frequency value has increased by a

Table 9. Comparison of non-dimensional higher order frequencies ($\bar{\omega}$) of simply supported plate ($a = 10$, $a/b = 1$, $a/h = 100$, $E = 30 \times 10^6$, $\nu = 0.3$).

	Model 1		Reduction rate (%)	Model 2		Reduction rate (%)	Model 3		Reduction rate (%)	Model 4		Reduction rate (%)
	$p=0.2$	$p=6$		$p=0.2$	$p=6$		$p=0.2$	$p=6$		$p=0.2$	$p=6$	
λ_1	11.8	8.15	44.7	9.55	7.6	25.65	9.43	7.58	24.4	9.37	7.5	24.9
λ_2	19.66	8.62	128.07	18.32	11.83	54.8	18.69	11.86	57.6	18.1	11.49	57.5
λ_3	58.36	30.83	89.3	50.61	34.83	45.3	51.55	35.04	47.1	50.07	30.04	66.6
	$\alpha=0.1$	$\alpha=6$		$\alpha=0.1$	$\alpha=6$		$\alpha=0.1$	$\alpha=6$		$\alpha=0.1$	$\alpha=6$	
λ_1	7.05	10.75	52.4	6.86	9.01	23.8	6.88	9.21	25.2	6.84	8.75	21.8
λ_2	15.02	7.9	47.4	15.46	12.5	19.1	15.54	13.16	15.3	15.37	11.72	23.7
λ_3	39.67	36.43	8.16	40.16	39.2	2.4	40.35	40.81	1.14	39.93	37.34	6.5
	$p=0.2$	$p=6$		$p=0.2$	$p=6$		$p=0.2$	$p=6$		$p=0.2$	$p=6$	
$\lambda_1 e_0 a = 0$	9.98	7.34	26.4	8.77	6.97	20.5	8.84	6.98	21.04	8.73	6.93	20.6
$\lambda_1 e_0 a = 1$	2.19	1.6	27	1.92	1.53	20.3	1.94	1.53	21.1	1.91	1.52	20.4
$\lambda_1 e_0 a = 2$	1.11	0.81	27	0.98	0.78	20.4	0.98	0.78	20.4	0.97	0.77	20.6
$\lambda_1 e_0 a = 4$	0.56	0.41	26.7	0.49	0.39	20.4	0.49	0.39	20.4	0.47	0.38	19.1

**Figure 7.** Comparison of the variation of the dimensionless fundamental frequency for porosity index $\alpha = 0-0.6$ and different porosity distribution functions of the core plate; for material gradation index of core plate $p = 1.5$; aspect ratio $a/h = 10$; face plate material Barium 50% and Cobalt 50%; nonlocal parameter $e_0 a = 0$; material size parameter $l_m = 0$; temperature rise $\Delta T = 0$; external electric potential $V_0 = 0$; external magnetic potential $H_0 = 0$; (a) the fundamental frequency parameter λ_1 , (b) the second frequency parameter λ_2 , (c) the third frequency λ_3 .

ratio of 52.5%. The other maximum and minimum frequency values have been given in Table 9 with the frequency increment ratio. As shown in Figure 7c, as the material porosity index increases, the third frequency value firstly decreases up to the porosity index $\alpha = 0.25$ and then rises up to the porosity index $\alpha = 0.6$ for the only porosity model 3. On the other hand, as the increases material porosity index value, the third frequency value decreases gradually for the other porosity models (Models 1, 2, and 4).

According to the material composition of p between 0 and 6 for a constant porosity index of $\alpha = 0.25$ and various

models of the porosity distribution, Figure 8 shows the influence of Eringen's nonlocal parameter considering different material porosity models given in Figure 2 considering material size parameter $l_m = 0$. The stiffness-reducing impact of the nonlocal parameter causes the frequencies to drop depending on the sizes of the nonlocal parameter, where $e_0 a = 0, 1, 2$, and 4 nm^2 . Generally, as shown in Figure 8, as the increases the material gradation index value p , the dimensionless first frequency value λ_1 decreases, and the slope of this decrease is enormous, especially in the range of $p \in [0, 2]$. As the p -value increases, the slope of the graph

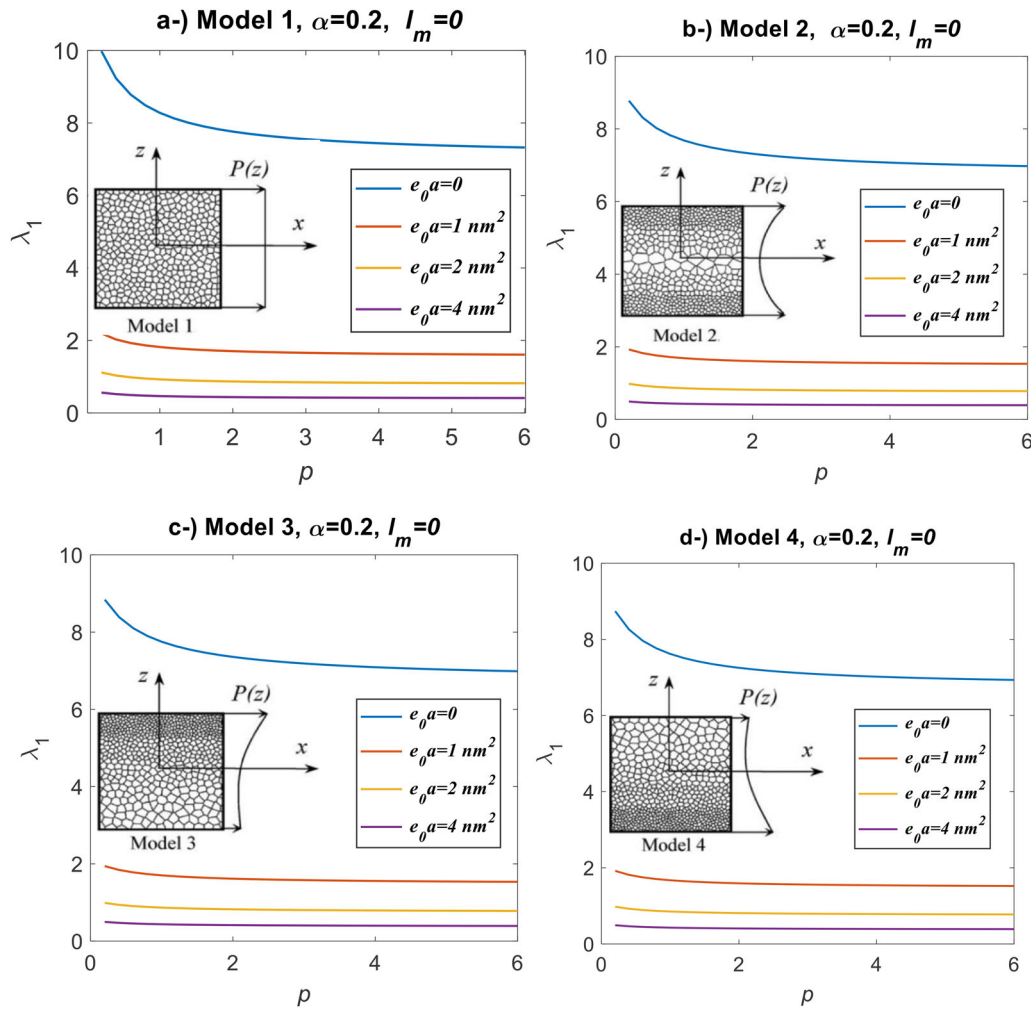


Figure 8. Comparison of the first dimensionless frequencies λ_1 , depending on the material gradation index of core plate $p=0-6$ and different models of porosity distributions of the core plate; for the porosity index $\alpha=0.25$ (resinleri 0.25 yap); aspect ratio $a/H=10$; face plate material Barium 50% and Cobalt %50; four different nonlocal parameters $e_0a=0, 1, 2, 4 \text{ nm}^2$; material size parameter $l_m=0$; temperature rise $\Delta T=0$; external electric potential $V_0=0$; external magnetic potential $H_0=0$; (a) Model 1, (b) Model 2, (c) Model 3, (d) Model 4.

decreases and becomes parallel to the x -axis. The dimensionless frequencies are computed as 2.19, 1.92, 1.94, and 1.91 at the material gradation index $p=0.2$ and as 1.6, 1.53, 1.54, and 1.52 at $p=6$ for porosity models of 1, 2, 3, and 4, respectively, when porosity models are compared for the nonlocal parameter $e_0a=1 \text{ nm}^2$. The computed frequency reduction rates are 26.9, 20.3, 20.6, and 20.4%, respectively. The other reduction rate and frequency values have been given in Table 3 for the other nonlocal parameters.

Figure 9a, b depict the fluctuations of the dimensionless frequency λ_1 of the nanoplate in response to temperature difference ΔT and material grading index p considering different material porosity models given in Figure 2. As shown in Figure 9a, the dimensionless first frequency values decrease to 690 and 649 K (buckling temperatures) for Model 1 and Models 2–4, respectively, with the material gradation indices $p=1$ and frequency values equal to zero. After this temperature point, the first dimensionless frequency value increases gradually for all porosity models given in Figure 2. The dimensionless frequencies in Models 2, 3, and 4 are comparable, but Model 1 yields slightly larger values for the zoomed region. On the other hand, Figure 9b

shows this comparison for the material gradation indices $p=5$. As shown in the figure, the buckling temperature has been obtained as 723 and 672 K for Model 1 and Models 2–4, respectively. According to these values, it is clearly seen that as the increases material gradation indices p -value, the nonlinear temperature rises equal to the buckling temperature of the FGM nanoplate increases too.

The dimensionless frequency λ_1 variations of the FGM nanoplate for a constant porosity ratio $\alpha=0.25$ and nonlocal parameter e_0a are shown in Figure 10a, b in relation to temperature rise ΔT and material grading index p . The effects of the material gradation index p and porosity distribution functions on the dimensionless frequency and buckling temperature variations are shown in Figure 10a, b in behaviors similar to those in Figure 9a, b. As shown in Figure 10a, b, as the increasing temperature difference the dimensionless first frequency values decrease gradually up to buckling frequency and then increase again. But in Figure 10a, b, because of the softening effect of the nonlocal parameter, the dimensionless first frequency value λ_1 is smaller than given in Figure 9a, b. For example, for Model 1, the dimensionless first frequency value λ_1 has been obtained as 7.58

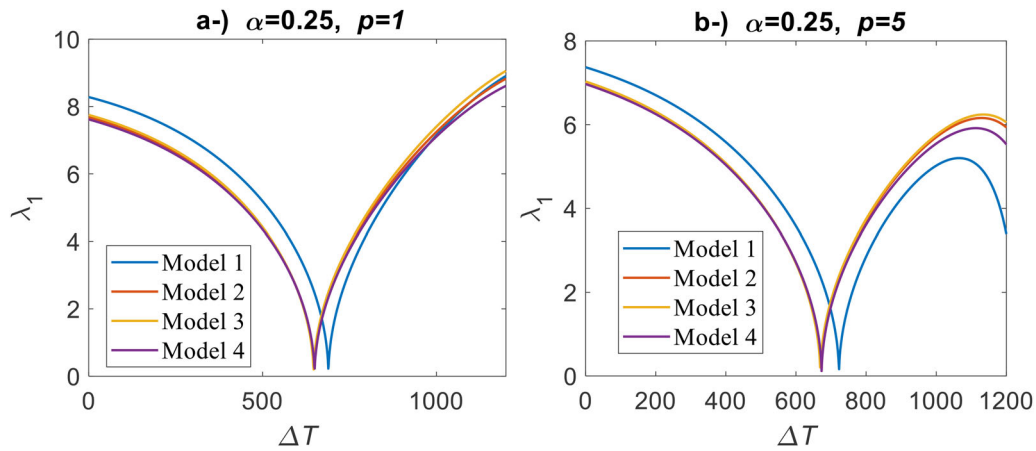


Figure 9. Comparison of the first dimensionless frequencies λ_1 depending on the nonlinear temperature rise; and different models of porosity distributions of the core plate; for the porosity index $\alpha = 0.25$; aspect ratio $a/H = 10$; face plate material Barium 50% and Cobalt %50; nonlocal parameter $e_0 a = 0$; material size parameter $l_m = 0$; temperature rise $\Delta T = 0$; external electric potential $V_0 = 0$; external magnetic potential $H_0 = 0$; (a) material gradation index of core plate $p = 1$, (b) material gradation index of core plate $p = 5$.

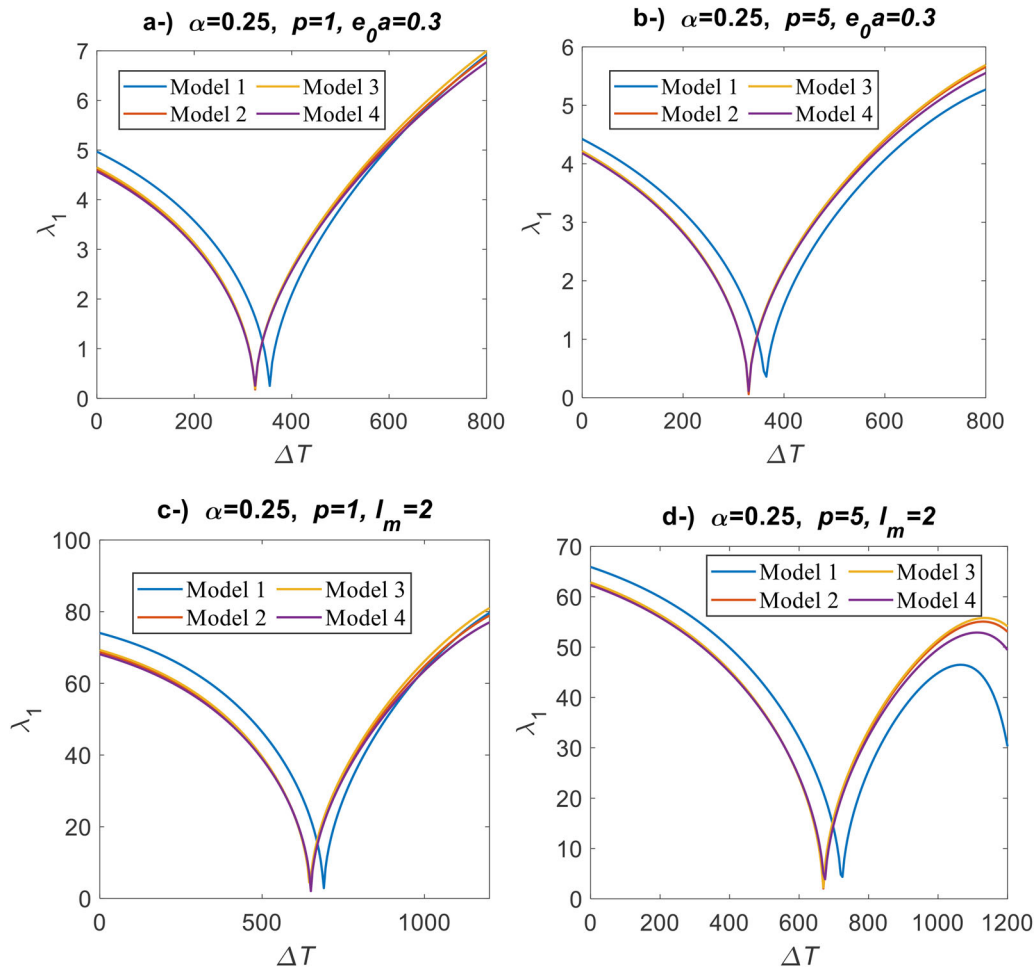


Figure 10. Comparison of the first dimensionless frequencies λ_1 depending on the nonlinear temperature rise; and different models of porosity distributions of the core plate; for the porosity index $\alpha = 0.25$; aspect ratio $a/H = 10$; face plate material Barium 50% and Cobalt %50; temperature rise $\Delta T = 0$; external electric potential $V_0 = 0$; external magnetic potential $H_0 = 0$; (a) material gradation index of core plate $p = 1$ nonlocal parameter $e_0 a = 0.3$, (b) material gradation index of core plate $p = 5$ nonlocal parameter $e_0 a = 0.3$, (c) material size parameter $l_m = 2$, material gradation index of core plate $p = 1$, (d) material size parameter $l_m = 2$, material gradation index of core plate $p = 5$.

for the temperature rise $\Delta T = 200$ K without a nonlocal effect, as shown in Figure 9a. This value is obtained as $\lambda_1 = 3.62$ for the $\Delta T = 200$ K with the nonlocal effect $e_0 a = 0.3$, as shown in Figure 10a. It is clearly seen that the

ratio of %52.2 has reduced the first frequency value. But in Figure 10c, d, because of the hardening effect of the strain gradient parameter effect, the dimensionless first frequency value λ_1 is bigger than given in Figure 9a, b. For example,

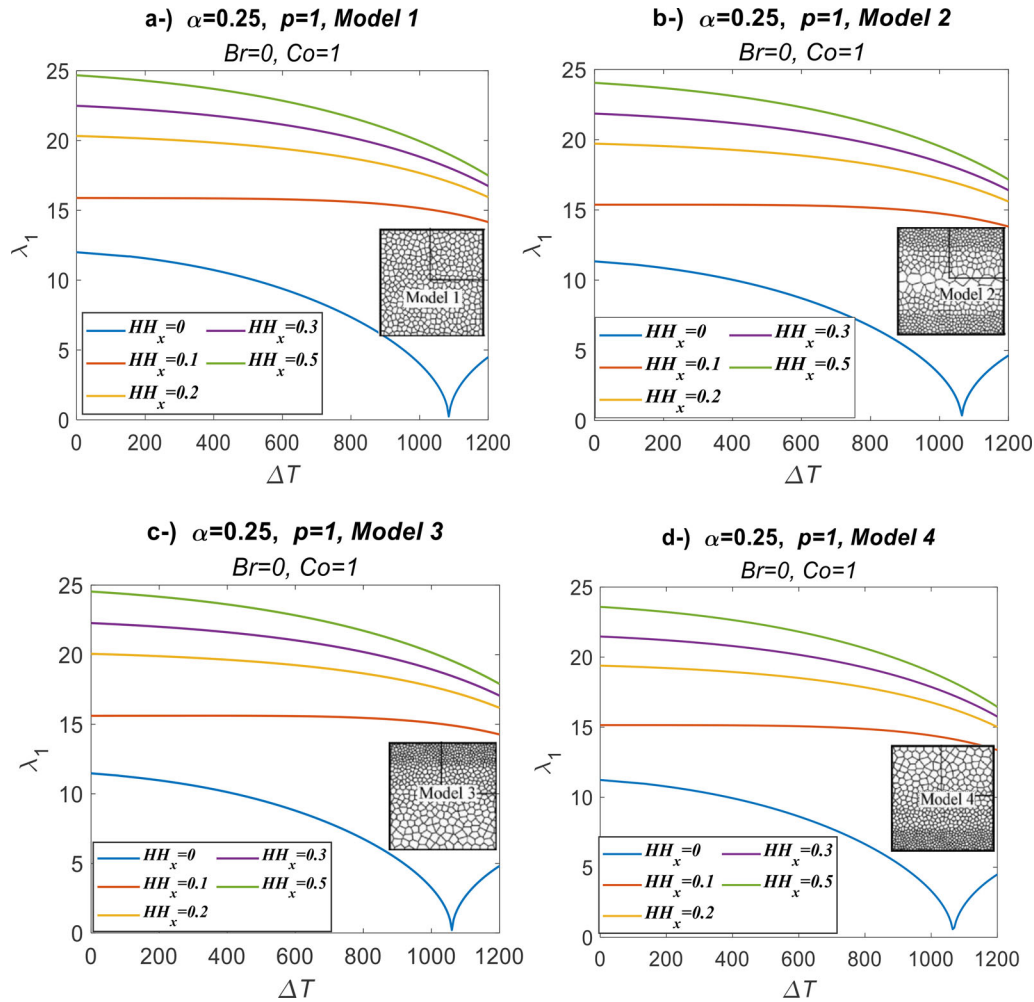


Figure 11. Comparison of the first dimensionless frequencies λ_1 depending on the nonlinear temperature rise; and different models of porosity distributions of the core plate; for the porosity index $\alpha=0.25$; aspect ratio $a/H=10$; face plate material Barium 0% and Cobalt %100; temperature rise $\Delta T=0$; external electric potential $V_0=0$; five different external magnetic potential $HH_x=0, 0.1, 0.2, 0.3$ and 0.5 ; (a) Model 1, (b) Model 2, (c) Model 3, (d) Model 4.

for Model 1, the dimensionless first frequency value λ_1 has been obtained as 7.58 for the temperature rise $\Delta T=200$ K without a strain gradient parameter effect, as shown in Figure 9a. This value is obtained as $\lambda_1=67.2$ for the $\Delta T=200$ K with the nonlocal effect $l_m=2$, as shown in Figure 10a. It is clearly seen that the ratio of %786.5 has increased the first frequency value.

In this section, the effect of the magnetic field intensity upon dimensionless first frequency values has been investigated according to nonlinear temperature rise with the four different porosity models. For this purpose, firstly, the following parameter relative magnetic field intensity has been defined.

$$HH^x = \frac{H_x}{D}, \quad D = \frac{EH^3}{12(1-\nu^2)} \quad (57)$$

The dimensionless frequency λ_1 fluctuations of the nanoplate for the constant porosity ratio $\alpha=0.25$ and the five different relative magnetic field intensity parameters ($HH_x=0, HH_x=0.1, HH_x=0.2, HH_x=0.3$, and $HH_x=0.5$) and four different porosity models are shown in Figure 11a–d in relation to temperature increase $\Delta T=[0, 1200]$, material grading index $p=1$. In this analysis, the face plate material

compound is chosen as $Br=0$ and $Co=1$ to make an effective magnetic field upon plate dynamic response. Figure 11a shows the effect of the five different relative magnetic field intensity parameters upon the first dimensionless frequency for the porosity Model 1. As shown in Figure 11a–d, as the increasing temperature difference the dimensionless first frequency values decrease gradually up to buckling frequency and then increase again. But in Figure 11a–d, because of the hardening effect of the magnetic field intensity parameter, as the increase relative magnetic field intensity value, the dimensionless first frequency increases too. For example, for Model 1, given in Figure 11a, the dimensionless first frequency value λ_1 has been obtained as 11.56 for the temperature rise $\Delta T=200$ K without a magnetic field intensity effect ($HH_x=0$), as shown in Figure 11a. These values have been obtained as 15.87, 20.13, 22.2, and 24.2 for the relative magnetic field intensity ($HH_x=0.1, HH_x=0.2, HH_x=0.3$, and $HH_x=0.5$), respectively. According to these values, it is clearly seen that the first dimensionless frequency of the plate increases by the ratio of 37.2, 74.1, 92, and 109.3% for the parameters $HH_x=0.1, HH_x=0.2, HH_x=0.3$, and $HH_x=0.5$ respectively. Another important point highlighted in Figure 11a–d is that the buckling temperature of the FGM plates

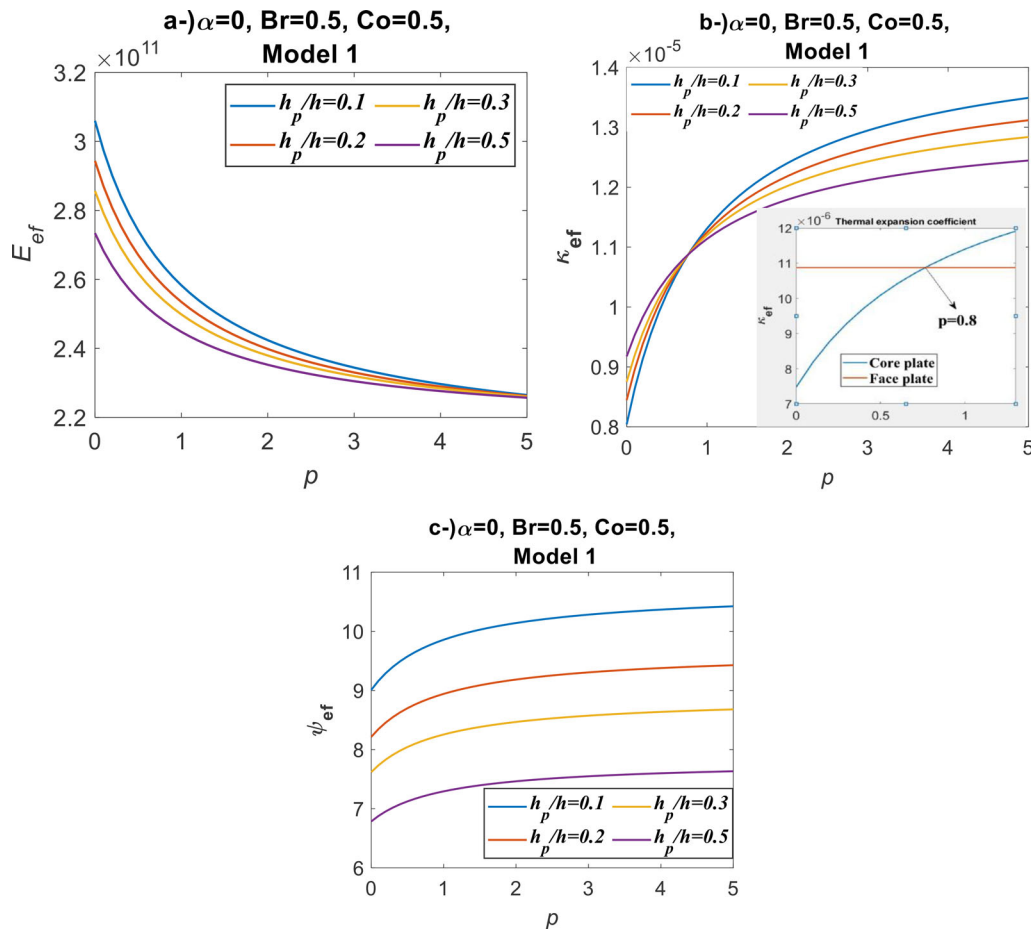


Figure 12. The variation of the effective properties of the whole plate depends on the material gradation index ($p=0-5$) of the core plate and the thickness ratio of the face plate to the core plate ($h_p/h=0.15, 0.2, 0.3$, and 0.5); for the porosity index $\alpha=0$; aspect ratio $a/H=10$; face plate material Barium 50% and Cobalt %50; nonlocal parameter $e_0a=0$; material size parameter $l_m=0$; temperature rise $\Delta T=0$; external electric potential $V_0=0$; external magnetic potential $H_0=0$; for the porosity Model 1; (a) Effective elasticity module E_{ef} , (b) effective thermal expansion coefficient κ_{ef} , (c) thermal conductivity coefficient ψ_{ef} .

corresponding to the first dimensionless frequency increases as the relative magnetic field intensity effect increases.

Another critical parameter that affects the plate's dynamic responses is the ratio of the face plate thickness to the core plate thickness (h_p/h). For this purpose, in Figure 12, the effect of the relative plate thickness upon plate dynamic behavior according to material gradation indices is investigated with the face plates material compound $Br=0.5$, $Co=0.5$, nonlocal parameter $e_0a=0$, material scale factor $l_m=0$ considering different material porosity model. This analysis fixed the total plate thickness with a value of 0.1 m. When the thickness of the face plate increases, the core plate's thickness decreases gradually, so the complete plate's thickness is constant. As shown in Figure 12a, as the relative plate thickness (h_p/h) increases, the effective elasticity modulus of the whole plate E_{ef} value decreases for any material gradation indices p . For example, the effective material elasticity module of the entire plate has been obtained as $2.6e11$, $2.55e11$, $2.51e11$, and $2.46e11$ GPa for the relative thickness values ($h_p/h=0.1, 0.2, 0.3$, and 0.5), respectively. This is because as the increase ratio of the h_p/h , the thickness of the face plate becomes bigger than the core plate's thickness. As a result, the face plate's material content consists of $CoFe_2O_4$ and $BaTiO_3$, and their elasticity modulus is smaller than the core plate material content (Si_3Ni_4 and $SUS304$). In

the material gradation index value range $p=0-1$, the rapidly decreasing of the effective elasticity module E_{ef} has been obtained. After that, the value material gradation index p is bigger than 1, and the curve is nearly parallel to the x -axis.

Moreover, Figure 12b shows the change of the FGM plate thermal expansion coefficient κ_{ef} according to material gradation index value p , considering different relative plate thickness ratios for the porosity Model 1. As shown in the figure, as the relative plate thickness ratio increases, the thermal expansion coefficient increases, too, in the range of material gradation index $p=[0-0.8]$ because the face plate material's thermal expansion coefficient is bigger than the core plate material ones. After the value $p > 0.8$, as the increases relative thickness ratio of the plate, the effective thermal expansion coefficient decreases, as shown in the figure, because after the value $p > 0.8$, the face plate's thermal expansion coefficient is bigger than the core plate material effective thermal expansion coefficient. In the material gradation index value range $p=0-1$, the rapidly increasing effective thermal expansion coefficient κ_{ef} has been obtained. After that, the value material gradation index p is bigger than 1, and the curve is nearly parallel to the x -axis. On the other hand, Figure 12c shows the effective thermal conductivity ψ_{ef} of the entire plate with the face plates material compound $Br=0.5$, $Co=0.5$, nonlocal parameter $e_0a=0$,

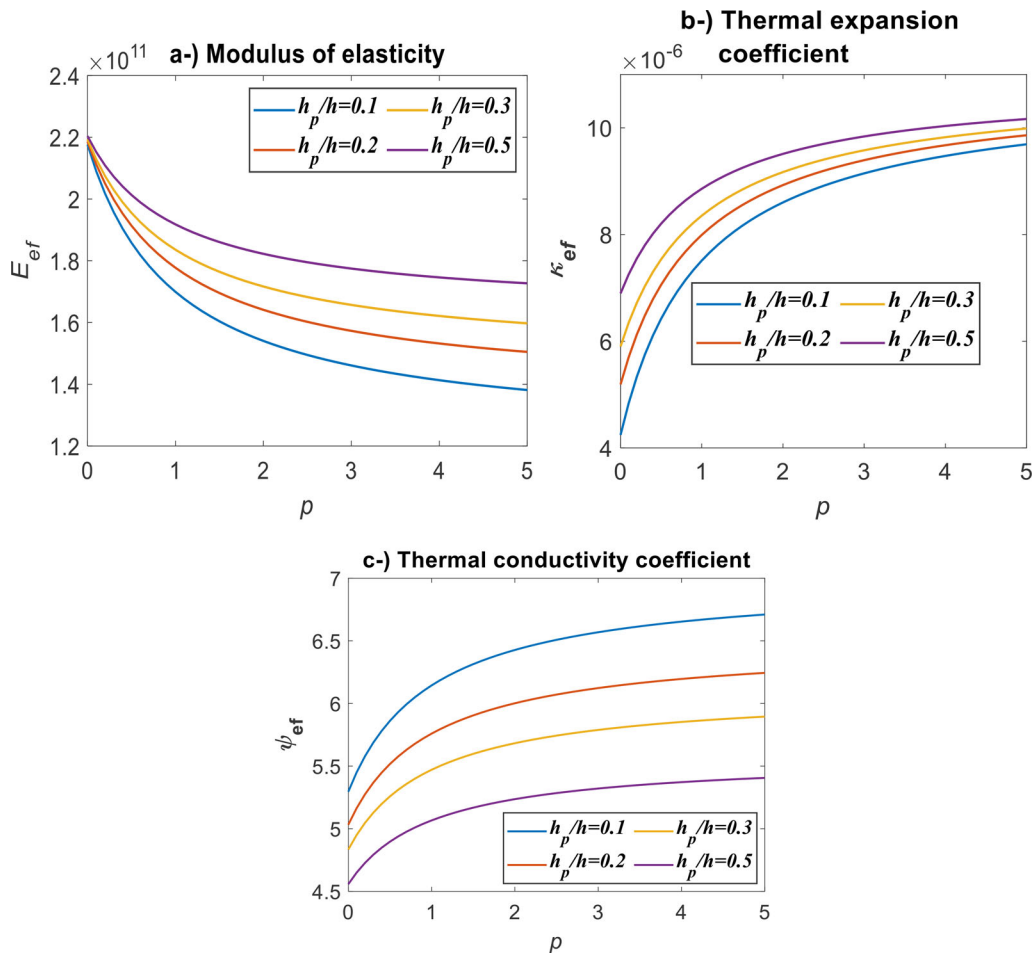


Figure 13. The variation of the effective properties of the whole plate depends on the material gradation index ($p=0-5$) of the core plate and the thickness ratio of the face plate to the core plate ($h_p/h=0.15, 0.2, 0.3$, and 0.5); for the porosity index $\alpha=0.4$; aspect ratio $a/H=10$; face plate material Barium 50% and Cobalt %50; nonlocal parameter $e_0a=0$; material size parameter $l_m=0$; temperature rise $\Delta T=0$; external electric potential $V_0=0$; external magnetic potential $H_0=0$; for the porosity Model 1; (a) Effective elasticity module E_{ef} , (b) effective thermal expansion coefficient κ_{ef} , (c) thermal conductivity coefficient ψ_{ef} .

material scale factor $l_m=0$ considering different material porosity models for the relative thickness values ($h_p/h=0.1, 0.2, 0.3$, and 0.5). As shown in the figure, as the relative plate thickness ratio increases, the thermal conductivity coefficient increases, too, because the face plate material's thermal conductivity coefficient is bigger than the core plate material ones. In the material gradation index value range $p=0-1$, the rapidly increasing effective thermal expansion coefficient κ_{ef} has been obtained. After that, the value material gradation index p is bigger than 1, and the curve is nearly parallel to the x -axis.

Figure 13a-c shows the same analysis with the material porosity ratio $\alpha=0.4$. The other analysis parameter is chosen the same as given in the Figure 12a-c analysis. As shown in Figure 13a, as the relative plate thickness h_p/h increases, the effective material elasticity modules of the whole plate increase, too, unlike Figure 12. The reason for this situation is the material porosity index added to the plate, which weakens the structure. On the other hand, Figure 13b shows the effective thermal expansion coefficient according to material gradation index p with the core plate material porosity ratio $\alpha=0.4$ the face plates material compound $Br=0.5, Co=0.5$, nonlocal parameter $e_0a=0$, material scale factor $l_m=0$. As shown in the figure, as the relative

plate thickness ratio increases, the effective thermal expansion coefficient increases, too, unlike the given analysis in Figure 12b, with the porosity ratio $\alpha=0$. Furthermore, Figure 13c shows the effective thermal conductivity coefficient according to material gradation index p with the core plate material porosity ratio $\alpha=0.4$, the face plates material compound $Br=0.5, Co=0.5$, nonlocal parameter $e_0a=0$, material scale factor $l_m=0$. As shown in the figure, as the relative plate thickness ratio increases, the effective thermal conductivity coefficient decreases.

Figure 14 shows the first dimensionless frequency λ_1 of the FGM nano plate according to material gradation index in the range of $p \in [0, 5]$ considering different plate relative thickness ratios ($h_p/h=0.1, 0.2, 0.3$, and 0.5) core plate material porosity ratio $\alpha=0.4$ the face plates material compound $Br=0.5, Co=0.5$, nonlocal parameter $e_0a=0$, material scale factor $l_m=0$. As shown in the figure, as the relative plate thickness ratio increases, the first dimensionless frequency value decreases for the material gradation index value p . For example, for the material gradation index $p=2$, the first dimensionless frequency value has been obtained as 10.2, 5.7, 4.2, and 3.03, considering the relative plate thickness ratio ($h_p/h=0.1, 0.2, 0.3$, and 0.5), respectively. On the other hand, a significant decrease is observed in the range of

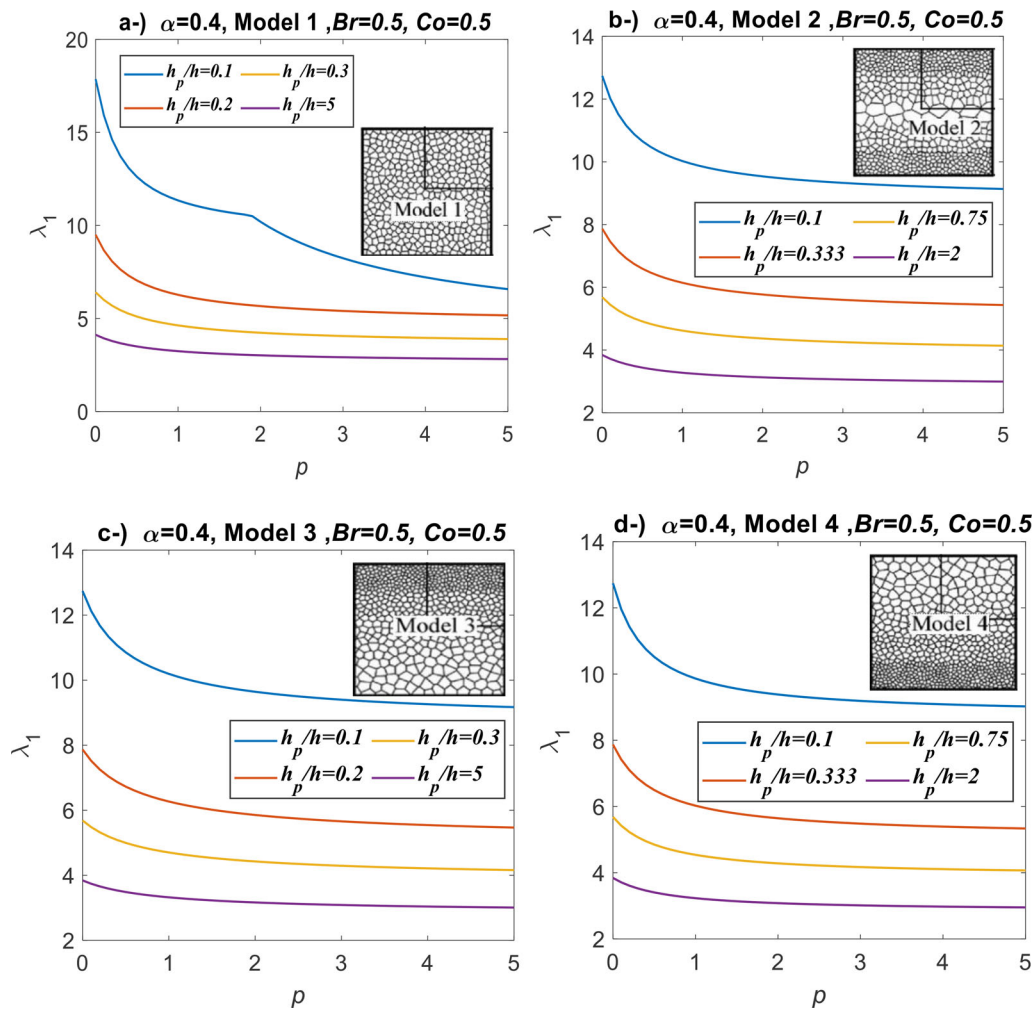


Figure 14. The variation of the dimensionless fundamental frequency depends on the material gradation index ($\rho=0-5$) of the core plate and the thickness ratio of the face plate to the core plate ($h_p/h=0.15, 0.2, 0.3$, and 0.5); for the porosity index $\alpha=0.4$; aspect ratio $a/H=10$; face plate material Barium 50% and Cobalt %50; nonlocal parameter $e_0 a=0$; material size parameter $l_m=0$; temperature rise $\Delta T=0$; external electric potential $V_0=0$; external magnetic potential $H_0=0$; (a) Model 1: Uniform porosity; (b) Model 2: Symmetric porosity; (c) Model 3: Bottom porosity; (d) Model 4: Top porosity.

material gradation index $\rho \in [0, 1]$, especially for the small relative plate thickness ratio ($h_p/h=0.1$). Moreover, Figure 14b–d show the same analysis for the material porosity models 2, 3, and 4, respectively. Consequently, the same results as Figure 14a have been determined for all material porosity models.

4. Conclusions

In this study, the thermomechanical free vibration response of nanoplates with magneto-electro elastic face layers and functionally graded porous core plate has been investigated HDST and nonlocal strain gradient theory. The functionally graded porous core plate and magneto-electro elastic face plates consist of Si_3N_4 and SUS304, and CoFe_2O_4 and BaTiO_3 , respectively. The Si_3N_4 and stainless steel (SUS304) mixture's porosity as a result of the technology currently in use during the sintering process was taken into account. The impact of porosity was examined using the uniform, symmetrical, asymmetric ascending downward and up porosity models and four alternative porosity models. Firstly, the effective material properties (elasticity modulus, Poisson

ratio, thermal expansion, and thermal conductivity coefficients) have been analyzed, considering different material gradation index ρ , material porosity ratios, and different porosity models according to nonlinear temperature rise. Consequently, the obtained results from these simulations have been summarized as follows:

- Because the elasticity module of the ceramic is larger than the metallic one, the effective elasticity modulus progressively drops with the increasing material gradation indices (SUS304). Although the ceramic compositions' increment ratio is more noticeable than those rich in metals, the effective thermal expansion coefficient κ_{ef} rises linearly with temperature. The thermal conductivity coefficient ψ_{ef} rises nonlinearly with temperature for metal-rich or entirely metallic materials. On the other hand, with the composition rich in ceramics, the thermal conductivity characteristics fall as the temperature rises.
- As the porosity ratio rises, the value of the effective material qualities decreases. The effective elasticity modulus E_{ef} of the FGM plates drops as the nonlinear temperature rise ΔT increases, but the effective Poisson ratio

ν_{ef} and effective thermal expansion coefficients κ_{ef} increase. However, the coefficient of thermal conductivity increased nonlinearly after decreasing up to around 600 K.

Secondly, the first three dimensionless frequency variations of the FGM nanoplate have been investigated considering different material gradation index p , porosity ratio of core plate material α , nonlocal parameter e_0a , different core plate material porosity models, and different magnetic potential H_0 . Consequently, the obtained results from these simulations have been summarized as follows:

- The FGM plate's first three dimensionless frequencies steadily decrease when material gradation index p is increased. The first frequency λ_1 increases, and the second frequency λ_2 value falls as the material porosity index α parameter increases. The dimensionless first frequency value λ_1 reduces as the material gradation index value p decreases, and the slope of this decline is quite sharp, particularly in the region of $p \in [0, 2]$.
- With the material gradation indices $p = 1$ and frequency values equal to zero, the dimensionless first frequency values for Model 1 and Models 2–4, respectively, drop to 690 and 649 K (buckling temperatures). The dimensionless first frequency values decrease to 690 and 649 K (buckling temperatures) for Model 1 and Models 2–4, respectively, with the material gradation indices $p = 1$ and frequency values equal to zero. After this temperature point, the first dimensionless frequency value increases gradually.
- The dimensionless first frequency values steadily decrease up to the buckling frequency and then increase as the temperature difference increases. The effect of the five different relative magnetic field intensity parameters has been investigated upon the first dimensionless frequency for the porosity Model 1. As shown in Figure 11a–d, as the increasing temperature difference the dimensionless first frequency values decrease gradually up to buckling frequency and then increase again.
- The effective elasticity modulus of the plate is significantly influenced by the relative thickness of the face plate and the core plate, with an increase in the relative thickness of the face plate resulting in a decrease in the overall effective elasticity modulus because the face plate material has a lower elasticity modulus. The connection between the thermal expansion coefficient, conductivity, relative thickness of the plate, and material gradation index of a plate having a gradient in its material characteristics is complicated. Up to a specific range of the material gradation index, the thermal expansion coefficient and conductivity both rise with the relative thickness of the plate before falling. When the material gradation index is bigger than 1, the thermal expansion coefficient and conductivity first grow quickly in the 0–1 range of the index before becoming virtually parallel to the x -axis.

The study's conclusions can be used to design and optimize engineering structures and devices that use nanoplates with magneto-electro elastic face layers and a functionally graded porous core plate, taking into account the effects of material gradation indices, porosity ratios and various porosity models on their thermomechanical free vibration response, buckling load, and critical buckling temperature. The thermomechanical free vibration response, buckling load, and critical buckling temperature of nanoplates with magneto-electro elastic face layers and a functionally graded porous core plate are all thoroughly analyzed in this paper. The porosity ratios, material gradation indices, and other porosity models were discovered to influence these nanoplates' behavior substantially. It is feasible to develop and optimize engineering systems and structures that use these materials for increased performance, dependability, and durability by carefully considering these variables. The design of MEMS devices, sensors, actuators, and other micro- and nano-scale structures and devices that require high strength, stiffness, and temperature resistance can all benefit from these discoveries. The results of the current study, in addition to those already mentioned, emphasize the significance of taking nonlocal strain gradient effects into account when analyzing the thermomechanical free vibration response of nanoplates with magneto-electro elastic face layers and functionally graded porous core plates. In comparison to the traditional plate theory, the nonlocal strain gradient theory is shown to provide more precise predictions of the plate's natural frequencies and buckling temperatures, particularly for small-sized nanoplates. For a more precise characterization of comparable structures' dynamic behavior, it is advised that future research include the nonlocal strain gradient effects as well.

ORCID

Mehmet Akif Koç  <http://orcid.org/0000-0001-7461-9795>

İsmail Esen  <http://orcid.org/0000-0002-7853-1464>

Mustafa Eroğlu  <http://orcid.org/0000-0002-1429-7656>

References

- [1] Y.-F. Zhao, S.-Q. Zhang, X. Wang, S.-Y. Ma, G.-Z. Zhao, and Z. Kang, Nonlinear analysis of carbon nanotube reinforced functionally graded plates with magneto-electro-elastic multiphase matrix, *Compos. Struct.*, vol. 297, pp. 115969, 2022. DOI: [10.1016/j.compstruct.2022.115969](https://doi.org/10.1016/j.compstruct.2022.115969).
- [2] M. Vinyas, Computational analysis of smart magneto-electro-elastic materials and structures: review and classification, *Arch. Comput. Methods Eng.*, vol. 28, no. 3, pp. 1205–1248, 2021. DOI: [10.1007/s11831-020-09406-4](https://doi.org/10.1007/s11831-020-09406-4).
- [3] F. Zhang, C. Bai, and J. Wang, Study on dynamic stability of magneto-electro-thermo-elastic cylindrical nanoshells resting on Winkler–Pasternak elastic foundations using nonlocal strain gradient theory, *J. Braz. Soc. Mech. Sci. Eng.*, vol. 45, no. 1, pp. 23, 2023. DOI: [10.1007/s40430-022-03930-z](https://doi.org/10.1007/s40430-022-03930-z).
- [4] A.I. Journal, I. Esen, and R. Özmen, Free and forced thermo-mechanical vibration and buckling responses of functionally graded magneto-electro-elastic porous nanoplates, *Mech. Based Des. Struct. Mach.*, vol. 0, pp. 1–38, 2022. DOI: [10.1080/15397734.2022.2152045](https://doi.org/10.1080/15397734.2022.2152045).

- [5] K. Madrahalli Chidanandamurthy, W. Wang, C. Fang, and S. Kattimani, Static, buckling, and free vibration characteristics of porous skew partially functionally graded magneto-electro-elastic plate, *Mech. Based Des. Struct. Mach.*, pp. 1–36, 2021. DOI: [10.1080/15397734.2021.2008257](https://doi.org/10.1080/15397734.2021.2008257).
- [6] V. Mahesh, and A.S. Mangalasseri, Agglomeration effects of CNTs on the energy harvesting performance of multifield interactive magneto-electro-elastic/nanocomposite unimorph smart beam, *Mech. Based Des. Struct. Mach.*, pp. 1–27, 2022. DOI: [10.1080/15397734.2022.2144886](https://doi.org/10.1080/15397734.2022.2144886).
- [7] S. Thai, V.X. Nguyen, and Q.X. Lieu, Bending and free vibration analyses of multi-directional functionally graded plates in thermal environment: A three-dimensional Isogeometric Analysis approach, *Compos. Struct.*, vol. 295, pp. 115797, 2022. DOI: [10.1016/j.compstruct.2022.115797](https://doi.org/10.1016/j.compstruct.2022.115797).
- [8] I. Khader, C. Koplin, C. Schröder, J. Stockmann, W. Beckert, W. Kunz, and A. Kailer, Characterization of a silicon nitride ceramic material for ceramic springs, *J. Eur. Ceram. Soc.*, vol. 40, no. 10, pp. 3541–3554, 2020. DOI: [10.1016/j.jeurceramsoc.2020.03.046](https://doi.org/10.1016/j.jeurceramsoc.2020.03.046).
- [9] E. Schwarzer-Fischer, E. Zschippang, W. Kunz, C. Koplin, Y.M. Löw, U. Scheithauer, and A. Michaelis, CerAMufacturing of silicon nitride by using lithography-based ceramic vat photopolymerization (CerAM VPP), *J. Eur. Ceram. Soc.*, vol. 43, no. 2, pp. 321–331, 2023. DOI: [10.1016/j.jeurceramsoc.2022.10.011](https://doi.org/10.1016/j.jeurceramsoc.2022.10.011).
- [10] Y. Yang, D. Cai, Z. Yang, X. Duan, P. He, D. Jia, and Y. Zhou, Rheology of organics-free aqueous ceramic suspensions for additive manufacturing of dense silicon nitride ceramics, *Ceram. Int.*, vol. 48, no. 21, pp. 31941–31951, 2022. DOI: [10.1016/j.ceramint.2022.07.130](https://doi.org/10.1016/j.ceramint.2022.07.130).
- [11] K. Zhao, L. Dong, Y. Zheng, G. Deng, Z. Li, S. Qu, K. Chen, and J. Wu, Optimization of light-analyte interaction in Si₃N₄/polymer hybrid waveguide for sensitive sensing of pyridine vapor with ppb-level detection limit, *Sensors Actuators B Chem.*, vol. 377, pp. 133104, 2023. DOI: [10.1016/j.snb.2022.133104](https://doi.org/10.1016/j.snb.2022.133104).
- [12] L. Selvarajan, R. Rajavel, K. Venkataramanan, and V.P. Srinivasan, Experimental investigation on surface morphology and recasting layer of Si₃N₄-TiN composites machined by die-sinking and rotary EDM, *Ceram. Int.*, vol. 49, no. 5, pp. 8487–8501, 2023. DOI: [10.1016/j.ceramint.2022.11.011](https://doi.org/10.1016/j.ceramint.2022.11.011).
- [13] B. Bai, R. Zhou, G. Yang, W. Zou, and W. Yuan, The constitutive behavior and dissociation effect of hydrate-bearing sediment within a granular thermodynamic framework, *Ocean Eng.*, vol. 268, pp. 113408, 2023. DOI: [10.1016/j.oceaneng.2022.113408](https://doi.org/10.1016/j.oceaneng.2022.113408).
- [14] J. Lu, W. Liu, and Y. Zhao, Anisotropy in electrochemical jet texturing of rolled stainless steel SUS304, *Mater. Des.*, vol. 215, pp. 110500, 2022. DOI: [10.1016/j.matdes.2022.110500](https://doi.org/10.1016/j.matdes.2022.110500).
- [15] T. Tang, Q. Shi, B. Lei, J. Zhou, Y. Gao, Y. Li, G. Zhang, and G. Chen, Transition of interfacial friction regime and its influence on thermal responses in rotary friction welding of SUS304 stainless steel: A fully coupled transient thermomechanical analysis, *J. Manuf. Process.*, vol. 82, pp. 403–414, 2022. DOI: [10.1016/j.jmapro.2022.08.016](https://doi.org/10.1016/j.jmapro.2022.08.016).
- [16] H. He, W. Tian, J. Li, K. Shi, M. Sun, and J. Li, Failure analysis and finite element simulation on service conditions of SUS304 stainless steel, *J. Mater. Eng. Perform.*, vol. 30, no. 8, pp. 5987–5999, 2021. DOI: [10.1007/s11665-021-05744-x](https://doi.org/10.1007/s11665-021-05744-x).
- [17] Q. Zheng, X. Zhuang, and Z. Zhao, Flow behavior of SUS304 stainless steel under a wide range of forming temperatures and strain rates, *Metal. Mater. Trans. A*, vol. 52, no. 12, pp. 5200–5214, 2021. DOI: [10.1007/s11661-021-06447-7](https://doi.org/10.1007/s11661-021-06447-7).
- [18] J. Sakamoto, N. Tada, and T. Uemori, Effect of resin lamination on tensile strength characteristics of SUS304 stainless steel thin film, *Int. J. Adv. Manuf. Technol.*, vol. 116, no. 3–4, pp. 1081–1088, 2021. DOI: [10.1007/s00170-021-07510-8](https://doi.org/10.1007/s00170-021-07510-8).
- [19] B. Cao, T. Iwamoto, and P.P. Bhattacharjee, An experimental study on strain-induced martensitic transformation behavior in SUS304 austenitic stainless steel during higher strain rate deformation by continuous evaluation of relative magnetic permeability, *Mater. Sci. Eng. A*, vol. 774, pp. 138927, 2020. DOI: [10.1016/j.msea.2020.138927](https://doi.org/10.1016/j.msea.2020.138927).
- [20] D. Savastru, S. Miclos, R. Savastru, and I.I. Lancranjan, Analysis of mechanical vibrations applied on a LPGFS smart composite polymer material, *Compos. Struct.*, vol. 226, pp. 111243, 2019. DOI: [10.1016/j.compstruct.2019.111243](https://doi.org/10.1016/j.compstruct.2019.111243).
- [21] M.M. Shahzamanian, A. Partovi, and P.D. Wu, Finite element analysis of elastic-plastic and fracture behavior in functionally graded materials (FGMs), *SN Appl. Sci.*, vol. 2, no. 12, pp. 2135, 2020. DOI: [10.1007/s42452-020-03901-w](https://doi.org/10.1007/s42452-020-03901-w).
- [22] M. Bayat, I.M. Alarifi, A.A. Khalili, T.M.A.A. El-Bagory, H.M. Nguyen, and A. Asadi, Thermo-mechanical contact problems and elastic behaviour of single and double sides functionally graded brake disks with temperature-dependent material properties, *Sci. Rep.*, vol. 9, no. 1, pp. 15317, 2019. DOI: [10.1038/s41598-019-51450-z](https://doi.org/10.1038/s41598-019-51450-z).
- [23] D. Kumar, D. Kumar, A.M. Tigga, and D. Sagar, Synthesis of Al-B4C functionally graded materials by sound-wave-assisted vibrational casting methodology, *J. Mater. Eng. Perform.*, 2022. DOI: [10.1007/s11665-022-07640-4](https://doi.org/10.1007/s11665-022-07640-4).
- [24] L. Hadji, N. Zouatnia, and A. Kassoul, Wave propagation in functionally graded beams using various higher-order shear deformation beams theories, *Struct. Eng. Mech.*, vol. 62, no. 2, pp. 143–149, 2017. DOI: [10.12989/sem.2017.62.2.143](https://doi.org/10.12989/sem.2017.62.2.143).
- [25] S.A. Yahia, H.A. Atmane, M.S.A. Houari, and A. Tounsi, Wave propagation in functionally graded plates with porosities using various higher-order shear deformation plate theories, *Struct. Eng. Mech.*, vol. 53, no. 6, pp. 1143–1165, 2015. DOI: [10.12989/sem.2015.53.6.1143](https://doi.org/10.12989/sem.2015.53.6.1143).
- [26] L. Hadji, M. Avcar, and N. Zouatnia, Natural frequency analysis of imperfect FG sandwich plates resting on Winkler-Pasternak foundation, *Mater. Today Proc.*, vol. 53, pp. 153–160, 2022. DOI: [10.1016/j.matpr.2021.12.485](https://doi.org/10.1016/j.matpr.2021.12.485).
- [27] L. Sun, G. Grasselli, Q. Liu, and X. Tang, Thermal cracking simulation of functionally graded materials using the combined finite-discrete element method, *Comp. Part. Mech.*, vol. 7, no. 5, pp. 903–917, 2020. DOI: [10.1007/s40571-019-00290-9](https://doi.org/10.1007/s40571-019-00290-9).
- [28] T. Wu, Y. Hu, S. Wang, Y. Leng, and M. Wang, Effect of SiC content and interlayer difference on microstructural characterization and mechanical properties of functionally graded 6061Al/SiCp composites, *Appl. Phys. A*, vol. 126, no. 9, pp. 673, 2020. DOI: [10.1007/s00339-020-03848-0](https://doi.org/10.1007/s00339-020-03848-0).
- [29] A. Oulderyou, H. Mehboob, A. Merdji, L. Aminallah, A. Mehboob, and O.M. Mukdadi, Biomechanical analysis of printable functionally graded material (FGM) dental implants for different bone densities, *Comput. Biol. Med.*, vol. 150, pp. 106111, 2022. DOI: [10.1016/j.combiomed.2022.106111](https://doi.org/10.1016/j.combiomed.2022.106111).
- [30] D.M. Sangeetha, D.T. Naveenkumar, V. Vinaykumar, and K.E. Prakash, Temperature stresses in Functionally graded (FGM) material plates using deformation theory – Analytical approach, *Mater. Today Proc.*, vol. 49, pp. 1936–1941, 2022. DOI: [10.1016/j.matpr.2021.08.130](https://doi.org/10.1016/j.matpr.2021.08.130).
- [31] A. Pasha, and R. B.m, Functionally graded materials (FGM) fabrication and its potential challenges & applications, *Mater. Today Proc.*, vol. 52, pp. 413–418, 2022. DOI: [10.1016/j.matpr.2021.09.077](https://doi.org/10.1016/j.matpr.2021.09.077).
- [32] M. Luginina, D. Angioni, S. Montinaro, R. Orrù, G. Cao, R. Sergi, D. Bellucci, and V. Cannillo, Hydroxyapatite/bioactive glass functionally graded materials (FGM) for bone tissue engineering, *J. Eur. Ceram. Soc.*, vol. 40, no. 13, pp. 4623–4634, 2020. DOI: [10.1016/j.jeurceramsoc.2020.05.061](https://doi.org/10.1016/j.jeurceramsoc.2020.05.061).
- [33] Y. Sitli, K. Mhada, O. Bourihane, and H. Rhanim, Buckling and post-buckling analysis of a functionally graded material (FGM) plate by the Asymptotic Numerical Method, *Structures*, vol. 31, pp. 1031–1040, 2021. DOI: [10.1016/j.istruc.2021.01.100](https://doi.org/10.1016/j.istruc.2021.01.100).
- [34] X.W. Chen, and Z.Q. Yue, Contact mechanics of two elastic spheres reinforced by functionally graded materials (FGM) thin coatings, *Eng. Anal. Bound. Elem.*, vol. 109, pp. 57–69, 2019. DOI: [10.1016/j.enganbound.2019.09.009](https://doi.org/10.1016/j.enganbound.2019.09.009).
- [35] X. Xiao, Q. Zhang, J. Zheng, and Z. Li, Analytical model for the nonlinear buckling responses of the confined polyhedral FGP-GPLs lining subjected to crown point loading, *Eng. Struct.*, vol. 282, pp. 115780, 2023. DOI: [10.1016/j.engstruct.2023.115780](https://doi.org/10.1016/j.engstruct.2023.115780).

- [36] M. Avcar, and W.K.M. Mohammed, Free vibration of functionally graded beams resting on Winkler-Pasternak foundation, *Arab. J. Geosci.*, vol. 11, no. 10, pp. 232, 2018. DOI: [10.1007/s12517-018-3579-2](https://doi.org/10.1007/s12517-018-3579-2).
- [37] W.-Y. Jung, and S.-C. Han, Analysis of sigmoid functionally graded material (S-FGM) nanoscale plates using the nonlocal elasticity theory, *Math. Probl. Eng.*, vol. 2013, pp. 1–10, 2013. DOI: [10.1155/2013/476131](https://doi.org/10.1155/2013/476131).
- [38] M. Hosseini, M.R. Mofidi, A. Jamalpoor, and M. Safi Jahanshahi, Nanoscale mass nanosensor based on the vibration analysis of embedded magneto-electro-elastic nanoplate made of FGMs via nonlocal Mindlin plate theory, *Microsyst. Technol.*, vol. 24, no. 5, pp. 2295–2316, 2018. DOI: [10.1007/s00542-017-3654-8](https://doi.org/10.1007/s00542-017-3654-8).
- [39] M.S.H. Al-Furjan, M.X. Xu, A. Farrokhian, G.S. Jafari, X. Shen, and R. Kolahchi, On wave propagation in piezoelectric-auxetic honeycomb-2D-FGM micro-sandwich beams based on modified couple stress and refined zigzag theories, *Waves Random Complex Medium*, pp. 1–25, 2022. DOI: [10.1080/17455030.2022.2030499](https://doi.org/10.1080/17455030.2022.2030499).
- [40] A. Vahidi-Moghaddam, M.R. Hairi-Yazdi, and R. Vatanikhah, Analytical solution for nonlinear forced vibrations of functionally graded micro resonators, *Mech. Based Des. Struct. Mach.*, vol. 51, no. 3, pp. 1543–1562, 2023. DOI: [10.1080/15397734.2021.1873802](https://doi.org/10.1080/15397734.2021.1873802).
- [41] Z.-Q. Lu, D.-H. Gu, H. Ding, W. Lacarbonara, and L.-Q. Chen, Nonlinear vibration isolation via a circular ring, *Mech. Syst. Signal Process.*, vol. 136, pp. 106490, 2020. DOI: [10.1016/j.ymsp.2019.106490](https://doi.org/10.1016/j.ymsp.2019.106490).
- [42] F. Ebrahimi, and M.R. Barati, Small-scale effects on hygro-thermo-mechanical vibration of temperature-dependent nonhomogeneous nanoscale beams, *Mech. Adv. Mater. Struct.*, vol. 24, no. 11, pp. 924–936, 2017. DOI: [10.1080/15376494.2016.1196795](https://doi.org/10.1080/15376494.2016.1196795).
- [43] F. Ebrahimi, and M.R. Barati, Vibration analysis of parabolic shear-deformable piezoelectrically actuated nanoscale beams incorporating thermal effects, *Mech. Adv. Mater. Struct.*, vol. 25, no. 11, pp. 917–929, 2018. DOI: [10.1080/15376494.2017.1323141](https://doi.org/10.1080/15376494.2017.1323141).
- [44] M. Lori Dehsaraji, A. Loghman, and M. Arefi, Three-dimensional thermo-electro-mechanical buckling analysis of functionally graded piezoelectric micro/nano-shells based on modified couple stress theory considering thickness stretching effect, *Mech. Adv. Mater. Struct.*, vol. 28, no. 19, pp. 2030–2045, 2021. DOI: [10.1080/15376494.2020.1716419](https://doi.org/10.1080/15376494.2020.1716419).
- [45] P. Wang, P. Yuan, S. Sahmani, and B. Safaei, Size-dependent nonlinear harmonically soft excited oscillations of nonlocal strain gradient FGM composite truncated conical microshells with magnetostrictive facesheets, *Mech. Based Des. Struct. Mach.*, vol. 51, no. 1, pp. 1–27, 2023. DOI: [10.1080/15397734.2021.1903495](https://doi.org/10.1080/15397734.2021.1903495).
- [46] M.F. Ahari, and M. Ghadiri, Resonator vibration of a magneto-electro-elastic nano-plate integrated with FGM layer subjected to the nano mass-Spring-damper system and a moving load, *Waves Random Complex Medium*, pp. 1–39, 2022. DOI: [10.1080/17455030.2022.2053233](https://doi.org/10.1080/17455030.2022.2053233).
- [47] L. Guo, X. Xin, D. Shahsavari, and B. Karami, Dynamic response of porous E-FGM thick microplate resting on elastic foundation subjected to moving load with acceleration, *Thin-Walled Struct.*, vol. 173, pp. 108981, 2022. DOI: [10.1016/j.tws.2022.108981](https://doi.org/10.1016/j.tws.2022.108981).
- [48] M.W.T. Mak, and J.M. Lees, Carbon reduction and strength enhancement in functionally graded reinforced concrete beams, *Eng. Struct.*, vol. 277, pp. 115358, 2023. DOI: [10.1016/j.eng-struct.2022.115358](https://doi.org/10.1016/j.eng-struct.2022.115358).
- [49] H. Lazreg, B. Fabrice, M. Royal, A. Ali, and G.M. Hassan, Bending and buckling of porous multidirectional functionality graded sandwich plate, *Struct. Eng. Mech.*, vol. 85, pp. 233–246, 2023. DOI: [10.12989/SEM.2023.85.2.233](https://doi.org/10.12989/SEM.2023.85.2.233).
- [50] R. Elloumi, S. El-Borgi, M.A. Guler, and I. Kallel-Kamoun, The contact problem of a rigid stamp with friction on a functionally graded magneto-electro-elastic half-plane, *Acta Mech.*, vol. 227, no. 4, pp. 1123–1156, 2016. DOI: [10.1007/s00707-015-1504-2](https://doi.org/10.1007/s00707-015-1504-2).
- [51] V. Mahesh, and S.A. Ponnusami, Nonlinear damped transient response of sandwich auxetic plates with porous magneto-electro-elastic facesheets, *Eur. Phys. J. Plus*, vol. 137, no. 5, pp. 563, 2022. DOI: [10.1140/epjp/s13360-022-02756-x](https://doi.org/10.1140/epjp/s13360-022-02756-x).
- [52] H. Gao, X. Huang, X. Ma, X. Li, L. Guo, and H. Yang, An ultra-wideband coding polarizer for beam control and RCS reduction, *Front. Phys.*, vol. 18, no. 4, pp. 42301, 2023. DOI: [10.1007/s11467-022-1252-4](https://doi.org/10.1007/s11467-022-1252-4).
- [53] M.C. Kiran, and S. Kattimani, Assessment of vibrational frequencies and static characteristics of multilayered skew magneto-electro-elastic plates: a finite element study, *Iran J. Sci. Technol. Trans. Mech. Eng.*, vol. 44, no. 1, pp. 61–82, 2020. DOI: [10.1007/s40997-018-0250-1](https://doi.org/10.1007/s40997-018-0250-1).
- [54] S.Q. Zhang, Y.F. Zhao, X. Wang, M. Chen, and R. Schmidt, Static and dynamic analysis of functionally graded magneto-electro-elastic plates and shells, *Compos. Struct.*, vol. 281, pp. 114950, 2022. DOI: [10.1016/j.compstruct.2021.114950](https://doi.org/10.1016/j.compstruct.2021.114950).
- [55] I. Esen, and R. Özmen, Thermal vibration and buckling of magneto-electro-elastic functionally graded porous nanoplates using nonlocal strain gradient elasticity, *Compos. Struct.*, vol. 296, pp. 115878, 2022. DOI: [10.1016/j.compstruct.2022.115878](https://doi.org/10.1016/j.compstruct.2022.115878).
- [56] X. Yu, X. Fan, and X. Bi, Size-dependent frequency analysis of the magneto-electro-elastic rotary microdisk by incorporating modified couple stress and higher-order shear deformation theories, *Mech. Based Des. Struct. Mach.*, vol. 51, no. 4, pp. 1822–1841, 2023. DOI: [10.1080/15397734.2021.1878904](https://doi.org/10.1080/15397734.2021.1878904).
- [57] D.T.D. Nguyen, F. Javidan, M. Attar, S. Natarajan, Z. Yang, E.H. Ooi, C. Song, and E.T. Ooi, Fracture analysis of cracked magneto-electro-elastic functionally graded materials using scaled boundary finite element method, *Theor. Appl. Fract. Mech.*, vol. 118, pp. 103228, 2022. DOI: [10.1016/j.tafmec.2021.103228](https://doi.org/10.1016/j.tafmec.2021.103228).
- [58] Z. Li, Q. Wang, B. Qin, R. Zhong, and H. Yu, Vibration and acoustic radiation of magneto-electro-thermo-elastic functionally graded porous plates in the multi-physics fields, *Int. J. Mech. Sci.*, vol. 185, pp. 105850, 2020. DOI: [10.1016/j.ijmecsci.2020.105850](https://doi.org/10.1016/j.ijmecsci.2020.105850).
- [59] A. Sharma, Effect of porosity on active vibration control of smart structure using porous functionally graded piezoelectric material, *Compos. Struct.*, vol. 280, pp. 114815, 2022. DOI: [10.1016/j.compstruct.2021.114815](https://doi.org/10.1016/j.compstruct.2021.114815).
- [60] Y. Gogotsi, *Nanomaterials Handbook. Advanced Materials and Technologies Series*, 2nd edition. CRC Press, Boca Raton, 2017. DOI: [10.1201/9781315371795](https://doi.org/10.1201/9781315371795).
- [61] K. Gao, Q. Huang, S. Kitipornchai, and J. Yang, Nonlinear dynamic buckling of functionally graded porous beams, *Mech. Adv. Mater. Struct.*, vol. 28, no. 4, pp. 418–429, 2021. DOI: [10.1080/15376494.2019.1567888](https://doi.org/10.1080/15376494.2019.1567888).
- [62] N. Wattanasakulpong, and V. Ungbhakorn, Linear and nonlinear vibration analysis of elastically restrained ends FGM beams with porosities, *Aerosp. Sci. Technol.*, vol. 32, no. 1, pp. 111–120, 2014. DOI: [10.1016/j.ast.2013.12.002](https://doi.org/10.1016/j.ast.2013.12.002).
- [63] F. Ebrahimi, F. Ghasemi, and E. Salari, Investigating thermal effects on vibration behavior of temperature-dependent compositionally graded Euler beams with porosities, *Meccanica*, vol. 51, no. 1, pp. 223–249, 2016. DOI: [10.1007/s11012-015-0208-y](https://doi.org/10.1007/s11012-015-0208-y).
- [64] K. Li, D. Wu, X. Chen, J. Cheng, Z. Liu, W. Gao, and M. Liu, Isogeometric Analysis of functionally graded porous plates reinforced by graphene platelets, *Compos. Struct.*, vol. 204, pp. 114–130, 2018. DOI: [10.1016/j.compstruct.2018.07.059](https://doi.org/10.1016/j.compstruct.2018.07.059).
- [65] Y.S. Touloukian, *Thermophysical Properties of High Temperature Solid Materials*. Macmillan, New York, 1967.
- [66] Y.S. Touloukian, *Thermophysical Properties of High Temperature Solid Materials*. Volume 4. Oxides and Their Solutions and Mixtures. Part 1, vol. 1. Macmillan, New York, 1966.
- [67] Y. Kiani, and M.R. Eslami, An exact solution for thermal buckling of annular FGM plates on an elastic medium, *Compos. Part B Eng.*, vol. 45, no. 1, pp. 101–110, 2013. DOI: [10.1016/j.compositesb.2012.09.034](https://doi.org/10.1016/j.compositesb.2012.09.034).

- [68] D.G. Zhang, Thermal post-buckling and nonlinear vibration analysis of FGM beams based on physical neutral surface and high order shear deformation theory, *Meccanica*, vol. 49, no. 2, pp. 283–293, 2014. DOI: [10.1007/s11012-013-9793-9](https://doi.org/10.1007/s11012-013-9793-9).
- [69] A.C. Eringen, Theories of nonlocal plasticity, *Int. J. Eng. Sci.*, vol. 21, no. 7, pp. 741–751, 1983. DOI: [10.1016/0020-7225\(83\)90058-7](https://doi.org/10.1016/0020-7225(83)90058-7).
- [70] C.W. Lim, G. Zhang, and J.N. Reddy, A higher-order nonlocal elasticity and strain gradient theory and its applications in wave propagation, *J. Mech. Phys. Solids.*, vol. 78, pp. 298–313, 2015. DOI: [10.1016/j.jmps.2015.02.001](https://doi.org/10.1016/j.jmps.2015.02.001).
- [71] L. Li, X. Li, and Y. Hu, Free vibration analysis of nonlocal strain gradient beams made of functionally graded material, *Int. J. Eng. Sci.*, vol. 102, pp. 77–92, 2016. DOI: [10.1016/j.ijengsci.2016.02.010](https://doi.org/10.1016/j.ijengsci.2016.02.010).
- [72] A. Farajpour, and A. Rastgoo, Influence of carbon nanotubes on the buckling of microtubule bundles in viscoelastic cytoplasm using nonlocal strain gradient theory, *Results Phys.*, vol. 7, pp. 1367–1375, 2017. DOI: [10.1016/j.rinp.2017.03.038](https://doi.org/10.1016/j.rinp.2017.03.038).
- [73] A.C. Eringen, On differential equations of nonlocal elasticity and solutions of screw dislocation and surface waves, *J. Appl. Phys.*, vol. 54, no. 9, pp. 4703–4710, 1983. DOI: [10.1063/1.332803](https://doi.org/10.1063/1.332803).
- [74] K.K. Żur, M. Arefi, J. Kim, and J.N. Reddy, Free vibration and buckling analyses of magneto-electro-elastic FGM nanoplates based on nonlocal modified higher-order sinusoidal shear deformation theory, *Compos. Part B Eng.*, vol. 182, pp. 107601, 2020. DOI: [10.1016/j.compositesb.2019.107601](https://doi.org/10.1016/j.compositesb.2019.107601).
- [75] J.N. Reddy, C.M. Wang, and S. Kitipornchai, Axisymmetric bending of functionally graded circular and annular plates, *Eur. J. Mech. A/Solids*, vol. 18, no. 2, pp. 185–199, 1999. DOI: [10.1016/S0997-7538\(99\)80011-4](https://doi.org/10.1016/S0997-7538(99)80011-4).
- [76] E. Pan, and P.R. Heyliger, Free vibrations of simply supported and multilayered magneto-electro-elastic plates, *J. Sound Vib.*, vol. 252, no. 3, pp. 429–442, 2002. DOI: [10.1006/jsvi.2001.3693](https://doi.org/10.1006/jsvi.2001.3693).
- [77] M. Arefi, and A.M. Zenkour, A simplified shear and normal deformations nonlocal theory for bending of functionally graded piezomagnetic sandwich nanobeams in magneto-thermo-electric environment, *J. Sandwich Struct. Mater.*, vol. 18, no. 5, pp. 624–651, 2016. DOI: [10.1177/1099636216652581](https://doi.org/10.1177/1099636216652581).
- [78] M. Arefi, and A.M. Zenkour, Free vibration analysis of a three-layered microbeam based on strain gradient theory and three-unknown shear and normal deformation theory, *Steel Compos. Struct.*, vol. 26, pp. 421–437, 2018. DOI: [10.12989/scs.2018.26.4.421](https://doi.org/10.12989/scs.2018.26.4.421).
- [79] J.N. Reddy, Energy principles and variational methods. In: *Theory and Analysis of Elastic Plates and Shells*, CRC Press, Boca Raton, 2020. DOI: [10.1201/9780849384165-6](https://doi.org/10.1201/9780849384165-6).
- [80] G.T. Monaco, N. Fantuzzi, F. Fabbrocino, and R. Luciano, Critical temperatures for vibrations and buckling of magneto-electro-elastic nonlocal strain gradient plates, *Nanomaterials*, vol. 11, pp. 1–18, 2021. DOI: [10.3390/nano11010087](https://doi.org/10.3390/nano11010087).
- [81] F. Ramirez, P.R. Heyliger, and E. Pan, Discrete layer solution to free vibrations of functionally graded magneto-electro-elastic plates, *Mech. Adv. Mater. Struct.*, vol. 13, no. 3, pp. 249–266, 2006. DOI: [10.1080/15376490600582750](https://doi.org/10.1080/15376490600582750).
- [82] R. Aghababaei, and J.N. Reddy, Nonlocal third-order shear deformation plate theory with application to bending and vibration of plates, *J. Sound Vib.*, vol. 326, no. 1–2, pp. 277–289, 2009. DOI: [10.1016/j.jsv.2009.04.044](https://doi.org/10.1016/j.jsv.2009.04.044).
- [83] J.N. Reddy, and C.D. Chin, Thermomechanical analysis of functionally graded cylinders and plates, *J. Thermal Stress.*, vol. 21, no. 6, pp. 593–626, 1998. DOI: [10.1080/01495739808956165](https://doi.org/10.1080/01495739808956165).

Appendix:

$$\begin{aligned}
 A_{ij}^{(n)} &= \int_{-h/2-h_s}^{-h/2} C_{ij}^s \{1, z, z^2\} dz + \int_{-h/2}^{h/2} C_{ij}^c \{1, z, z^2\} dz + \int_{h/2}^{h/2+h_s} C_{ij}^s \{1, z, z^2\} dz \quad n = 0, 1, 2 \\
 \bar{A}_{ij}^{(\bar{n})} &= \int_{-h/2-h_s}^{-h/2} C_{ij}^s f(z) \{1, z, f(z)\} dz + \int_{-h/2}^{h/2} C_{ij}^c f(z) \{1, z, f(z)\} dz \\
 &\quad + \int_{h/2}^{h/2+h_s} C_{ij}^s f(z) \{1, z, f(z)\} dz, \quad \bar{n} = 0, 1, f \\
 \tilde{A}_{ij}^{(\tilde{n})} &= \int_{-h/2-h_s}^{-h/2} C_{ij}^s g'(z) \{1, z, g'(z), f(z)\} dz + \int_{-h/2}^{h/2} C_{ij}^c g'(z) \{1, z, g'(z), f(z)\} dz + \int_{h/2}^{h/2+h_s} C_{ij}^s g'(z) \{1, z, g'(z), f(z)\} dz, \quad \tilde{n} = 0, 1, g', f \\
 \tilde{A}_{ij}^{(\tilde{n})} &= \int_{-h/2-h_s}^{-h/2} C_{ij}^s g^2(z) dz + \int_{-h/2}^{h/2} C_{ij}^c g^2(z) dz + \int_{h/2}^{h/2+h_s} C_{ij}^s g^2(z) dz
 \end{aligned} \tag{A1}$$

$$\begin{aligned}
 B_{eij}^{(k)} &= - \left[\int_{-h/2-h_s}^{-h/2} e_{ij} \left(\frac{2\varphi_0}{h_s} \right) \left\{ z, f(z), g'(z), \left(\frac{h_s}{2\varphi_0} \right) \cos \left(\frac{\pi z_2}{h_s} \right) \right\} dz + \int_{-h/2}^{h/2} e_{ij} \left(\frac{2\varphi_0}{h} \right) \left\{ z, f(z), g'(z), \left(\frac{h_s}{2\varphi_0} \right) \cos \left(\frac{\pi z}{h_s} \right) \right\} dz \right. \\
 &\quad \left. + \int_{h/2}^{h/2+h_s} e_{ij} \left(\frac{2\varphi_0}{h_s} \right) \left\{ z, f(z), g'(z), \left(\frac{h_s}{2\varphi_0} \right) \cos \left(\frac{\pi z_2}{h_s} \right) \right\} dz \right], \quad k = 1, f, g', g \\
 \bar{B}_{eij}^{(k)} &= - \left[\int_{-h/2-h_s}^{-h/2} e_{ij} \left[\frac{\pi}{h_s} \sin \left(\frac{\pi z_1}{h_s} \right) \right] \{1, z, f(z), g'(z)\} dz + \int_{-h/2}^{h/2} e_{ij} \left[\frac{\pi}{h} \sin \left(\frac{\pi z}{h} \right) \right] \{1, z, f(z), g'(z)\} dz \right. \\
 &\quad \left. + \int_{h/2}^{h/2+h_s} e_{ij} \left[\frac{\pi}{h_s} \sin \left(\frac{\pi z_2}{h_s} \right) \right] \{1, z, f(z), g'(z)\} dz \right], \quad k = 0, 1, f, g' \\
 B_{qij}^{(k)} &= - \left[\int_{-h/2-h_s}^{-h/2} q_{ij} \left(\frac{2\varphi_0}{h_s} \right) \left\{ z, f(z), g'(z), \left(\frac{h_f}{2\varphi_0} \right) \cos \left(\frac{\pi z_1}{h_s} \right) \right\} dz + \int_{-h/2}^{h/2} q_{ij} \left(\frac{2\varphi_0}{h} \right) \left\{ z, f(z), g'(z), \left(\frac{h}{2\varphi_0} \right) \cos \left(\frac{\pi z}{h} \right) \right\} dz \right. \\
 &\quad \left. + \int_{h/2}^{h/2+h_s} q_{ij} \left(\frac{2\varphi_0}{h_s} \right) \left\{ z, f(z), g'(z), \left(\frac{h_f}{2\varphi_0} \right) \cos \left(\frac{\pi z_2}{h_s} \right) \right\} dz \right], \quad k = 1, f, g', g \\
 \bar{B}_{qij}^{(k)} &= - \left[\int_{-h/2-h_s}^{-h/2} q_{ij} \left[\frac{\pi}{h_s} \sin \left(\frac{\pi z_1}{h_s} \right) \right] \{1, z, f(z), g'(z)\} dz + \int_{-h/2}^{h/2} q_{ij} \left[\frac{\pi}{h} \sin \left(\frac{\pi z}{h} \right) \right] \{1, z, f(z), g'(z)\} dz \right. \\
 &\quad \left. + \int_{h/2}^{h/2+h_s} q_{ij} \left[\frac{\pi}{h_s} \sin \left(\frac{\pi z_2}{h_s} \right) \right] \{1, z, f(z), g'(z)\} dz \right], \quad k = 0, 1, f, g'
 \end{aligned} \tag{A2}$$

$$\begin{aligned}
 P_{\varepsilon_{ij}}^{(n)} &= - \left[\int_{-h/2-h_s}^{-h/2} \varepsilon_{ij} \left\{ \left(\frac{2\varphi_0}{h_s} \right) \left[\frac{\pi}{h_s} \sin \left(\frac{\pi z_1}{h_s} \right) \right], \left[\frac{\pi}{h_s} \sin \left(\frac{\pi z_1}{h_s} \right) \right]^2, \left[\cos \left(\frac{\pi z_1}{h_s} \right) \right]^2 \right\} dz + \int_{-h/2}^{h/2} \varepsilon_{ij} \left\{ \left(\frac{2\varphi_0}{h} \right) \left[\frac{\pi}{h} \sin \left(\frac{\pi z}{h} \right) \right], \left[\frac{\pi}{h} \sin \left(\frac{\pi z}{h} \right) \right]^2, \left[\cos \left(\frac{\pi z}{h} \right) \right]^2 \right\} dz \right. \\
 &\quad \left. + \int_{h/2}^{h/2+h_s} \varepsilon_{ij} \left\{ \left(\frac{2\varphi_0}{h_s} \right) \left[\frac{\pi}{h_s} \sin \left(\frac{\pi z_2}{h_s} \right) \right], \left[\frac{\pi}{h_s} \sin \left(\frac{\pi z_2}{h_s} \right) \right]^2, \left[\cos \left(\frac{\pi z_2}{h_s} \right) \right]^2 \right\} dz \right], \quad n = 1, s2, c2 \\
 P_{g_{ij}}^{(n)} &= - \left[\int_{-h/2-h_s}^{-h/2} g_{ij} \left\{ \left(\frac{2\varphi_0}{h_s} \right) \left[\frac{\pi}{h_s} \sin \left(\frac{\pi z_1}{h_s} \right) \right], \left[\frac{\pi}{h_s} \sin \left(\frac{\pi z_1}{h_s} \right) \right]^2, \left[\cos \left(\frac{\pi z_1}{h_s} \right) \right]^2 \right\} dz + \int_{-h/2}^{h/2} g_{ij} \left\{ \left(\frac{2\varphi_0}{h} \right) \left[\frac{\pi}{h} \sin \left(\frac{\pi z}{h} \right) \right], \left[\frac{\pi}{h} \sin \left(\frac{\pi z}{h} \right) \right]^2, \left[\cos \left(\frac{\pi z}{h} \right) \right]^2 \right\} dz \right. \\
 &\quad \left. + \int_{h/2}^{h/2+h_s} g_{ij} \left\{ \left(\frac{2\varphi_0}{h_s} \right) \left[\frac{\pi}{h_s} \sin \left(\frac{\pi z_2}{h_s} \right) \right], \left[\frac{\pi}{h_s} \sin \left(\frac{\pi z_2}{h_s} \right) \right]^2, \left[\cos \left(\frac{\pi z_2}{h_s} \right) \right]^2 \right\} dz \right], \quad n = 1, s2, c2 \\
 P_{\mu_{ij}}^{(n)} &= - \left[\int_{-h/2-h_s}^{-h/2} \mu_{ij} \left\{ \left(\frac{2\varphi_0}{h_s} \right) \left[\frac{\pi}{h_s} \sin \left(\frac{\pi z_1}{h_s} \right) \right], \left[\frac{\pi}{h_s} \sin \left(\frac{\pi z_1}{h_s} \right) \right]^2, \left[\cos \left(\frac{\pi z_1}{h_s} \right) \right]^2 \right\} dz + \int_{-h/2}^{h/2} \mu_{ij} \left\{ \left(\frac{2\varphi_0}{h} \right) \left[\frac{\pi}{h} \sin \left(\frac{\pi z}{h} \right) \right], \left[\frac{\pi}{h} \sin \left(\frac{\pi z}{h} \right) \right]^2, \left[\cos \left(\frac{\pi z}{h} \right) \right]^2 \right\} dz \right. \\
 &\quad \left. + \int_{h/2}^{h/2+h_s} \mu_{ij} \left\{ \left(\frac{2\varphi_0}{h_s} \right) \left[\frac{\pi}{h_s} \sin \left(\frac{\pi z_2}{h_s} \right) \right], \left[\frac{\pi}{h_s} \sin \left(\frac{\pi z_2}{h_s} \right) \right]^2, \left[\cos \left(\frac{\pi z_2}{h_s} \right) \right]^2 \right\} dz \right], \quad n = 1, s2, c2
 \end{aligned}$$

(A3)

$$\begin{aligned}
 K_{11} &= -c_2 \left(\alpha^2 A_{11}^{(0)} + \beta^2 A_{66}^{(0)} \right) \\
 K_{12} &= -c_2 \alpha \beta \left(A_{12}^{(0)} + A_{66}^{(0)} \right) \\
 K_{13} &= c_2 \left(\alpha^3 A_{11}^{(1)} + \alpha \beta^2 \left(A_{12}^{(1)} + 2A_{66}^{(1)} \right) \right) \\
 K_{14} &= c_2 \left(\alpha^3 \bar{A}_{11}^{(0)} + \alpha \beta^2 \left(\bar{A}_{12}^{(0)} + 2\bar{A}_{66}^{(0)} \right) \right) \\
 K_{15} &= c_2 \alpha \tilde{A}_{13}^{(0)} \\
 K_{16} &= c_2 \alpha \bar{B}_{e31}^{(0)} \\
 K_{17} &= c_2 \alpha \bar{B}_{q31}^{(0)} \\
 K_{22} &= -c_2 \left(\beta^2 A_{22}^{(0)} + \alpha^2 A_{66}^{(0)} \right) \\
 K_{23} &= -c_2 \left(\beta^3 A_{22}^{(1)} + \beta \alpha^2 \left(A_{12}^{(1)} + 2A_{66}^{(1)} \right) \right) \\
 K_{24} &= c_2 \left(\beta^3 \bar{A}_{22}^{(0)} + \beta \alpha^2 \left(\bar{A}_{12}^{(0)} + 2\bar{A}_{66}^{(0)} \right) \right) \\
 K_{25} &= c_2 \beta \tilde{A}_{23}^{(0)} \\
 K_{26} &= c_2 \beta \bar{B}_{e32}^{(0)} \\
 K_{27} &= c_2 \beta \bar{B}_{q32}^{(0)} \\
 K_{33} &= \alpha^2 \left[1 + \mathcal{B}(\alpha^2 + \beta^2) \right] (N_0 + p_{e31} + p_{q31}) + \beta^2 \left[1 + \mathcal{B}(\alpha^2 + \beta^2) \right] (\gamma N_0 + p_{e32} + p_{q32}) - c_2 \left(\alpha^4 A_{11}^{(2)} - \beta^4 A_{22}^{(2)} - 2\alpha^2 \beta^2 \left(A_{12}^{(2)} + 2A_{66}^{(2)} \right) \right) \\
 K_{34} &= -c_2 \left(\alpha^4 \bar{A}_{11}^{(1)} + \beta^4 \bar{A}_{22}^{(1)} + 2\alpha^2 \beta^2 \left(\bar{A}_{12}^{(1)} + 2\bar{A}_{66}^{(1)} \right) \right) \\
 K_{35} &= -c_2 \left(\alpha^2 \tilde{A}_{13}^{(1)} + \beta^2 A_{23}^{(1)} \right) \\
 K_{36} &= -c_2 \left(\alpha^2 \bar{B}_{e31}^{(1)} + \beta^2 \bar{B}_{e32}^{(1)} \right) \\
 K_{37} &= -c_2 \left(\alpha^2 \bar{B}_{q31}^{(1)} + \beta^2 \bar{B}_{q32}^{(1)} \right) \\
 K_{44} &= -c_2 \left(\alpha^2 \hat{A}_{55}^{(0)} + \beta^2 \hat{A}_{44}^{(0)} + \alpha^4 \bar{A}_{11}^{(f)} + \beta^4 \bar{A}_{22}^{(f)} + 2\alpha^2 \beta^2 \left(\bar{A}_{12}^{(f)} + 2\bar{A}_{66}^{(f)} \right) \right) \\
 K_{45} &= -c_2 \left(\alpha^2 \left(\tilde{A}_{13}^{(f)} + \hat{A}_{55}^{(0)} \right) + \beta^2 \left(\tilde{A}_{23}^{(f)} + \hat{A}_{44}^{(0)} \right) \right) \\
 K_{46} &= c_2 \left(\alpha^2 \left(B_{e15}^{(g)} - \bar{B}_{e31}^{(f)} \right) + \beta^2 \left(B_{e24}^{(g)} - \bar{B}_{e32}^{(f)} \right) \right) \\
 K_{47} &= c_2 \left(\alpha^2 \left(B_{q15}^{(g)} - \bar{B}_{q31}^{(f)} \right) + \beta^2 \left(B_{q24}^{(g)} - \bar{B}_{q32}^{(f)} \right) \right)
 \end{aligned}$$

$$\begin{aligned}
K_{55} &= -c_2 \left(\hat{A}_{33}^{(g)} + \alpha^2 \hat{A}_{55}^{(0)} + \beta^2 \hat{A}_{44}^{(0)} \right) \\
K_{56} &= c_2 \left(\alpha^2 B_{e15}^{(g)} + \beta^2 B_{e24}^{(g)} - \bar{B}_{e33}^{(g)} \right) \\
K_{57} &= c_2 \left(\alpha^2 B_{q15}^{(g)} + \beta^2 B_{q24}^{(g)} - \bar{B}_{q33}^{(g)} \right) \\
K_{66} &= c_2 \left(\alpha^2 p_{e11}^{(c2)} + \beta^2 p_{e22}^{(c2)} + p_{e33}^{(s2)} \right) \\
K_{66} &= c_2 \left(\alpha^2 p_{g11}^{(c2)} + \beta^2 p_{g22}^{(c2)} + p_{g33}^{(s2)} \right) \\
K_{77} &= c_2 \left(\alpha^2 p_{\mu11}^{(c2)} + \beta^2 p_{\mu22}^{(c2)} + p_{\mu33}^{(s2)} \right) \\
c_2 &= (1 + I_m(\alpha^2 + \beta^2))
\end{aligned} \tag{A4}$$

$$\begin{aligned}
M_{11} &= -[1 + \mathcal{B}(\alpha^2 + \beta^2)] m_0 \\
M_{13} &= \alpha [1 + \mathcal{B}(\alpha^2 + \beta^2)] m_1 \\
M_{14} &= \alpha [1 + \mathcal{B}(\alpha^2 + \beta^2)] m_3 \\
M_{12} &= M_{15} = M_{16} = M_{17} = 0 \\
M_{22} &= -[1 + \mathcal{B}(\alpha^2 + \beta^2)] m_0 \\
M_{23} &= \beta [1 + \mathcal{B}(\alpha^2 + \beta^2)] m_1 \\
M_{24} &= \beta [1 + \mathcal{B}(\alpha^2 + \beta^2)] m_3 \\
M_{25} &= M_{26} = M_{27} = 0 \\
M_{33} &= -[1 + \mathcal{B}(\alpha^2 + \beta^2)] m_0 - (\alpha^2 + \beta^2) [1 + \mathcal{B}(\alpha^2 + \beta^2)] m_2 \\
M_{34} &= -[1 + \mathcal{B}(\alpha^2 + \beta^2)] m_0 - (\alpha^2 + \beta^2) [1 + \mathcal{B}(\alpha^2 + \beta^2)] m_4 \\
M_{35} &= -[1 + \mathcal{B}(\alpha^2 + \beta^2)] m_6 \\
M_{36} &= M_{37} = 0 \\
M_{44} &= -[1 + \mathcal{B}(\alpha^2 + \beta^2)] m_0 - (\alpha^2 + \beta^2) [1 + \mathcal{B}(\alpha^2 + \beta^2)] m_5 \\
M_{45} &= -[1 + \mathcal{B}(\alpha^2 + \beta^2)] m_6 \\
M_{46} &= M_{47} = 0 \\
M_{55} &= -[1 + \mathcal{B}(\alpha^2 + \beta^2)] m_7 \\
M_{56} &= M_{57} = M_{66} = M_{67} = M_{77} = 0
\end{aligned} \tag{A5}$$